COUPLING OF A MULTIBODY SIMULATION TOOL FOR THE ANALYSIS OF ROTARY SYSTEMS WITH A PANEL BASED FLOW SOLVER AND A NAVIER-STOKES FLOW SOLVER

A THESIS SUBMITTED TO
THE GRADUATE SCHOOL OF NATURAL AND APPLIED SCIENCES
OF
MIDDLE EAST TECHNICAL UNIVERSITY

BY

SEMİH SOĞANCI

IN PARTIAL FULLFILLMENT OF THE REQUIREMENTS
FOR
MASTER OF ENGINEERING
IN
AEROSPACE ENGINEERING

JUNE 2018

Approval of the thesis:

COUPLING OF A MULTIBODY SIMULATION TOOL FOR THE ANALYSIS OF ROTARY SYSTEMS WITH A PANEL BASED FLOW SOLVER AND A NAVIER-STOKES FLOW SOLVER

submitted by **SEMİH SOĞANCI** in partial fulfillment of the requirements for the degree of **Master of Science in Aerospace Engineering Department, Middle East Technical University** by,

Prof. Dr. Halil Kalıpçılar
Dean, Graduate School of **Natural and Applied Sciences** __________________

Prof. Dr. Ozan Tekinalp
Head of Department, **Aerospace Engineering** __________________

Prof. Dr. Altan Kayran
Supervisor, **Aerospace Engineering Dept., METU** __________________

Prof. Dr. İsmail Hakkı Tuncer
Co-Supervisor, **Aerospace Engineering Dept., METU** __________________

Examining Committee Members:

Assoc. Prof. Dr. Dilek Funda Kurtuluş
Aerospace Engineering Dept., METU __________________

Prof. Dr. Altan Kayran
Aerospace Engineering Dept., METU __________________

Assoc. Prof. Dr. Demirkan Çöker
Aerospace Engineering Dept., METU __________________

Asst. Prof. Dr. Mustafa Perçin
Aerospace Engineering Dept., METU __________________

Asst. Prof. Dr. Durmuş Sinan Körpe
Aeronautical Engineering Dept., UTAA __________________

Date: 28.06.2018

I hereby declare that all information in this document has been obtained and presented in accordance with academic rules and ethical conduct. I also declare that, as required by these rules and conduct, I have fully cited and referenced all material and results that are not original to this work.

Name, Last name: Semih Soğancı

Signature:

ABSTRACT

COUPLING OF A MULTIBODY SIMULATION TOOL FOR THE ANALYSIS OF ROTARY SYSTEMS WITH A PANEL BASED FLOW SOLVER AND A NAVIER-STOKES FLOW SOLVER

Soğancı, Semih
M.Sc., Department of Aerospace Engineering
Supervisor: Prof. Dr. Altan Kayran
Co-Supervisor: Prof. Dr. İsmail Hakkı Tuncer

June 2018, 173 pages

In rotorcraft design, aeroelastic effects on the main rotor blades play a critical role in the accurate estimation of the external loading acting on the structure. The external loading is mainly due to the aerodynamic loads and the inertial loads on the main rotor blades. High aspect ratio blades largely deform in flapping direction on top of rigid body flapping, and due to the rigid and elastic flapping motion, the airloads acting on the blades change continuously. Hence, the rotor blade loads analysis should be interdisciplinary relying on the nonlinear structural dynamics, the aerodynamics and the control. A flexible multibody dynamics solver, DYMORE, is used as a comprehensive analysis tool for rotor simulations. Aerodynamic loads are internally calculated from two dimensional aerodynamic tables which give the aerodynamic coefficients based on the angle of attack and the Mach number. In the aerodynamic shape optimization of blade profiles, at each iteration in the shape optimization, sections are perturbed and for the perturbed sections aerodynamic loads can not be calculated using the look-up tables since these tables are for a certain airfoil shape.

Therefore, there is a need for an aerodynamic solver to provide the solution for the perturbed sections.

In this study, the internal aerodynamic module of DYMORE is replaced first with a panel based flow solver, XFOIL, and then a Reynolds Averaged Navier-Stokes (RANS) solver, SU2. At each section, the aerodynamic load coefficients obtained from XFOIL and SU2 are used instead of interpolated table coefficients. XFOIL and SU2 source codes are embedded into DYMORE and compiled together using the C-FORTRAN interoperability functions and the external data structures with assigned pointers. The simulations are carried out for an isolated rotor in hover. UH-60 main rotor architecture is modeled and NACA 0012 profile is used for blade sections. Validation studies are carried out at Mach numbers of 0.4 and 0.7 for the angle of attack range of 0 to 15 degrees. The lift and drag coefficients obtained from XFOIL and SU2 are in good agreement with the table values. Hub airloads and blade angles obtained from the coupled analyses are also in close correlation with the internal aerodynamic results.

Keywords: Computational Fluid Dynamics (CFD) - Computational Structural Dynamics (CSD) Coupling, Comprehensive Rotorcraft Simulation, Flexible Multibody Dynamics, Panel Method, Reynolds Averaged Navier-Stokes

ÖZ

DÖNEN SİSTEMLERİN ÇOKLU KÜTLELİ BENZETİM ARACININ PANEL TABANLI AKIŞ ÇÖZÜCÜSÜ VE NAVIER-STOKES AKIŞ ÇÖZÜCÜSÜ İLE ETKİLEŞİMLİ ANALİZİ

Soğancı, Semih
Yüksek Lisans, Havacılık ve Uzay Mühendisliği Bölümü
Tez Yöneticisi: Prof. Dr. Altan Kayran
Ortak Tez Yöneticisi: Prof. Dr. İsmail Hakkı Tuncer

Haziran 2018, 173 sayfa

Helikopter ana rotor palleri üzerindeki aeroelastik etkiler, yapıya etkiyen dış yüklerin yüksek doğrulukta bulunabilmesi için helikopter tasarımı açısından kritiktir. Dış yükler ana rotorda, temel olarak aerodinamik yüklerden ve atalet yüklerinden oluşur. Yüksek kiriş-veter oranlı paller çırpınma ile rijit çırpınma hareketinin üzerinde yüksek deformasyonlara uğrar ve rijit ve elastik çırpınma hareketlerinden dolayı pallere etkiyen aerodinamik ve atalet yükleri değişir. Bu nedenle, rotor pali yük analizleri doğrusal olmayan yapısal dinamik, aerodinamik ve kontrol ile ilintili disiplinler arası olmalıdır. Esnek çoklu cisim dinamiği çözücüsü, Dymore, kapsamlı analiz aracı olarak rotor benzetimlerinde kullanılır. Aerodinamik yükler dahili iki boyutlu aerodinamik katsayı tablolarından hesaplanır. Bu tablolar aerodinamik katsayıları Mach sayısına ve hücum açısına bağlı olarak verir. Pal kesitleri için yapılacak aerodinamik şekil optimizasyonunda, her iterasyonda kesit yüzeyleri değiştirilir ve tabloların sadece bir kesit profili için olması nedeniyle değiştirilmiş kesit yüzeyleri için aerodinamik yükler hesaplanamaz. Dolayısıyla, değiştirilmiş kesitlerde çözüm alabilmek için bir aerodinamik çözücü ihtiyacı vardır.

Bu çalışmada, DYMORE dahili aerodinamik modülü ilk olarak panel tabanlı akış çözücüsü, XFOIL, ve sonra Reynolds Ortalama Navier-Stokes çözücüsü, SU2 ile değiştirilmiştir. Her kesitte, XFOIL ve SU2 ile hesaplanan aerodinamik yük katsayıları ara değerlenen tablo verileri yerine kullanılmıştır. XFOIL ve SU2 kaynak kodları Dymore içine entegre edilmiştir ve C-FORTRAN birlikte çalışabilirlik fonksiyonları ve dış veri yapısı ile tanımlı işaretçiler kullanılarak derlenmiştir. Benzetimler askı koşulunda izole rotor için gerçekleştirilmiştir. UH-60 ana rotor mimarisi modellenmiştir ve NACA 0012 profili pal kesitleri için kullanılmıştır. Doğrulama çalışmaları, 0.4 ve 0.7 Mach sayılarında ve 0^o ile 15^o arasında hücum açıları için yapılmıştır. XFOIL ve SU2 ile hesaplanan kaldırma ve sürükleme katsayıları tablo verileri ile uyumludur. Ayrıca bütünleşik analizlerle bulunan merkezi rotor aerodinamik yükleri ve pal açıları dahili aerodinamik modülü sonuçları ile benzerdir.

Anahtar Kelimeler: Hesaplamalı Akışkanlar Dinamiği (HAD) - Hesaplamalı Yapısal Dinamik (HYD) Eşlenikli Çözümü, Kapsamlı Döner Kanat Hava Aracı Benzetimi, Esnek Çoklu Cisim Dinamiği, Panel Metod, Reynolds Ortalama Navier Stokes.

ACKNOWLEDGEMENTS

Firstly, I wish to express my deepest gratitude to my supervisors, Dr. Altan Kayran and Dr. İsmail Hakkı Tuncer for their guidance, advice, criticism, encouragements and insight throughout my research.

I would like to thank Dr. Dilek Funda Kurtuluş, Dr. Demirkan Çöker, Dr. Mustafa Perçin and Dr. Durmuş Sinan Körpe for their critics and suggestions in my thesis committee.

I am very grateful to Dr. Nilay Sezer Uzol and Dr. Serkan Özbay who gave the first insight and advice at the beginning of this study.

I specially would like to thank Bali İhsan Özturan for his support and suggestions.

I also wish to thank all my collegues and friends for their support.

I would like to acknowledge Turkish Aerospace Industries, Inc., (TAI) Helicopter Group where I have received the opportunity to study on rotor dynamics and aerodynamics.

Finally, I would like to dedicate this study to my mother and also my chemistry teacher, Sema Boyacı.

TABLE OF CONTENTS

CHAPTERS

LIST OF TABLES

TABLES

LIST OF FIGURES

FIGURES

LIST OF SYMBOLS

SYMBOLS

C_{l_α}	Lift curve slope
C_l	Sectional lift coefficient
C_d	Sectional drag coefficient
C_{d_0}	Zero lift drag coefficient
C_m	Sectional moment coefficient
C_{m_0}	Zero lift pitching moment coefficient
C_{p_0}	Incompressible pressure coefficient
C_p	Compressible pressure coefficient
β_c	Compressibility correction factor
Δn	First wall height
β	Flap angle
β_0	Coning angle
β_{1s}	Lateral cyclic flapping angle
β_{1c}	Longitudinal cyclic flapping angle
β_p	Precone angle
ξ	Lag angle
θ	Pitch angle
θ_0	Collective input
θ_{1s}	Longitudinal cyclic input
θ_{1c}	Lateral cyclic input
I_β	Second mass moment of inertia around flapping axis
k_β	Spring stiffness around flapping axis
$\dot{\beta}$	Flapping rate
$\ddot{\beta}$	Flapping acceleration
e	Hinge offset

S_{ξ}	First mass moment of inertia around lag axis
I_{ξ}	Second mass moment of inertia around lag axis
k_{ξ}	Spring stiffness around lag axis
$\dot{\xi}$	Lag rate
$\ddot{\xi}$	Lag acceleration
I_{f}	Total mass moment of inertia around feathering axis
I_0	Mass moment of inertia around sectional center of gravity
k_{θ}	Spring stiffness around feathering axis
$\theta_{control}$	Pitch angle prescribed by the controller
q_i	Generalized coordinates
$\vec{R}_i$	Vector between origin and cg of part i in multibody system
$\vec{r}_i$	Vector between origin and connection point between parts i and j
$\vec{d}_i$	Vector between cg of part i and connection point on part j
R_{x_i}	x component of vector $\vec{R}_i$
R_{y_i}	y component of vector $\vec{R}_i$
θ_i	Rotational degree of vector $\vec{R}_i$
A_i	Rotation matrix
$C(q,t)$	Constraint equation
M	Mass matrix
Q_e	External force at the joints
Q_c	Reaction force at the joints
λ	Lagrange multipliers
α	Angle of attack
φ	Inflow angle
M	Mach number
Re	Reynolds number
Re_{θ}	Momentum thickness Reynolds number
T	Thrust

ψ	Azimuth
r	Radial distance
R	Rotor radius
ρ	Air density
Ω	Rotor speed
A	Rotor disk area
C_T	Rotor thrust coefficient
λ	Inflow factor
v_i	Induced velocity
κ_x, κ_y	Harmonic inflow coefficients
χ	Wake angle
μ	Advance ratio
α_s	Rotor disk incidence
λ	Inflow factor
u_p	Axial component of relative flow velocity coming to blade section
u_t	Tangential component of relative flow velocity coming to blade section
u_r	Radial component of relative flow velocity coming to blade section
V_{rel}	Relative flow velocity coming to blade section
dL	Sectional lift force
dD	Sectional drag force
dT	Sectional thrust
dH	Sectional horizontal force
ds	Spanwise discrete section length
$\phi(x,y)$	Potential function
$\psi(x,y)$	Stream function
ψ_0	Stream function on airfoil surface
σ_i	Source strengths of panels
γ_i	Vortex strengths of panels

a_{ij}, b_{ij}	Influence coefficients
N	Panel number
δ	Boundary layer mass thickness
δ^*	Boundary layer displacement thickness
δ^{**}	Boundary layer density thickness
θ	Boundary layer momentum thickness
θ^*	Boundary layer kinetic energy thickness
H	Shape parameter
H^*	Kinetic energy shape parameter
H^{**}	Density flux shape parameter
H_k	Kinematic shape parameter
C_τ	Shear stress coefficient
$C_{\tau,EQ}$	Equilibrium shear stress coefficient
C_f	Skin friction coefficient
ρ_e	Boundary layer edge air density
u_e	Boundary layer edge flow velocity
M_e	Boundary layer edge Mach number
Φ	Integral quantity
e_t	Total energy
$V(t)$	Control volume
$S(t)$	Control surface
$\bar{\bar{T}}$	Stress tensor
p	Pressure
$\bar{\bar{I}}$	Identity tensor
$\bar{\bar{\tau}}$	Shear stress tensor
$\vec{f}_b$	Body force
μ	Dynamic viscosity
υ	Kinematic viscosity

μ_t	Turbulent eddy viscosity
$\breve{v}$	Kinematic eddy viscosity
R_{ij}	Reynolds Stress Tensor
$\overline{u}_J$	Mean velocity
u', v', w'	Fluctuation velocities
k	Turbulent kinetic energy
ω	Specific dissipation rate

ABBREVIATIONS

MBD	Multibody Dynamics
cg	Center of Gravity
FE	Finite Element
CFD	Computational Fluid Dynamics
CSD	Computational Structural Dynamics
BEM	Blade Element Momentum
RTT	Reynolds Transport Theorem
RSM	Reynolds Stress Model
TPP	Tip path plane
RANS	Reynolds Averaged Navier-Stokes
LES	Large Eddy Simulation
DNS	Direct Numerical Simulation
SA	Spalart Allmaras
SST	Shear Stress Transport

CHAPTER 1

INTRODUCTION

1.1. Overview

Rotorcraft design is highly multidisciplinary and complex so that it involves the steps of modeling and analyses, manufacturing, verification and certification. At the analysis and development stage, comprehensive simulations are required to obtain loads acting on the airframe components and on the rotary components to size the parts and the components for various operational flight conditions. On the main rotor, the forcing is mainly due to aerodynamic loads, centrifugal loads and inertial loads accompanied by Coriolis loads and rotational or linear spring and damper loads. The flow solution and the structural dynamic response are usually calculated via comprehensive analyses tools' time marching solutions. Calculated loads are then distributed to the components of the rotorcraft to size the parts through finite element analyses.

Due to the complexity of helicopter aerodynamics, in general for the blades, flow calculations have been performed by using the blade element theory. At the aerodynamic stations, the force and the moment coefficients are interpolated from the aerodynamic performance look-up tables. Look-up tables are two dimensional and dependent on the angle of attack and the Mach number. This approach provides a cost effective solution; however the interpolated coefficients depend on the resolution of the look-up tables from which they are formed. Rotor blades are exposed to nonlinearities which occur from reverse flow, shocks and dynamic stall effect all of which induce errors in the look-up table approach and usually corrections are employed to increase the accuracy. The unsteadiness of the flow in transient simulations are usually treated with thin airfoil based theories. Comprehensive tools generally employ the finite state inflow model of Peters to increase the efficiency of simulations, instead of filament based or sheet based free wake methods which take more time in the calculation of the rotor wake.

Helicopter blades are modelled as flexible beams since they have high aspect ratios. The aerodynamic loads that are calculated at the aerodynamic stations are then applied on the blade structure. The aeroelastic effects are included in the determination of the aerodynamic loads and depending on the aeroelastic deformations, kinematic positions and orientations of aerodynamic stations are recalculated and transferred into the aerodynamic interface. This process is iterative and performed at each Newton iteration in the nonlinear solution sequence.

In dynamic equilibrium, the net forces and the net moments with respect to the helicopter’s center of gravity have to be zero. This equilibrium condition is called as trim condition. To trim the helicopter both the main rotor and the tail rotor have to oppose the forces and the moments acting on the helicopter’s center of gravity. For the hover condition, in plane forces, the axial force, the pitching moment, the rolling moment and the rotor torque generated by the rotor disk should balance the forces and moments generated by the weight. The rotor torque generated by the main rotor causes a reaction torque on the helicopter frame in the opposite direction. This anti-torque is balanced by the moment of the thrust generated by the tail rotor with respect to the center of gravity.

Computational fluid dynamics have been both employed in two dimensional sections of the blades to find the force and the moment coefficients and in 3D CFD (Computational Fluid Dynamics) - CSD (Computational Structural Dynamics) coupling. In order to create the aerodynamic performance tables, wind tunnel test results and results from Navier-Stokes analyses are generally used. The tables are then used in the calculation of the aerodynamic loads at the blade stations. The aerodynamic loads are integrated along the blade sections to get the aerodynamic blade loads. The centrifugal load, spring and damper loads which come from the elastomeric bearing and the lead-lag damper are added to aerodynamic loads to get total loading on one blade as well as the Coriolis load and the weight. After summing all the blade loads, the rotor hub loads are obtained.

In the three dimensions, the CFD-CSD coupled computations are performed in two ways. The first approach is the loose coupling in which the data transfer between the aerodynamic stations and CFD is based on each period. In this approach, motions of the aerodynamic stations are transferred to the body conforming CFD grid after the rotor is rotated one period in the comprehensive simulation. Next, CFD solver outputs the load distribution at certain azimuths for the same rotation. Loads are then applied to the blades in the comprehensive simulation for the next iteration. These steps are repeated for one period till the solution is converged. The second approach is the tight coupling in which the data transfer is based on each time step. The loosely coupled comprehensive rotorcraft simulation is more widely used recently because of the fact that, the solution in CFD and the data exchange at each time step is computationaly more expensive in tight coupling. In the loose coupling, the velocities at the aerodynamic stations are transferred to the computational fluid dynamics code for each rotation of the dynamic rotor model used in the comprehensive analysis tool. CFD program calculates and outputs the loads at certain azimuth intervals. Then, these loads are distributed and used in the comprehensive analyses by the mechanical model.

On the other hand, structurally, a multibody system consist of bodies, joints, prescribed motions and forces. Using members of spherical joints, revolute joints, prismatic joints, universal joints, axial and torsional springs and dampers, beams for the lifting line to represent the blade span and rigid connection elements any rotor mechanism can be modeled. Initially each part of the rotor has 6 degrees of freedom. In order to see whether the system is constructed kinematically correct and does not have any clash or jamming during the operation of the mechanism, a kinematic anaysis should be performed before the dynamic analysis. In order to perform a kinematic analysis, total number of degrees of freedom of the system should be zero. Initially, parts have six degrees of freedom in 3D space. Joints between these parts constraint some number of degrees of freedom; for example, revolute joints contsraint five degrees of freedom on a part. Similarly, each rotational or translational motion prescribed on a joint constraints one degree of freedom of the system. At the end, constrained degree of freedom should be equal to the degree of freedom of the system and net degree of freedom of the system should be zero before the kinematic analysis.

1.2. Previous Work

At the stage of the design and the development of a helicopter, interdisciplinary analyses tools are required in order to predict the performance, the loads, the vibrations and the stability. For this purpose, many comprehensive analysis tools such as CAMRAD (Comprehensive Analytical Model of Rotorcraft Aerodynamics and Dynamics), RCAS (Rotorcraft Comprehensive Analysis System), COPTER (Comprehensive Program for Theoretical Evaluation of Rotorcraft-Bell Helicopters), RDYNE (Rotorcraft System Dynamics Analysis-Sikorsky), FLIGHTLAB (Advanced Rotorcraft Technology, Inc.), Dymore (Georgia Institute of Technology), UMARC (University of Maryland Advanced Rotorcraft Code), CHARM (Comprehensive Hierarchical Aeromechanics Rotorcraft Model) have been developed as mentioned in Johnson's historical study [1] on the comprehensive rotorcraft analyses tools. These comprehensive tools generally uses the blade element theory in the aerodynamic calculations. However, blade element theory is a two dimensional theory which excludes three dimensional effects. Induced flow which is caused by the rotation of the blades reduces the angle of attack. The induced flow can be taken as uniform and constant across the rotor disk and the rotor wake can be taken as rigid. This assumptions lead to the blade element momentum theory (BEM). Furthermore, the inflow can be calculated from the free wake models, the prescribed wake models or the finite state inflow theory of Peters [2]. Comprehensive tools generally use Peters dynamic inflow theory because of the fact that the uniform inflow cannot provide the desired accuracy and the free wake calculations require excessive computational times. The flow is highly unsteady on the main rotor in the forward flight because of the dynamic stall in the retreating side of the rotor disk where the reverse flow exists. Dynamic stall theories of Leishman-Beddoes [3] or ONERA-EDLIN [4][5] can also be used in the comprehensive analyses to improve the accuracy of the simulation.

Previous studies related to the rotor aerodynamics and the applied aerodynamics can be categorized into experimental studies and numerical studies. Experimental studies include the wind tunnel tests. Test data classification is dependent on the Mach number, the angle of attack and the Reynolds number and includes the assesment of airfoil profiles used for the blade sections of the isolated rotor. Numerical studies consists of the two dimensional CFD studies and the three dimensional CFD studies. Two dimensional CFD analyses are based on the studies which are conducted in two dimensional sectional profiles. The main aim is to find the aerodynamic coefficients using Reynolds Averaged Navier-Stokes (RANS), Euler or panel based flow solvers. It should be noted that the automatic generation of two dimensional aerodynamic performance tables with CFD is a preliminary work for this study. From another point of view, three dimensional RANS analyses include loose or tight coupling methodology between computational fluid dynamics (CFD) with computational structural dynamics (CSD) using overset grids, coupling of the vortex lattice method based free wake calculations with multibody dynamics calculations and hybrid methods. In hybrid methods, nearfield of the blade is calculated with Reynolds Averaged Navier Stokes (RANS) for a rotating body grid attached to the blade while the farfield is represented by the vortices over the filaments shed from the trailing edge of the blade. After the calculation of vortex strengths at the filament sections, the induced flow created by the vortex elements at the farfield is added to the lifting line. The purpose of the hybrid methods is to get rid of the computational cost that arises from the calculation of the state variables in large numbers of the farfield cell elements.

Previous studies related to the wind tunnel tests are given in this paragraph for NACA0012 and SC1095 profiles. Aerodynamic performance tables are prepared for an angle of attack range of -180^o to 180^o and the Mach number range of 0 and 1. Many wind tunnel tests have been performed for the NACA 0012 airfoil previously. There exists aerodynamic performance tables for NACA 0012 which is also used for this thesis to compare the analysis results with the numerical results. However, there is not enough information in the literature about test conditions used to generate the aerodynamic coefficient lookup table. Therefore, it is helpful to investigate the classification study conducted by Mccroskey [6]. Mccroskey classified over 40 wind tunnel test data with the considerations of lift curve slope, maximum lift coefficient, zero lift coefficient, drag coefficient, lift to drag ratio, drag divergence Mach number and pitching moment coefficient for the NACA 0012 airfoil. The test data are filtered and investigated in four groups around the numerical value of $\beta C_{l\alpha}$ which is presented in Equation (1) and to C_{d_0} which is given in Equation (2) and Equation (3) for the untripped boundary layer and for the tripped boundary layer respectively.

$$\beta_c C_{l_\alpha} = 0.1025 + 0.00485 \log\left(\frac{Re}{10^6}\right) \tag{1}$$

$$C_{d_0} = 0.0044 + \frac{0.018}{Re^{0.15}} \tag{2}$$

$$C_{d_0} = 0.0017 + \frac{0.91}{(\log Re)^{2.58}} \tag{3}$$

where β_c is the Prandtl-Glauert compressibility correction factor and expressed as,

$$\beta_c = \sqrt{1 - M_\infty^2} \tag{4}$$

Equations (1), (2) and (3) are derived by curve fitting to the experimentally scattered data. In the first group, experimental results with a tolerance of $\beta_c C_{l_\alpha} = \pm 0.0005$ and of $C_{d_0} = \pm 0.0002$ are filtered. Most noticeable tests in this group are conducted by Abbott et al [7], Ladson [8], Gregory & O'Reilly [9] and Green & Newman [10]. Critzos et al [11] have extended the wind tunnel results in the range of angles of attack between -180 deg to 180 deg for the Reynolds numbers of 0.5 and 1.8 millions. In the second group, experimental results with a tolerance of $\beta_c C_{l_\alpha} = \pm 0.004$ and of $C_{d_0} = \pm 0.001$ are filtered. Most noticeable test data in the second group belong to Harris [12]. These tests have been conducted between Mach 0.3 and 0.86 and for the Reynolds number of 3, 6 and 9 million. Third group covers the data which satisfy one of the conditions of the second group. It is stated that the most noticeable test data in the third group belong to Vidal. These tests are conducted between Mach 0.4 and 0.95 for the Reynolds number of 1 million. Data which do not satisfy both of the conditions of the second group constitute the fourth group. It can be considered that the currently existing c81 performance table for the NACA 0012 profile is generated by the combination of these data. Totah [13] has also made a similar classification for the main sectional profile of the UH60 main rotor blade (SC1095) based on 9 wind tunnel tests as McCroskey did for the NACA 0012 profile. Similarly, Bousman [14] has also made an assessment for the aerodynamic characteristics of the SC1095 profile based on 10 wind tunnel tests. In this thesis study, NACA 0012 airfoil profile is used as the main rotor blade profile because of the availability of pitching moment table data for NACA 0012 in the initial steps of the study instead of UH60 main rotor blade profile, SC1095, which is also a symmetrical airfoil.

Smith et al. [15] carried out sectional CFD analyses for the SC1095 airfoil using OVERFLOW, FUN2D, Cobalt LLC and TURNS with SA turbulence model and CFL3D with Baldwin-Lomax turbulence model. Used programs, grid types, grid properties and turbulence models used in this study are summarized in Table 1 [15].

Table 1 CFD Codes, Grid Properties and Turbulence Models of RANS Analyses Carried out for the SC1095 Airfoil by Smith et al. [15]

CFD Program	Grid Type	Domain Size	Surface Points	Turbulence Model
OVERFLOW [16]	S	297x81	225	Spalart-Allmaras
FUN2D [17]	U	29000	314	Spalart-Allmaras
CFL3D [18]	S	257x129	193	Baldwin-Lomax
Cobalt LLC [19]	S	600x150	400	Spalart-Allmaras
TURNS [20]	S	217x91	145	Spalart-Allmaras

Because of the computational costs of RANS analyses, Smith et al. also performed calculations with a less costly program named as MSES [21]. MSES is a design and analyses tool for the airfoil profiles. It is developed in Massachusets Institute of Technology by Mark Drela. The program uses finite volume discretization in the streamwise direction and it solves steady euler equations. Viscous boundary layer effect is included by coupling the inviscid solution with an integral two-equation lagged dissipation equation. Smith et al. have validated their analyses with 10 wind tunnel experiments which Totah had investigated for Mach numbers of 0.4 and 0.7. They have performed analyses for three different Reynolds number, Mach number multiplied by $12.5*10^6$, Mach number multiplied by $12.5*10^6$ and divided by 1.67 and Reynolds number of 6.5 million. They have correlated the lift coefficients obtained from Navier-Stokes analyses with the wind tunnel results and found out excellent match between the lift coefficients. Similarly, for the pre-stall region they have achieved similar correlation with the MSES results. Smith et al. have come across with a problem of early stall in the TURNS calculations, which is a transient unstructured Navier-Stokes solver, and they have solved this problem with grid refinement. Then, Smith et al. have compared lift curve slope of Mach 0.4 and Mach 0.7 calculations with McCroskey's [6] equation for the lift curve slope given in Equation (1) which is used when grouping wind tunnel test results for the NACA 0012 airfoil.

According to the same study conducted by Smith et al., all lift curve slopes multiplied by the compressibility correction factor are found out to be less than the McCroskey's limit. Secondly, they have compared the maximum lift coefficient and the angle of attack at which the maximum lift occurs. For the Mach number 0.4, maximum lift coefficient is calculated by taking the mean of the five group of the computational data as 1.355 with a deviation of 0.10 and it is compared with the mean value of the wind tunnel tests data calculated as 1.19 with a deviation of 0.07. Moreover, the maximum lift location for Mach 0.4 is within the experimental limits however after Mach 0.6, calculations are not sufficient to predict the stall location corresponding to the experimental wind tunnel data sets. Thirdly, this study states that pitching moment is important because it mainly affects the vibratory loading on the helicopter main rotor. They have compared the pitching moment considering the maximum pitching moment and its break location where the pitching moment becomes negative. It is stated that the poor results are obtained for transonic Mach number and also stated that there exist significant differences between maximum pitching moments and also pitching moment break locations. It is specified that beyond the transonic regime the pitching moment becomes negative and this implies that the aerodynamic center is travelling towards the trailing edge. Similar to the lift coefficient, the drag coefficient obtained in the calculations have close correlation with the experimental data in the linear region at Mach numbers of 0.4 and 0.7. As for the zero lift coefficient, McCroskey fitted the wind tunnel experimental data of no boundary layer trip in Equation (2) for the zero-lift drag coefficient. Smith et al. re-developed this equation for the experimental data of the SC1095 wind tunnel test data as given in the Equation (5).

$$C_{d_0} = \frac{0.026}{Re^{0.08}} \tag{5}$$

It has been found out that analyses data for the zero-lift drag coefficient is higher than the experimental data obtained from Equation (5) especially for higher Mach numbers. Also, the drag divergence Mach number and the maximum lift to drag ratio are also two parameters compared in the study. Drag divergence Mach number is calculated when the change in the zero-lift drag coefficient becomes 0.01 or the slope of drag becomes 0.002. Drag divergence Mach numbers came out to be less than the experimental values. Original drag divergence Mach number is 0.809 while the mean of CFD computations is 0.764 according to study of Totah [13] for the SC1095 airfoil. Lastly, Smith et al. have compared the maximum lift to drag ratio by simply fitting a second order curve passing through the maximum experimental lift-to-drag ratio of each Mach number. They found out that the computational values are lower than the experimental values for the L/D ratio. Furthermore, they made case studies for the effect of the trailing edge geometry, the effect of turbulence models and the effect of grid refinement. Smith et al. have found out that the closed trailing edge geometry does not affect values significantly with %1-3 change. They also performed computations in FUN2D and Cobalt LLC codes with coarser grids (500x100, $\Delta n=1\times10^{-5}$). The grid refinement study proved that there is no need for a finer grid since it is computationally more costly while the accuracy gain in the coefficients is insignificant. The most effective turbulence model is determined as Spalart-Allmaras model in these case studies. Detailed conclusions are drawn for the aerodynamic performance parameters considering case studies is given in reference [15].

Mayda and Dam [22] automatized the generation of the airfoil performance tables with Navier-Stokes analyses for the SC1095 airfoil. They have performed steady state and transient analyses at a Reynolds number of 6.5 million with Spalart-Allmaras turbulence model, used O-grid topology and picked y+ value less than 1. They have set computational domain with 392 point on the airfoil surface and 153 points in the extrusion direction and a farfield at 45 chords and performed analyses in ARC2D [23] which is a two dimensional compressible RANS solver which is discretized in finite difference formulation. In this study, it is stated that the two dimensional computation is started steady initially. If the convergence is not achieved in the steady state analysis, the analysis is switched to a time dependent transient analysis. They have used XFOIL to predict the transition location on airfoil surface before performing a transient analysis. The transition was forced at 0.1 of chord on the top surface of the airfoil. Critical turbulence amplification factor, n_{crit} was selected as 9. After the transition location is found in XFOIL, it is prescribed in ARC2D in the transient analyses. The transient analyses are accomplished with dual time stepping methodology. If the program recognizes steady pattern in time dependent analysis, the analysis is assumed to be converged and coefficients are obtained. It is also specified that around the region before stall, solver cannot decide whether the analysis should be started as steady or transient. In this case, the analysis is started as steady first, then switched to transient when residuals show divergence. The author also states that there are cases on the domain which lies in the border between the steady and the unsteady. Therefore, solution obtained from automatization of these cases are not fully reliable. As given in Mayda's work, there are three types of calculations namely steady, time dependent and mixed of steady and transient and the combination of the steady and the transient analysis. Mayda and Dam stated that for the cases which is known to be exactly steady or transient are mainly prescribed by the user initially. As in the study of Mayda and Dam [15], the aerodynamic performance parameters are compared with the classified parameters for the SC1095 airfoil by Bousman[14] with the considerations of McCroskey's. Firstly, the lift curve slope is found out to be larger than the experimental values almost at all Mach numbers. The lift curve slope obtained by using Spalart-Allmaras turbulence model presents an overshoot around Mach 0.7. This overshoot is reduced slightly by employing Baldwin-Barth (BB) turbulence model. They also examined zero-lift angle of attack which should be zero for the symmetric airfoils, the experimental values and ARC2D results show similar constant behavior up to Mach 0.85. The difference is that ARC2D gives -0.5 degree of negative angle of attack for zero-lift coefficient while the experimental values are scattered between 0 and -1 degrees of angle of attack. Zero-lift drag coefficient for all Mach number seems to be in good correlation for the SA turbulence model while the zero-lift drag coefficient is predicted lower than the experimental values in BB turbulence model. It is also noted that the results obtained from the CFD predicts the drag divergence Mach number correctly as it is seen from the sharp increase around Mach 0.8 in the zero-lift drag versus Mach number plot (Fig. 6 of Ref [22]). For zero-lift pitching moment coefficient (C_{m_0}), the author stresses that the increase in Mach number decreases the zero-lift pitching moment and points the lack of reliable pitching moment test data. After Mach number 0.8, related to transonic flow and shocks, the zero-lift pitching moment shows nonlinear behavior. The pitching moment curve slope shows constant behavior up to Mach number 0.6. The break point occurs in the pitching moment curve around Mach 0.75 and around Mach 0.8, the pitching moment coefficient becomes negative. It can be inferred from this study that the pitching moment data is in good correlation with the experimental data below Mach 0.8. It is also reported that both of SA and BB turbulence models performed similarly for the pitching moment coefficient in all Mach range. Between Mach numbers of 0.3 and 0.55, the maximum lift coefficient obtained from the ARC2D results, shows good agreement with the experimental scattered data. For Mach numbers less than 0.3, the maximum lift coefficient is found out to be on the lower bound of the experimental scatter. For Mach numbers around 0.55, the maximum lift coefficient occurs at 22 degree angle of attack and the maximum lift coefficient increases dramatically while the experimental data tends to decrease after Mach 0.55. Lift to drag ratio fits well with the experimental values for Mach 0.4 and 0.8. Automated computations found out the drag divergence Mach number M_{dd} as 0.797, while in Bousman experimental data classification study for the SC1095 profile proposes that the mean of the drag divergence Mach number is 0.814. The drag divergence Mach number is predicted from the slope of the drag coefficient versus the Mach number curve at which the slope equals to 0.1. With a comparison with the existing c81 table for the SC1095 airfoil, numerical computation predicts higher lift coefficient around the stall region and slightly higher around the linear region. Also, it predicts the maximum lift coefficient with approximately 2 degree delay from the c81 table at Mach 0.4. The break point of the pitching moment and the drag divergence also differs with a 2 degree delay from the c81 table. For the Mach number 0.4, unsteady calculations are performed starting from 13^{o} angle of attack.

Potsdam, Yeo and Johnson [24] showed that significant improvements on the prediction of the aerodynamic loading on the main rotor blades have been achieved in recent computational fluid dynamics (CFD) - computational structural dynamics (CSD) coupled simulations. It is stated that the CFD is used simultaneosly with the multibody dynamics tools to obtain high fidelity airloads and to include the blade aeroelastic deformations in the comprehesive flight simulations. The CFD-CSD coupling process can be loose coupling based on load and motion exchange at each period or tight coupling based on load and motion exchange at each time step of the simulation time interval. According to Potsdam et al. problems arising in helicopter flow can be assessed in mainly four categories. These are the unsteady flow, the reverse flow on retreating blade, the transonic flow which causes shocks at the blade tips and the dynamic stall due to oscillatory flapping motion and lead-lag motion of the blades which generally exists in the retreating blade. Furthermore, most critical cases are specified as helicopter in low speed with advance ratio of 0.15 in which rotor has blade vortex interaction, helicopter in high speed with advance ratio of 0.37 in which rotor has negative lift in advancing blade side, helicopter in high thrust with advance ratio of 0.24 in which dynamic stall is observed on the blades and helicopter in hover. Due to the fact that these cases are critical, the hover condition is selected for the isolated rotor simulation in this thesis study. In the study of Potsdam, Yeo and Johnson, a comprehensive analyses tool CAMRAD II is loosely coupled with OVERFLOW-D which is a three dimensional finite volume based CFD solver developed by NASA. UH60 main rotor is modeled in CAMRAD II. For the first rotation, the rotor is rotated with its internal lifting line aerodynamics; that is, the trim condition is reached using the look-up table aerodynamics. Next, the motions of aerodynamic stations dependent on the azimuth and the radius, are transferred into the CFD code, OVERFLOW-D for one blade. It is stated that the CFD code outputs surface grid and the state variables at intervals of 5^o azimuth. From the surface grids and the state variables, the normal force, the pitching moment and the chord force are obtained with respect to the azimuth and the radius. In the next iteration, the difference between the aerodynamic loads obtained from the CFD and from the lifting line solution from the previous iteration, called as delta airloads, are added to the internal lifting line aerodynamics and applied to the structural dynamic model. The comprehensive simulation is performed with the aerodynamic loads obtained from the lifting line plus a correction which comes on top of the trim condition of the previous turn which is the delta airloads. This procedure is repeated until the convergence is achieved. In the referred study, a structural cartesian grid is used for the background domain and an overset structured C type grid is used for the blade. The overset grid is divided into three zones for the tip, root and the middle sections of the blade in order to catch the tip vortices and the root effects. Chimera grid tool is used for the grid generation. This overset blade grid can deform aeroelastically according to the motion of the blade. On the blade surface, leading edge spacing is set to 0.001 of the chord length and trailing edge spacing is set to 0.002 of the chord length. On the blade surface, there are 201 seed points. First the wall thickness is selected so as to take the y+ value less than 1. The background grid has 26.1 million elements; 45 percent of which is located near the blade and 55 percent of which is located far from the blade. The step size is adjusted so that the azimuthal spacing becomes 0.05 degrees. In an another study by Zaki [25], the tight CFD-CSD coupling procedure is investigated. Advanced methods on the tight and the loose CFD-CSD coupling for the rotor trim condition. Hybrid unstructured RANS coupled freewake method are investigated later by Reveles [26]. Both the structured and the unstructured meshed domains are modelled in the solution of the rotorcraft simulation. A CFD/CSD coupling between FUN3D and CAMRAD II is also provided in reference [27].

According to another study performed by Smith et al [28], one of the aerodynamic problems is expressed as the blade vortex interaction (BVI) caused by advancing blade of the rotor disk. In this study, the effect of the blade vortex interaction (BVI) is investigated with the CFD-CSD coupled programs using two-equation turbulence models or detached eddy simulation (DES) models. Mesh refinement and spatial discretization schemes are configured to capture the blade tip vortices. It is stated that the hybrid Navier-Stokes/Lagrangian wake methods are less accurate than the full CFD/CSD methods. They have investigated the blade vortex interaction using loosely coupled codes; CAMRAD II with OVERFLOW, FUN3D and KFLOW, DYMORE 2 with GENCAS (Generic Numerical Compressible Airflow Solver), DYMORE 4 with FUN3D, RCAS with NSU3D-SAMARC, UMARC with TURNS (Transonic Unsteady Rotor Navier-Stokes).

Wachpress, Quackenbush and Boschitsch [29] present methods embedded into CHARM in the calculation of the free wake geometry and the flow induced by the wake elements on the blade lifting line. CHARM (Comprehensive Hierarchical Aeromechanics Rotorcraft Model) is a comprehensive analyses tool for the rotorcraft which uses harmonic balancing for the periodic trim simulations and time integration for the aperiodic flight simulations such as maneuvers. CHARM is mostly used for acoustic and performance calculations which are usually related to blade vortex interaction. In CHARM, both the trailed (spanwise) and the shed (temporal) vortex filaments are generated along the blade during rotation. The bound circulation is divided into primary zone and negative circulation zone at the tip. These filaments have equal and constant vortex strengths through the zone contours. This wake model is called as the constant vorticity contours (CVC). CHARM employs a periodic base relaxation methodology in order to save from computational time. It updates the wake geometry at the end of each rotation. Each element of the vortex filament can have an influence over another element which allows the filaments to deform freely under the influence of the induced velocities. Induced velocities are calculated by using Biot-Savart law. The effect of induced velocities of the downstream wake elements are integrated towards the upstream wake elements. Rolled-up tip and root vortices in the blade are formed automatically under the influence of the wake elements. Structurally, the blades are depicted as first order linear finite elements with modal information. Vortex core model and the induced velocities are modelled in Equation (1) of reference [29] which is first introduced by Scully [30] and developed by Vatistas [31]. CHARM also uses panel method to model the other structural surfaces of the helicopter such as a vertical fin, a horizontal fin, the fuselage or the ground.

Running a comprehensive analysis tool requires sectional CFD solutions to determine the aerodynamic performance coefficients. In order to decide on the accuracy of the performance coefficients, experimental test data should be examined for the used airfoil profiles. Hence, in this section, classification of wind tunnel test data of NACA 0012 and SC1095 airfoils, which are also used in the thesis, are also investigated. Furthermore, in order to be familiarized in the field and in order to use them in future studies, recent studies related to the comprehensive simulation tools and the coupling of the comprehensive simulation tools with the three dimensional CFD solvers or potential flow based free wake methods are provided in this section.

1.3. Objective

In the comprehensive rotorcraft analysis, the blade element theory is widely used. In this method, the aerodynamic center of each section along the blade span constitutes a lifting line. At each aerodynamic center, aerodynamic loads are interpolated according to the sectional angle of attack and the Mach number. This interpolation is calculated from the two dimensional aerodynamic performance tables. Wind tunnel tests and the two dimensional CFD analyses are generally carried out in generating these look-up tables. It is needed to have an airfoil performance table for each airfoil profile to be used throughout the blade span. Hence, in case of an airfoil profile optimization, aerodynamic tables are required for each perturbed profile.

In this study, an opensource multibody dynamics simulation tool, Dymore, is coupled with an open source panel based airfoil design and analysis tool, XFOIL, and an open source unsteady viscous Reynolds Averaged Navier-Stokes (RANS) solver, SU2, in order to swap the aerodynamic performance look-up tables used in the comprehensive analyses with the instantaneous sectional panel or CFD solutions. The main aim of the present study is to integrate an independent aerodynamics solver into a multibody dynamics solver so that the multibody solver can be used seamlessly in the aerodynamic optimization of the blade profile to minimize the rotor power for the same trim targets in forward flight condition. It should be noted that in the aerodynamic profile optimization for the helicopter blade, the aerodynamic coefficients have to be calculated from the aerodynamic analyses for each perturbed section since the lookup tables are only available for a specified airfoil profile. Aerodynamic optimization of the blade is the follow-up study of the present work once the seamless integration of the multibody dynamic solver Dymore with the aerodynamic solver has been achieved successfully.

1.4. Content

Chapter 1 is dedicated to an overview to the field of the study, literature review and the study objective. Chapter 2 is given for the related theories in the comprehensive rotorcraft analysis; such as rotor dynamics and rotor aerodynamics. Also, the methodology for the multibody formulation is given in this chapter. A multibody dynamics program used in this study, Dymore, and the dynamic rotor model are introduced and the solution parameters are given. Then, the aerodynamic theories related to rotorcraft and CFD are roughly reviewed. The panel based solver, XFOIL and the RANS solver, SU2 are introduced and grid parameters and solution parameters used in the CFD and the panel analyses are given. Additionally, coupling methodology between the CFD and the MBD code Dymore is provided in this section. In Chapter 3, results for the two dimensional CFD analyses are given as validation studies for an operational range of blades in terms of the angle of attack and the Mach number. Also, the CFD results are compared with the look-up table solutions. In this chapter, simulation results for coupled simulations are also presented and compared for the hover simulations. In Chapter 4, conclusions are drawn and future work is introduced as an optimization study.

CHAPTER 2

METHOD

In this chapter, theories related to rotor dynamics and aerodynamics are presented in section 2.1. Rotor dynamics section starts with the classification of rotor types in terms of the articulation and the natural frequency of the 1st chordwise bending mode of the rotor which are grouped as soft-in-plane or stiff-in-plane. Analytical dynamic equations related to the flap-lag and torsional degrees of freedom of blades and related natural frequencies to these dynamics are given. Secondly, the multibody formulation for kinematic chains based on Lagrangian dynamics is given in section 2.2. Also, the dynamic rotor model generated in the MBD tool is provided. Section 2.3 basically covers inflow theories and blade element theory used in analytical calculation for the sectional lift, drag and moments. In section 2.4, CFD solvers, general formulation and used parameters are given for XFOIL and SU2 by specifying the panel model and the computational grid. In section 2.5, comprehensive analysis methodology using the look-up table aerodynamics and coupled simulations are provided. Finally, coupling methodology between the CFD and the flexible MBD and its parallelization are given in section 2.5.

2.1. A Review of Rotor Dynamics

Helicopters are categorized in terms of the configuration of the rotors such as tiltrotor, tandem, coaxial, autogyros and conventional helicopters with one main rotor and one tail rotor. Tiltrotors are air vehicles which allow making both vertical and horizontal flight. An example to tiltrotor configuration is given in Figure 1.

Figure 1 Bell-Boeing V22 Osprey [32]

Tandem rotors have two rotors connected to each other with mechanical linkage. In this configuration, the rotors rotate in the opposite directions to balance the torque created by the each other; otherwise in a single rotor case the torque created by one rotor should be balanced by the tail rotor. They are mainly used for cargo purposes. CH-46 is an example to tandem rotors and it is given by Figure 2.

Figure 2 CH-46 Sea Knight [33]

Also, in the tandem configuration, to prevent one of the rotor hitting the other rotor, a mechanical linkage is used to ensure the coordinated rotation. Main advantage of this type of rotor is that all the thrust generated is used to create the lift unlike that in convential helicopter one rotor creates thrust to prevent the anti-torque. Coaxial rotors have two large axial rotors located on the main shaft. They rotate in the opposite directions. They are used for heavy lifting operations. One disadvantage is the mechanical complexity of the rotor hub. A coaxial rotor can be seen in Figure 3.

Figure 3 Kamov Ka-32A-12 [34]

Autogyros have no engine to drive the main rotor, instead they have engine to drive the propeller located at the back which pushes the rotorcraft forward. Rotor is automatically driven under the effect of the oncoming flow and by this way lift is generated. An example to the autogyro is given in Figure 4.

Figure 4 AutoGyro MTOsport [35]

Also, there is another configuration called as NOTAR (no tail rotor) in which the air is blown from the tail cone to generate thrust for the anti-torque instead of generating it by the tail rotor. Figure 5 shows an example to the no tail rotor configuration. As shown in Figure 5, black part placed in the rear of the helicopter is the place where the air is blown.

Figure 5 MD Explorer [36]

These solutions are developed to eliminate the disadvantages of the tail rotor. A tail rotor increases the power loss generated by the engine. It amplifies the structural failure risk since it operates in high speeds. Similarly, the possibility to hitting obstacles decreases the safety and the security in human transport. On the other hand, a conventional helicopter has one main rotor, one tail rotor, transmission, engine, fuselage, vertical and horizontal fins, landing gears as well as many critical systems such as rotor flight control system, automatic flight control system, environmental control system, electrical subsystems and hydraulic subsystems etc.

2.1.1. Rotor Types

Rotors are classified according to their kinematic architecture as articulated, teetering, gimballed, hingeless (semi-rigid) or hingeless and bearingless. In an articulated rotor, flap, lead-lag and feathering hinges exist. Fully articulated rotor of CH53G is given as an example to the articulated rotor in Figure 6. The disadvantages of this rotor type is the mechanical complexity and the probability of wear due to high cycle fatigue.

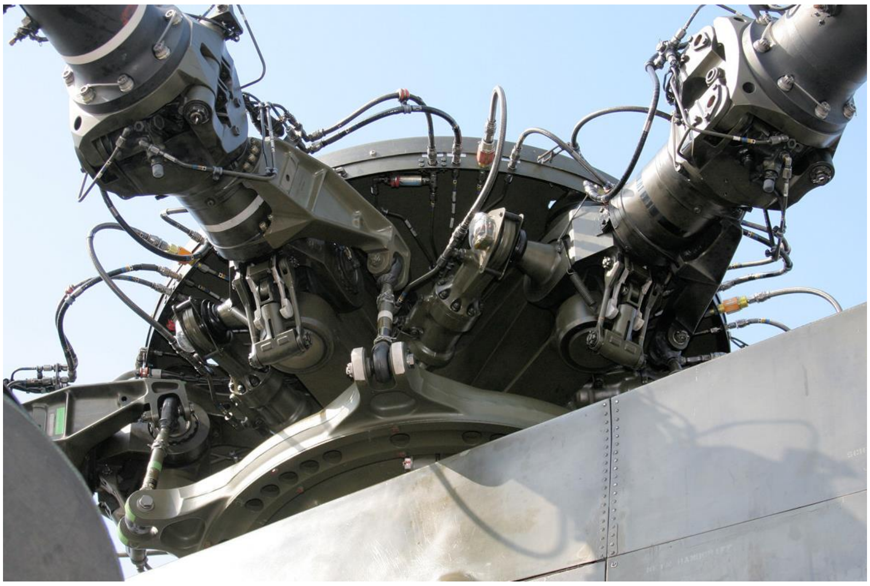

Figure 6 Fully Articulated Main Rotor - Sikorsky CH53G [37]

In the teetering rotor, there is no lag hinge and two blades forms a continuous structure sharing the same flapping hinge. Also, in the teetering rotor flap hinge is located at the center of the rotor disk. An example to the teetering rotor can be given as R22-Robinson helicopter in Figure 7.

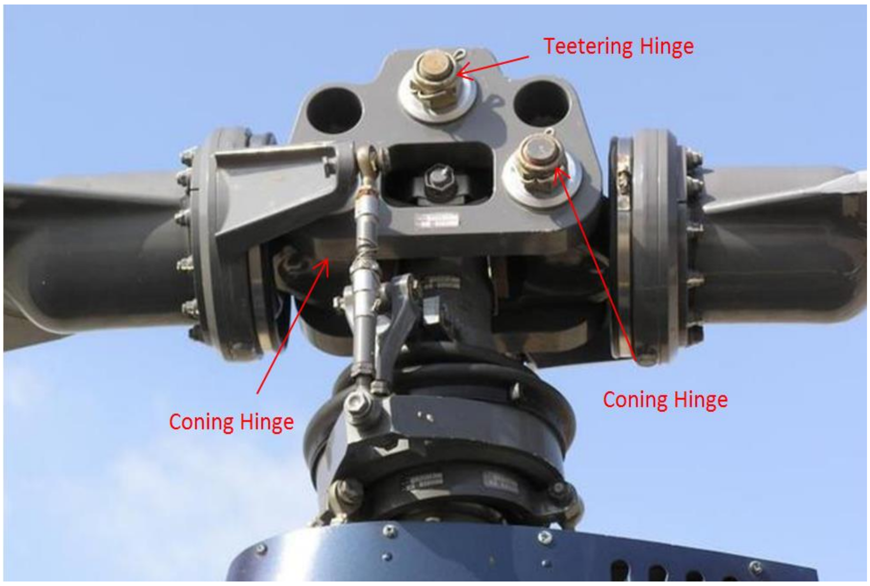

Figure 7 Teetering Main Rotor - Robinson R22 [38]

In the hingeless rotor, there are no flap and lag hinges; however, pitch motion is prescribed around a bearing. Flapwise and chordwise moments are relieved by the flexible structure of the retention links. Retention links are connected to the rotor hub and the root of the blades. In this configuration, blades can be considered as cantilever beams which are clamped at the root. An example of the hingeless rotor is the BO105 main rotor given as in Figure 8.

Figure 8 Hingeless Main Rotor - BO105 [39]

In the hingeless and bearingless rotor type, no flap and lag hinges or pitch bearings exist as seen in Figure 9. Composite flexible straps enable pitch, lead-lag and flap motions.

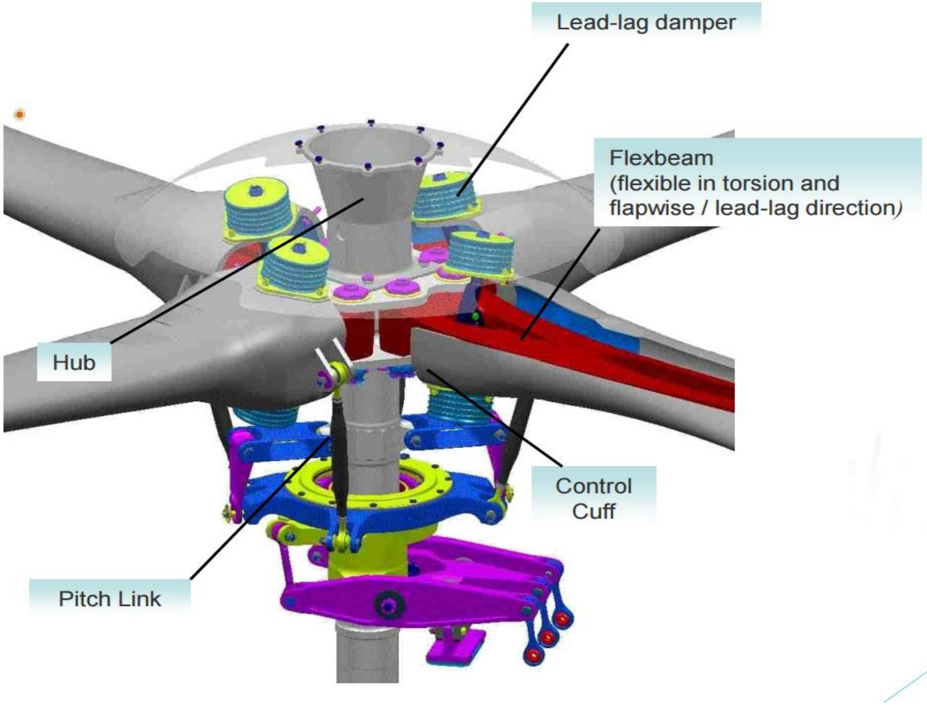

Figure 9 Hingeless and Bearingless Type of Main Rotor of EC135 [40]

In gimballed rotor configuration, more blades are connected to the rotor hub. There is a gimballed connection between the rotor hub and the rotor shaft. The gimbal is represented with a universal joint between the rotor hub and the rotor shaft.

Rotor are also categorized according to lag frequencies named as stiff in plane and soft in plane. If the nondimensional lag frequency is higher than 1 which means that lag frequency is higher than the rotational speed, the rotor is called as stiff in plane. If the lag frequency is less than the rotational speed, then it is called as soft in plane. There are both advantages and disadvantages of the soft in plane and the stiff in plane rotors. Stiff in plane rotors cause high frequency vibration and the noise. They are also more prone to structural damage. In stiff in plane rotors, coupling of 1st lag mode with 1st flap mode can be observed. This may cause flap-lag instability. On the other hand, soft in plane rotors comprises the rotors which have lead-lag hinge. The movement of the center of gravity of the blades in the lead-lag direction is higher in these rotors. This motion causes a phenomenon called ground resonance. In the soft in plane rotors, first mode shape which corresponds to the lowest frequency is the chordwise. Lowest chordwise bending frequency can create an excitation and can be amplified around the center of gravity of the helicopter and may cause crash during landing or take-off.

In rotor dynamics, the origin of the helicopter system is generally placed at the nose of the aircraft. Inertial coordinate frame is placed so that the x direction points the tail in longitudinal direction and the z direction points positive upwards from the ground. From the right hand rule y axis points the starboard direction of the helicopter. With respect to the inertial reference frame, the x coordinate is called as stationline, y coordinate is called as the buttline and z coordinate is called as the waterline. Other coordinate systems used in the calculations and the analyses are body moving frame, hub frame, wind axis frame and control frame. Vehicle carried frame is a coordinate system which has an origin at the rotorcraft cg. It points to the north, the east and to the earth, in x, y and z directions accordingly. The vehicle carried frame is not a rotating frame while the body moving frame rotates with the vehicle and the origin of the body moving frame is at the helicopter cg and points to the nose, starboard and toward the center of earth, in x, y and z directions respectively. Body moving frame is used in the trim analysis and the flight simulations. Coordinate systems are given in Figure 10.

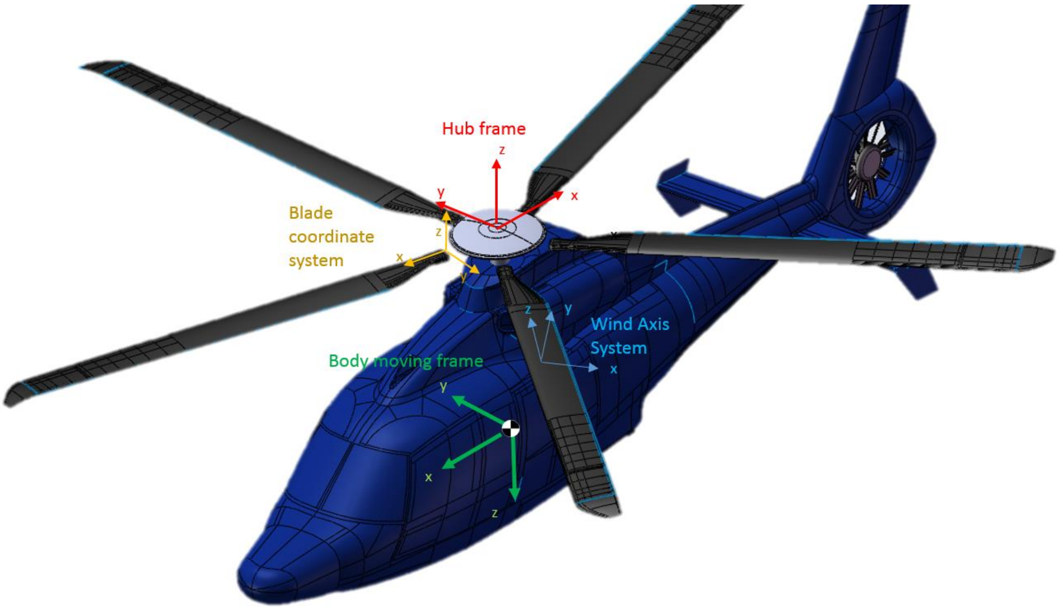

Figure 10 Coordinate Systems used in Comprehensive Analysis [41]

Aerodynamic loads are calculated with respect to the wind coordinate axis in which x direction points in the flow direction, z direction points in the radial direction and y is perpendicular to x direction. The calculated airloads are converted to blade coordinate system and integrated throughout the blade span. The blade coordinate system is located at the root of the blade and x direction points in the radial direction, y direction points in the leadwise direction and z direction points in the axial direction parallel to the rotor shaft. Then, the blade loads are summed in the rotating hub frame and converted into the nonrotating hub frame. These nonrotating hub loads are then used in the trim analyses.

There are also reference planes which are used in the comprehensive analysis. Tip path plane (TPP) is a reference plane to describe the flapping angle which is calculated by Equation (6). The trajectory of the blade tips constructs the tip path plane.

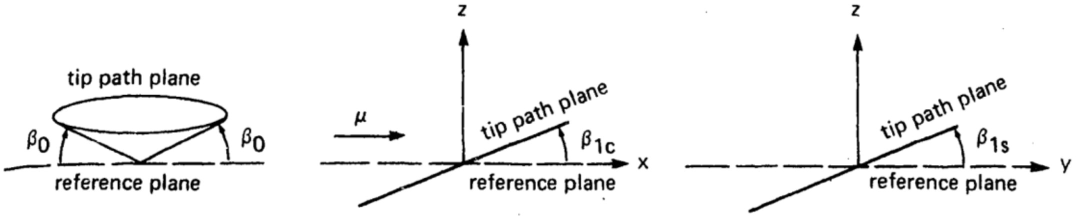

a) Coning Angle, β_0 **b) Longitudinal TPP Tilt, β_{1c} (view from left)** **c) Lateral TPP Tilt, β_{1s} (view from aft)**

Figure 11 Interpretation of Tip Path Plane and Flapping Angle [42]

Thrust vector direction is perpendicular to this plane. Generally rotor shafts have approximately 5^o inclination towards to the nose of the aircraft because of the optimized orientation of the fuselage with respect to the aerodynamic drag in the forward flight. The hub plane is taken as perpendicular to the rotor shaft axis. In the reference hub frame, z direction points axially outwards coincident with the shaft, y direction points right and from the right hand rule x direction points the tail cone with 5^o inclination from the horizontal plane. There is also no feathering plane (NFP) which is perpendicular to the view at which the pitch angle difference between blades are zero and henceforth the cyclic variation is zero. In order to understand the cyclic and the collective input distribution, flapping (β) and the pitch angle (θ) distributions with respect to the azimuth are given in Equations (6) and (7).

$$\beta(t) = \beta_0 + \beta_{1c}\cos(\psi) + \beta_{1s}\sin(\psi) \tag{6}$$

$$\theta(t) = \theta_0 + \theta_{1c}\cos(\psi) + \theta_{1s}\sin(\psi) \tag{7}$$

First term of the flapping equation stands for the coning angle and the first term in the pitch angle equation stands for the collective input. Second term of the flapping equation is the longitudinal cyclic angle which shows the tilt of TPP forward or backward so that the thrust vector is pointed in the longitudinal direction. Third term of the flapping equation is the lateral cyclic angle which shows the tilt of TPP rightward or leftward so that thrust vector is pointed in the lateral direction.

The second term and the third term of the pitch equation stand for the lateral and the longitudinal cyclic inputs respectively. Corresponding lateral and longitudinal coefficients of flap and pitch equations are crossed because of the fact that there is a 90 degree phase angle between the flap and the pitch angles. If a collective input is given to the blades, the flapping angle of the blades increases because of the increase in the lift. The angle between the hub plane and the blades is called as the coning angle when there is no cyclic input. In this case, there is a 90 degree phase angle between the pitch input and the flap angle because of the gyroscopic effect. This can be explained by the fact that giving maximum pitch angle at one azimuth through the tilt of swashplate causes the maximum flapping of the blade at an azimuth 90^o after the input is received. The swashplate and the blade pitch control arms adjusted so as to decrease or eliminate the phase difference. If the flap, lag or feathering axes of the blade are not orthogonal to each other, there can be couplings between the flap, the pitch and the lag motions. In this case, rotation axes are not pure.

Operational conditions for a helicopter can be considered in the groups of axial flight, level flight, transient maneuvers and autorotation. The axial flight includes the hover, the climb and the descent flight conditions. The hover condition can be stated as the equilibrium condition of the helicopter having no translational or rotational motion. In the comprehensive simulations, solutions are obtained for the periodic conditions such as hover, climb or level flight by using the method of harmonic balancing or the time integration. On the other hand, forward flight is considered as constant velocity and constant altitude flight also called as level flight. In level flight, the velocity distribution on the retreating side and the progressing side of the rotor disk is not equal because of the forward speed as seen in Figure 12.

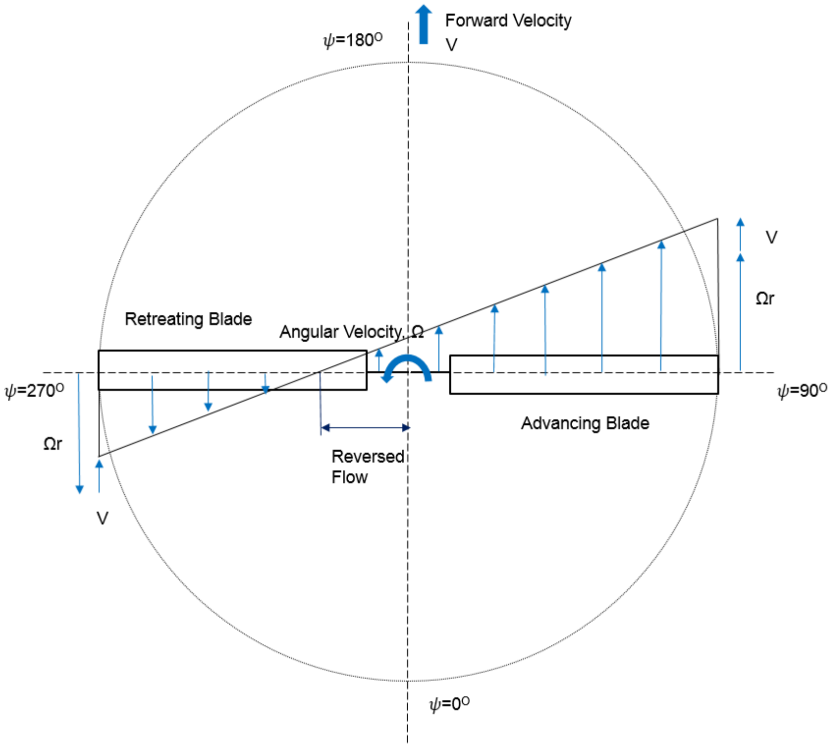

Figure 12 Velocity and Lift Distribution in Forward Flight

This causes inequal lift distribution and a rolling moment around the longitudinal axis of the hub frame. This moment is relieved with a flap hinge. This fact is first proposed by Renard in 1904 and applied by Cierva in 1920. Similarly, during the flapping motion the center of gravity of the blades moves closer to the hub. From the conservation of angular momentum, decrease in the radius requires an increase in the rotational speed. The blade accelerates to increase the rotational speed and lead motion is observed. When the blade decelerates, lag motion is observed. This is governed by Coriolis force acting on the rotor blades acting in the tangential direction. Coriolis force exists when there is a relative motion in a rotating frame.

According to Theodorsen [43], loads acting on a blade are due to inertial loads, aerodynamic loads and restraint loads. In cylindrical coordinates, from dynamics point of view acceleration of a point with respect to the center of hub frame is given by Equation (8). This equation actually presents the inertial loads acting in a rigid body.

$$\vec{a} = \vec{a}_{ref} + \dot{\vec{\Omega}} \times \vec{r} - \Omega^2 \vec{r} - 2\vec{\Omega} \times \vec{v} \tag{8}$$

First term of Equation (8) is the acceleration at the origin of the reference plane. Second term stands for the rotational acceleration or the deceleration, third term stands for the centrifugal acceleration which stiffens the blades and prevents them from dropping and fourth term stands for the Coriolis acceleration. These terms represents inertial loading while aerodynamic loads or restraint loads are external loading.

2.1.2. Flap Dynamics

Aerodynamic loads are mainly the lift, the drag and the pitching moment while the restraint forces are springs, dampers, preapplied forces and moments. A second order equation of motion can be written for flapping dynamics for a rigid blade. Inertial loads acting on the blade are the tangential inertial force and the centrifugal force and due to the flapping. On the other hand, the aerodynamic load acting on the blade is only the lift force. Restraint forces are hinge offset, elastomeric spring stiffness in the flapping direction and the preconing. Figure 13 shows the forces and moments acting on the blade in flapping dynamics.

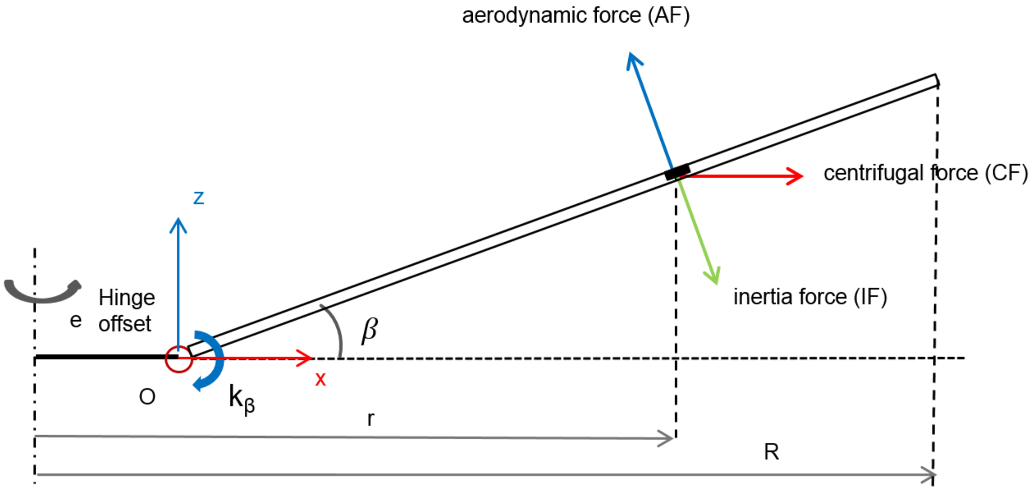

Figure 13 Forces and Moments Acting on the Blade in Flapping Dynamics

Analytical solution for flapping dynamics can be obtained from a second order equation. Dimensional flap equation for the hover condition can be simply written as by writing total moment around the hinge point by summing the moments of all the acting forces on discrete elements along the blade.

$$\left(\int_e^R m(r-e)^2\,dr\right)\ddot{\beta}+\left(\int_e^R m\Omega^2 r(r-e)\,dr\right)\beta \\ -\int_e^R F_{aero}(r-e)\,dr+k_\beta\left(\beta-\beta_p\right)=0 \tag{9}$$

where β_p is the precone angle which is prescribed to the blades by installation.

The flapping equation can be simplified into Equation (10) for a rigid blade for the level flight or the hover condition. The aerodynamic moment is given by Equation (63).

$$\ddot{\beta}+\Omega^2\left(1+\epsilon+\frac{k_\beta}{\Omega^2 \mathrm{I}_\beta}\right)\beta+\frac{k_\beta}{\mathrm{I}_\beta}\beta_p=\frac{M_{aero,flap}}{\mathrm{I}_\beta} \tag{10}$$

where;

$$\mathrm{I}_\beta=\int_e^R m(r-e)^2\,dr\,,\qquad \epsilon\approx\frac{3e}{2(1-e)} \tag{11}$$

First term of the flapping equation represents the rotational acceleration, second term stands for the centrifugal force, third term shows stiffness due to the hinge offset, fourth term comes from the spring stiffness at the flapping hinge and fifth term comes from the preconing of blades. The right hand side of the equation represents the the aerodynamic force. Dimensional (rad/s) and nondimensionalized natural frequencies with respect to the rotational speed of the flap equation are expressed by Equations (12) and (13), respectively.

$$\omega_{n_{f,d}}=\Omega\sqrt{1+\epsilon+\frac{k_\beta}{\Omega^2 \mathrm{I}_\beta}} \tag{12}$$

$$\omega_{n_{f,nd}} = \sqrt{1 + \epsilon + \frac{k_\beta}{\Omega^2 I_\beta}} \tag{13}$$

The aerodynamic moment is created by the lift force. The lift force is governed by the angle of attack and the sectional velocity. The angle of attack depends on the pitch angle input given by the pilot and the twist angle of the section. The right hand side of Equation (10) can be written in terms of the pitch angle defined in Equation (7) and the left hand side of Equation (10) can be written in terms of the flap angle defined in Equation (6). Also, the forcing due to the roll rate or the pitch rate of the fuselage can be added to the right hand side of Equation (10) as shown in section 1.3 of reference [44] for maneuvering flight conditions. On the other hand, the flapping equation and the pitch equation contain higher harmonic terms in reality. Furthermore, the coefficients of periodic terms are time dependent in the aspect of the flight mechanics. However, the coefficients of periodic terms are assumed to be constant and only the first harmonic terms are evaluated in the theoretical rotor dynamics analysis. The trim solution for a periodic response can be obtained from the harmonic balancing. The harmonic balancing is based on equating the coefficients of same periodic functions of both sides of the equation. Also, inflow is taken as uniform and constant throughout the rotor disc. Detailed information is given in sections 2.3.1 and 2.3.2.

2.1.3. Lag Dynamics

Top view of the blade is given in Figure 14 to show the forces and the moments acting in lag dynamics. In static equilibrium, lag equation is written from the moments acting on the lag hinge point. Force and moment directions are shown in Figure 14.

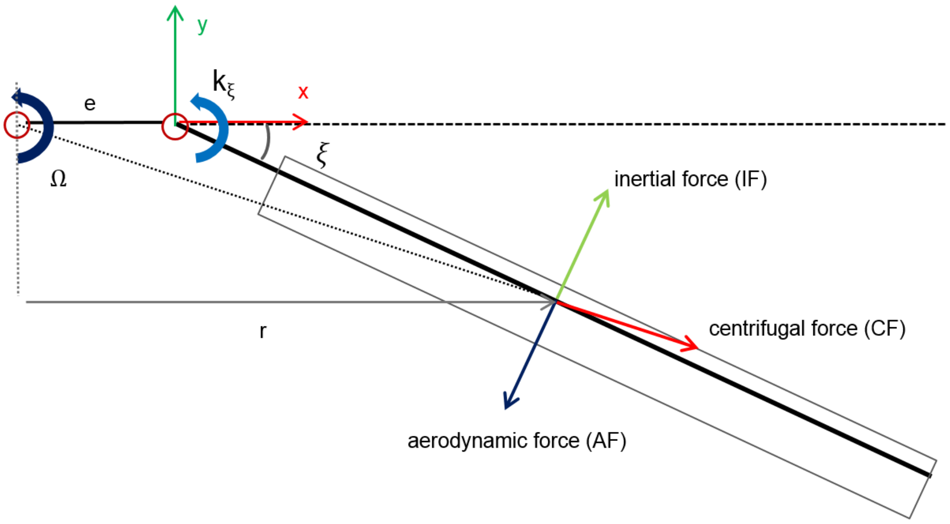

Figure 14 Forces and Moments Acting on the Blade in Lag Dynamics

A second order equation of motion can be written for the lag dynamics for a rigid blade. Acting loads in the lag dynamics are the inertial force, the centrifugal force, the drag force and the spring force in the lead-lag direction. The Coriolis force is neglected in the lag dynamics equations.

$$\begin{gathered}\left(\int_e^R m(r-e)^2\,dr\right)\ddot{\xi}+\left(\int_e^R m\Omega^2 r(r-e)\frac{e}{r}dr\right)\xi \\ -\int_e^R F_{aero}(r-e)\,dr+k_\xi\xi=0\end{gathered} \tag{14}$$

Lag equation can be reduced to Equation (15),

$$\ddot{\xi}+\Omega^2\left[\frac{e\,\mathrm{S}_\xi}{\mathrm{I}_\xi}+\frac{k_\xi}{\Omega^2\,\mathrm{I}_\xi}\right]\xi=\frac{M_{aero,lag}}{\mathrm{I}_\xi} \tag{15}$$

where the second mass moment of inertia and the first mass moment of inertia are defined as;

$$\mathrm{I}_\xi = \int_e^R m(r-e)^2\,dr\,, \qquad \mathrm{S}_\xi = \int_e^R m(r-e)\,dr \tag{16}$$

The natural frequency of the lag equation can be expressed in dimensional (rad/s) and nondimensionalized forms as in Equations (17) and (18) respectively.

$$\omega_{n_{f,d}} = \Omega\sqrt{\frac{e\,\mathrm{S}_\xi}{\mathrm{I}_\xi} + \frac{k_\xi}{\Omega^2\,\mathrm{I}_\xi}} \tag{17}$$

$$\omega_{n_{f,nd}} = \sqrt{\frac{e\,\mathrm{S}_\xi}{\mathrm{I}_\xi} + \frac{k_\xi}{\Omega^2\,\mathrm{I}_\xi}} \tag{18}$$

Rotational speed is defined according to the natural frequencies of the fuselage. Rotor speed can alter in maximum %10 range because of the fact that the rotational frequency may overlap with the natural frequencies of the helicopter. Therefore, the thrust is increased or decreased by only increasing and decreasing the pitch angles of the blades. The rotor blade sections are designed and arranged according to the mode shapes and the natural frequencies.

2.1.4. Torsion Dynamics

Sectional view of the blade is given in Figure 16 to show the forces and the moments acting in feathering dynamics. Top view of the blade is given in Figure 15 to show the eccentricity between the feathering axis and the cg axis. In static equilibrium, torsion equation is written around the feathering axis. Force and moment directions are shown in Figure 16.

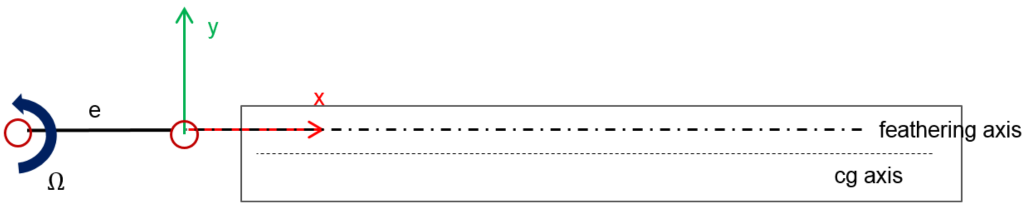

Figure 15 Top View of One Blade in Torsion Dynamics

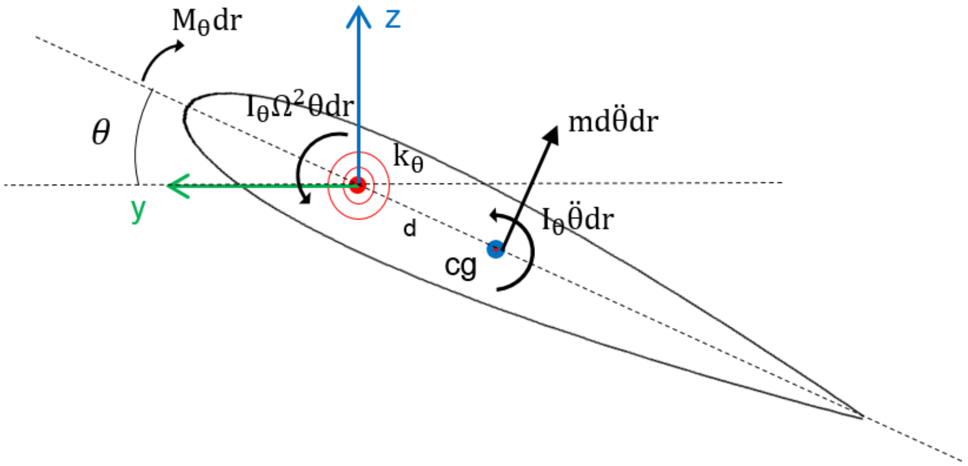

Figure 16 Forces and Moments Acting on the Blade in Torsion Dynamics

A second order equation of motion can be written for the torsion dynamics for a rigid blade. Acting loads in the torsion dynamics are the inertial force, the centrifugal force, the drag force and the spring force in the feathering direction.

$$\begin{aligned}\int_e^R \mathrm{I}_0\ddot{\theta}\, dr + \int_e^R md^2\ddot{\theta}\, dr + + \int_e^R \mathrm{I}_\theta\Omega^2\, \theta dr \\ + k_\theta(\theta - \theta_{control}) - \int_e^R M_\theta\, dr = 0\end{aligned} \tag{19}$$

where I_0 is the mass moment of inertia with respect to center of gravity of the section and I_θ is the mass moment of inertia with respect to the feathering axis of the section.

In Equation (19), the first term stands for the inertial torque defined around the sectional center of gravity. The second term stands for the moment of the inertia force due to rotation around the feathering axis. The third term represents the moment due to perpendicular component of the centrifugal force since it is applied at the center of gravity location of the section. The fourth term stands for the spring stiffness of the pitch degree of freedom. Last term represents the aerodynamic pitching moment applied around the feathering axis.

The torsion equation can be reduced to Equation (20),

$$\ddot{\theta} + \left(\Omega^2 + \frac{k_\theta}{\mathrm{I}_f}\right)\theta = \frac{M_{Aero}}{\mathrm{I}_f} + \frac{k_\theta}{\mathrm{I}_f}\theta_{control} \tag{20}$$

where the total mass moment of inertia around the feathering axis is defined as;

$$\mathrm{I}_f = \int_e^R \mathrm{I}_\theta \, dr = \int_e^R (I_0 + md^2)\, dr \tag{21}$$

The natural frequency of the torsion equation can be expressed in dimensional (rad/s) and nondimensionalized forms as in Equations (22) and (23).

$$\omega_{n_{f,d}} = \Omega\sqrt{1 + \frac{k_\theta}{\Omega^2\, \mathrm{I}_f}} \tag{22}$$

$$\omega_{n_{f,nd}} = \sqrt{1 + \frac{k_\theta}{\Omega^2\, \mathrm{I}_f}} \tag{23}$$

2.2. Multibody Dynamics

The comprehensive helicopter simulation blends the aerodynamic solution with the structural solution which requires the multibody model of the architecture. The multibody systems are constituted of rigid parts, joints, prescribed motions and dynamic elements such as springs, dampers, point masses and forces or flexible elements such as beams or cables, pulleys and gears. Recent formulation for the multibody dynamic problems is based on the Lagrangian dynamics. Simply, a numerical solution is obtained by solving a system set of nonlinear equations. In this section, a summary to the construction of the set of the equations of the multibody system is introduced and the solution methodology are given in references [45] and [46]. In multibody mechanical systems, system of nonlinear equations is constructed using generalized coordinates.

2.2.1. Formulation

The formulation starts with the definition of the generalized coordinates in forming the system of equation for the nonlinear multibody system. Positions, velocities and the accelerations of the bodies of the MBD system can be represented in the independent coordinates (maximal coordinates) or in the dependent coordinates. Independent coordinates are equal to the total number of degrees of freedom of the MBD system. On the other hand, the dependent coordinate systems have less number of coordinates than the total degree of freedom of the MBD system. The main point is that the dependent coordinate systems only cover the constraints between the bodies which reduce the total degree of freedom. For this reason, it is more appropriate to represent a MBD system in the dependent coordinates. On the other hand, the dependent coordinates can be defined relatively between the parts or absolutely with respect to a fixed frame. The relative coordinates determine the position of one part relative to the other part which are connected to each other via a joint. A drawback is stated in reference [45] that representing a MBD system in the relative coordinates leads to full matrices which takes more time in the computation. Therefore, the best way to write the equations of motion is to write them with respect to absolute coordinates which are called as the generalized coordinates. Generalized coordinates can be expressed in two dimensional space as shown in Equation (24) for one part.

$$q_i = \begin{bmatrix} R_{x_i} & R_{y_i} & \theta_i \end{bmatrix} \tag{24}$$

where R_{x_i}, R_{y_i} are the components of vector $\vec{R_i}$ in the x and y direction of and θ_i is the rotational degree of vector $\vec{R_i}$ for part i in 2D space. $\vec{R_i}$ is the vector between the cg of part i and the origin of the inertial frame which is seen in Figure 17.

For n number of parts, generalized coordinates are represented as in Equation (25).

$$q = [q_1 \quad q_2 \quad q_3 \quad \cdots \quad q_n] \tag{25}$$

In all joints, the constraints can be expressed with algebraic equations. For instance, a constraint which prevents the rotation between two links is expressed with a constant angle between angular degree of freedom of the two parts in two dimensional space. Fixed constraint is expressed algebraicly as given in Equation (26).

$$q_i - C = 0 \tag{26}$$

Revolute joints allow one degree of rotation while constraining the other five degrees of freedom. The equation for revolute joints is derived using the vector summation as seen in Figure 17.

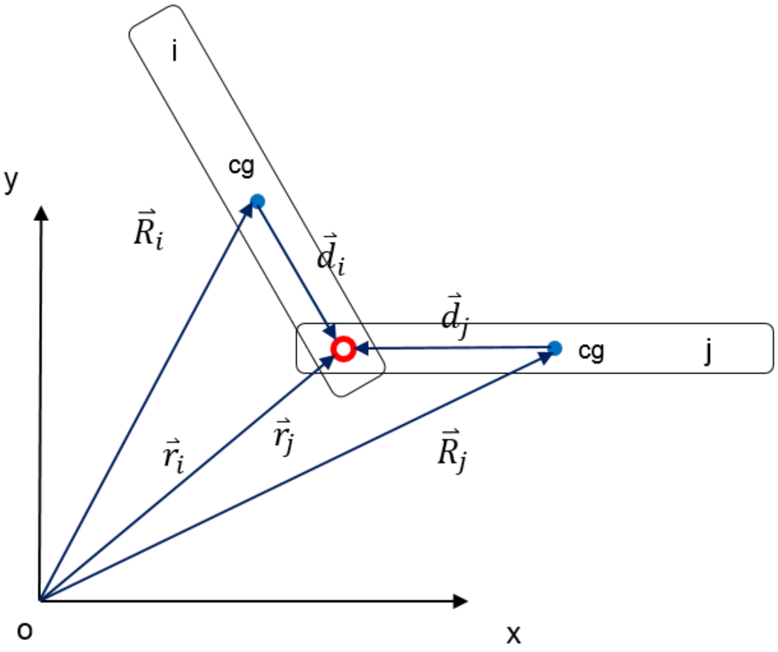

Figure 17 Constraint Equation Derivation for Revolute Joints in 2D Space [45]

Revolute joint constraint is prescribed in Equation (28) in two dimensional space which is taken from reference [45].

$$\vec{r}_i = \vec{r}_j \tag{27}$$

$$\vec{R}_i + A_i\vec{d}_i - \vec{R}_j - A_j\vec{d}_j = 0 \tag{28}$$

A matrix is the rotation matrix depending on θ_i or Euler angles as given in reference [45] for three dimensional space. A spherical joint has three rotational degree of freedom while it constraints three translational motion. A universal joint permits the rotation around two axes while it constraints other four degrees of freedom. A cylindrical joint has one rotational and one translational degrees of freedom while constraining the other four degrees of freedom. Constraints on rotational degree of freedom can be modeled similar to the revolute joint. Constraints on translational degree of freedom can be modeled similar to the prismatic joint.

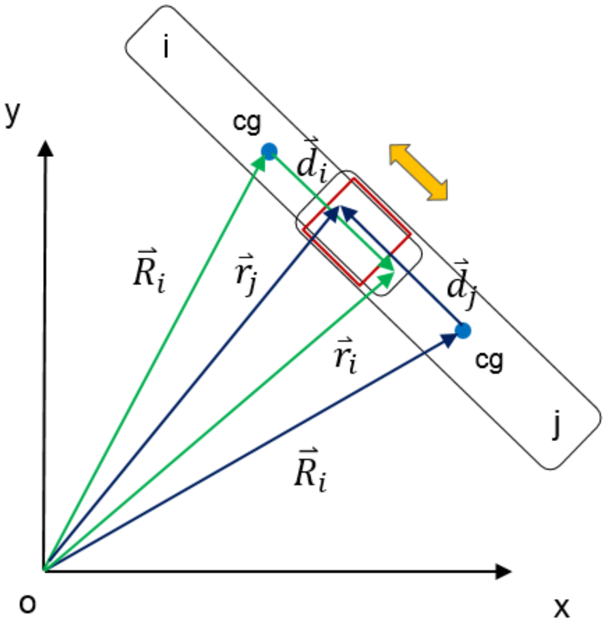

Figure 18 Constraint Equation Derivation for Prismatic Joints in 2D Space [45]

A prismatic joint can be modeled as in Figure 18. In the two dimensional space, it can be expressed with two equations given by Equations (29) and (31). A prismatic joint prevents the relative rotation between two parts which is prescribed in Equation (29).

$$\theta_i - \theta_j - C = 0 \tag{29}$$

A second equation can be written to satisfy the parallelism between $\vec{u}_i$ and $\vec{u}_j$, or the orthogonality between the joint axis and an outside vector on one body, initially perpendicular to the joint axis.

$$A_i \vec{d}_i \times \left(\vec{r}_i - \vec{r}_j\right) = 0 \tag{30}$$

$$A_i\vec{d}_i \times \left(\vec{R}_i + A_i\vec{d}_i - \vec{R}_j - A_j\vec{d}_j\right) = 0 \tag{31}$$

Next, the equations are written in terms of the time and the generalized coordinates as in Equation (32).

$$C(q,t) = [C_1(q,t) \quad C_2(q,t) \qquad \cdots \quad C_n(q,t)]^T = 0 \tag{32}$$

where $q(t)$ is given by expressions (24) and (25).

In Equation (32), $C(q,t)$ stands for the translational and rotational constraints. A constraint equation is formed between the two bodies and an algebraic set of equations is constructed and solved for the part positions. Velocities and accelerations are calculated by taking the time derivative of the equation set given in (32). Velocities are expressed in Equation (34) and accelerations are expressed in Equation (38). The kinematic solution is obtained from Equations (32) to (38). Using the chain rule, velocity is obtained by taking the time derivative of the position equation given in Equation (32).

$$\frac{dC(q,t)}{dt} = \frac{\partial C}{\partial q}\frac{\partial q}{\partial t} + \frac{\partial C}{\partial t} = 0 \tag{33}$$

$$C_q\dot{q} = -C_t \tag{34}$$

After taking second time derivative of the velocity from Equation (33), acceleration is obtained as shown in Equation (38). Intermediate steps are given in Equations (35), (36) and (37).

$$\frac{d^2C(q,t)}{dt^2} = \frac{\partial}{\partial t}\left[\frac{\partial C}{\partial q}\frac{\partial q}{\partial t} + \frac{\partial C}{\partial t}\right] \tag{35}$$

$$\begin{aligned}\frac{d^2C(q,t)}{dt^2} = \frac{\partial}{\partial q}\left[\frac{\partial C}{\partial q}\frac{\partial q}{\partial t}\right]\frac{\partial q}{\partial t} + \frac{\partial}{\partial t}\left[\frac{\partial C}{\partial q}\frac{\partial q}{\partial t}\right] + \frac{\partial}{\partial q}\left(\frac{\partial C}{\partial t}\right)\frac{\partial q}{\partial t} \\ + \frac{\partial}{\partial t}\left(\frac{\partial C}{\partial t}\right) = 0\end{aligned} \tag{36}$$

$$\frac{d^2C(q,t)}{dt^2} = \frac{\partial}{\partial q}\left[\frac{\partial C}{\partial q}\frac{\partial q}{\partial t}\right]\frac{\partial q}{\partial t} + 2\frac{\partial^2 C}{\partial q \partial t}\frac{\partial q}{\partial t} + \frac{\partial C}{\partial q}\frac{\partial^2 q}{\partial t^2} + \frac{\partial^2 C}{\partial t^2} = 0 \tag{37}$$

$$C_q\ddot{q} = -\left(C_q\dot{q}\right)_q\dot{q} - 2C_{qt}\dot{q} - C_{tt} \tag{38}$$

Secondly, the dynamic solution is based on the Newton's second law of motion. The force is expressed at the joints as the summation of the external force and the reaction force as given in Equation (39),

$$M\ddot{q} = Q_e + Q_c \tag{39}$$

where Q_e is the external force vector and Q_c is the reaction force vector at the joints. The reaction force is expressed as the multiplication of an unknown Lagrange coefficient in Equation (40) and the Jacobian matrix C_q^T which is constructed from the gradient of the constraint equations with respect to the generalized coordinates is given in Equation (41).

$$Q_c = -C_q^T\lambda \tag{40}$$

$$C_q^T = \begin{bmatrix} \frac{\partial C_1}{\partial q_1} & \frac{\partial C_1}{\partial q_2} & \cdots & \frac{\partial C_1}{\partial q_n} \\ \frac{\partial C_2}{\partial q_1} & \frac{\partial C_2}{\partial q_2} & \cdots & \frac{\partial C_2}{\partial q_n} \\ \vdots & \vdots & & \vdots \\ \frac{\partial C_n}{\partial q_1} & \frac{\partial C_n}{\partial q_2} & \cdots & \frac{\partial C_n}{\partial q_n} \end{bmatrix} \tag{41}$$

The reaction force term is taken to the left hand side of the dynamic equation and the set of equation system becomes as in Equation (43).

$$M\ddot{q} + C_q^T\lambda = Q_e \tag{42}$$

$$\begin{bmatrix} M & C_q^T \\ C_q & 0 \end{bmatrix}\begin{bmatrix} \ddot{q} \\ \lambda \end{bmatrix} = \begin{bmatrix} Q_e \\ -\left(C_q\dot{q}\right)_q\dot{q} - 2C_{qt}\dot{q} - C_{tt} \end{bmatrix} \tag{43}$$

This equation set contains both the algebraic and the differential equations. Unknowns are the accelerations and the Lagrange multipliers. This nonlinear set of equation can be solved with Newton and Newton like methods. After solving this set of equations the Lagrange multipliers and the accelerations are found. Then, the velocities and the positions of the generalized coordinates can be obtained by the time integration. This is the methodology in the formulation and in the solution in multibody dynamic programs such as MSC Adams [46].

In the MBD analysis, first a kinematic analysis is performed. In the kinematic analyses, the total degree of freedom of the system should be zero. In the dynamic analyses total degree of freedom of the system should be greater than zero. In the MBD systems, a degree of freedom can be constrained by two or more joints. These constraints cause redundancy in the system. Redundant constraints make structures hyperstatic, which causes erroneous load calculation. In the hyperstatic systems, the loads acting on the joints can be found from the superposition of the forces and the moments of the rigid MBD analysis and an elastic finite element analysis (FEA).

2.2.2. Dymore - Finite Element Based MBD Solver

DYMORE [47] is a FE based flexible multibody solver designed to work as a comprehensive analysis tool for the rotorcraft applications. It is developed by Olivier Bauchau at Georgia Instutite of Technology. The program is widely applicable to any physical problem because of the nonlinear multibody formulation in the finite element discretization. Other commercial softwares such as ADAMS can be used in the kinematic and the dynamic analyses of the helicopter rotor. ADAMS [46] uses finite element method to get a stress solution on flexible elements by modal reduction or expansion. In this approach, a modal analysis is performed and a modal neutral file is provided for each flexible part to the model. This file contains modal stiffness, damping and mass information and it is generated after a modal analysis is performed in NASTRAN or ABAQUS. Furthermore, in ADAMS, flexible elements can be modeled as beams. Dymore is better than ADAMS since Dymore utilizes nonlinear composite beam theory [48] developed by Hodges while ADAMS uses Timoshenko beam theory. On the other hand, specifically, DYMORE is used for the rotary systems as a comprehensive analysis tool. It has a library of multibody construction elements of joints, beam, rigid connection element, cable, gear, spring, damper as well as aerodynamic elements, control elements and hydraulic elements. Models are constructed based on geometrical elements such as points and curves. Connections on the kinematic chain are constructed as points. Coordinate systems are created according to directions and points called as frames. Topological entities are defined at each point and they are used to create hieararchical representations at connections between the structural elements. Nonlinear composite beam theory developed by Hodges [48] is used. Beam elements are formulated and coupled with the nonlinear multibody system by Bauchau [47].

The aerodynamic computation is based on the lifting line theory and the blade element method. Each lifting line has airstations at which the airloads are calculated. Each section gets the angle of attack and the Mach number information and based on this information solver makes interpolation from the two dimensional lookup tables to find the sectional lift, drag and the moment coefficients. Dymore has an inflow model based on Peters-He [2] formulation to correct the angle of attack. The angle of attack is dependent on the blade flapping rate, the inflow angle and the oncoming flow angle. The lifting lines are modeled as elastic beams to model the aeroelastic behavior.

Controllers are linear and they are applied in a quasi-steady manner. Solver tries to reach the controller targets by changing controller variables. Between them, a gradient (Jacobian) matrix is constructed by giving small perturbations to the variables and monitoring the change in the trim targets. The controller tries to catch the trim targets along the gradient vector.

Dymore uses time marching in finite element discretization for the trim analyses and the flight simulations. To obtain a steady state solution a certain time should be spent for the solution process. After the problem is assumed to reach to the steady state, the response is saved and it is used in the transient analysis. If the user desires an eigenvalue analysis in the static analysis or in the dynamic analysis, natural frequencies and the mode shapes are calculated. The solution takes approximately 4 or 5 Newton iterations to reach convergence with tolerance of 10^{-5} at each time step. After the convergence is achieved within a Newton iteration, the rotor moves to the next time step at which the rotor disk is rotated by the rotor speed multiplied with the time step. The time step parameters and the convergence parameters are entered in text files. Figure 19 shows the solution steps of a comprehensive analysis in Dymore.

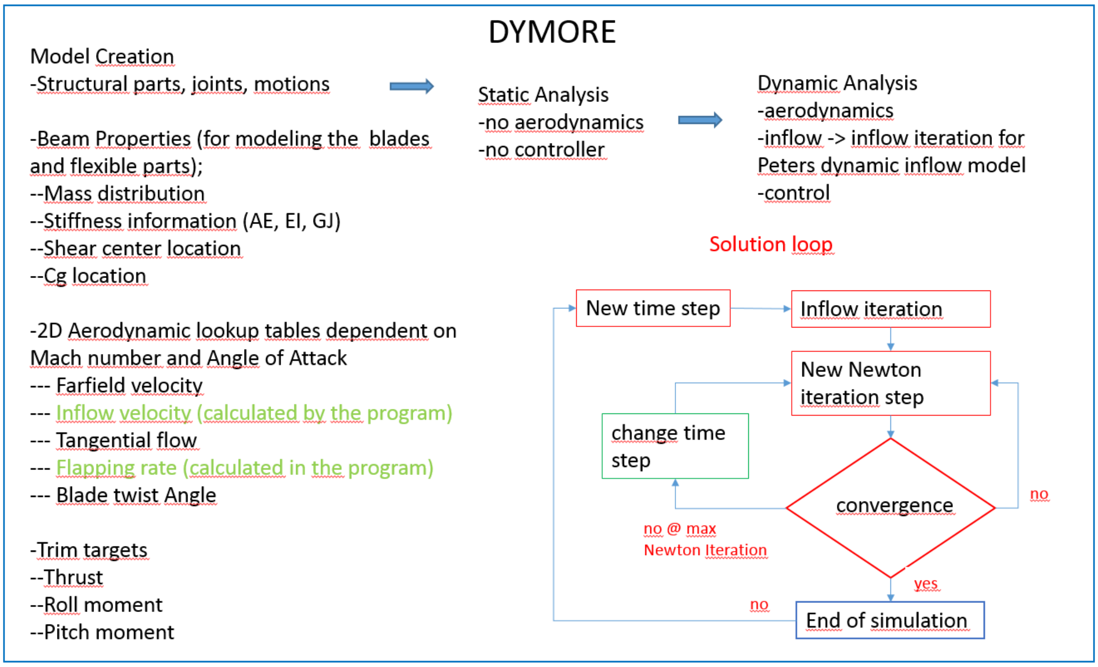

Figure 19 Solution Steps of the Multibody Dynamics Simulation in Dymore

2.2.3. Rotor Model

In this study, the main rotor architecture of UH60 utility helicopter is used which is given in Figure 20. UH60 main rotor is an articulated type rotor and the blades have flap, lag and torsional degrees of freedom. More joints increase the mechanical complexity. For this reason, rotors have a part called elastomeric bearing which collapses the three hinges into one virtual hinge providing three rotational degree of freedom at one point as shown in Figure 20.

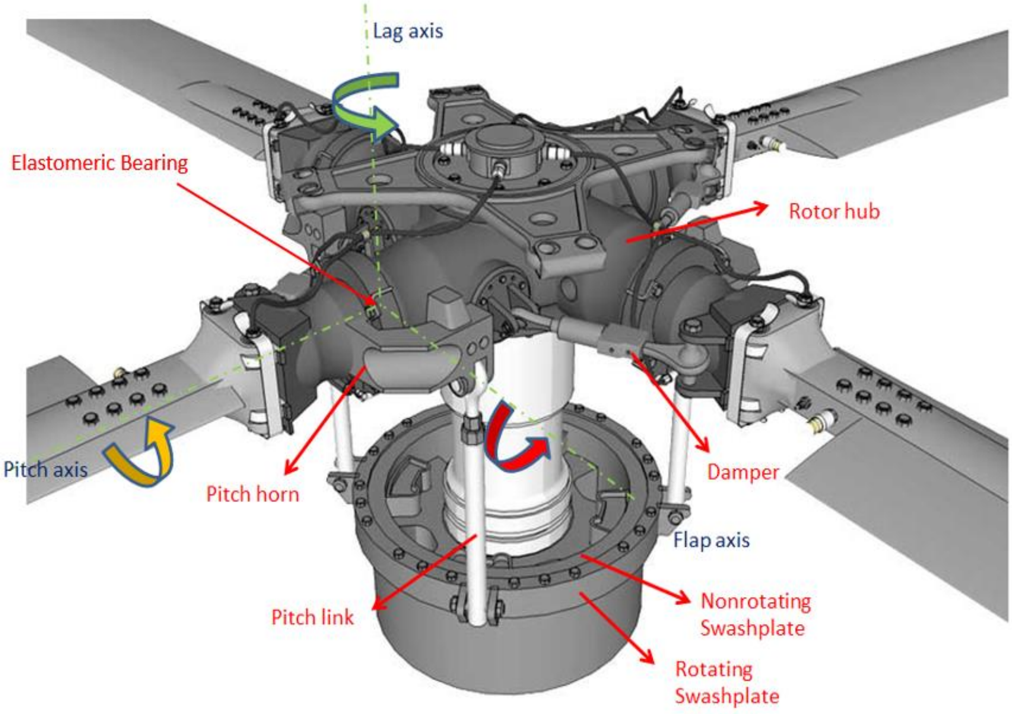

Figure 20 Simple CAD Model of UH60 Main Rotor [49]

The rotor parameters used in the dynamic model are summarized in Table 2.

Table 2 Main Rotor Parameters used in the Dynamic Model in Dymore

rotor radius	8.178 m
chord	0.527 m
number of blades	4
rotor speed	258 rpm/27.02 rad/s
virtual hinge location	0.381 m
blade twist	-12^{o}
airfoil profile	NACA0012

NACA 0012 airfoil profile is used along the blade span instead of UH60 main rotor blade profile SC1095 because of the availability of pitching moment coefficient table data for NACA 0012 in the initial steps of this study. The chord length is taken constant as 0.527 mm. Hinge offset is 0.381 m from the rotor shaft axis and can be interpreted from Figures 13 and 14. The blade is assumed to have no sweep angle at the tip. The blade is assumed to have a linear twist angle which is 10 degrees at the root and -2 degrees at the tip. Main reason for having a blade twist is to have equal load distribution on the blade. Parts related to the main rotor of UH-60 helicopter are illustrated in Figure 21.

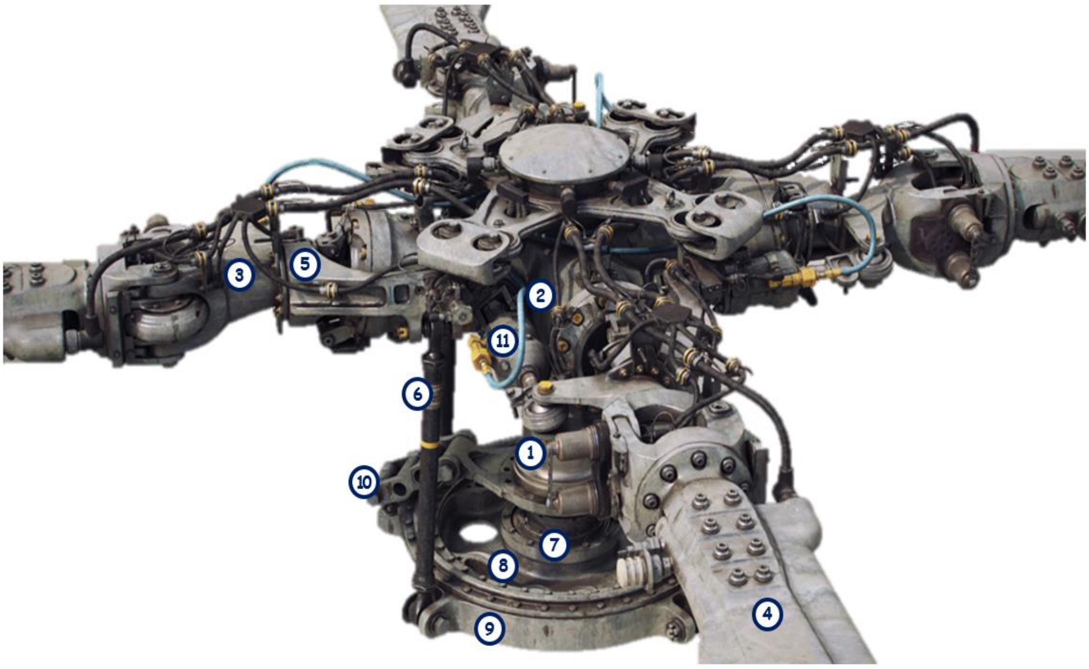

Figure 21 Parts of Main Rotor of UH-60 [50]

Part numbers and part names of the main rotor of UH-60 are given in Table 3.

Table 3 Parts in Dynamic Rotor Model

Part ID	Description
1	mast
2	rotor hub
3	retention link

Table 3 continued

4	blade
5	pitch horn
6	pitch link
7	uniball
8	nonrotating swashplate
9	rotating swashplate
10	rotating scissor
11	damper

The rotor hub is the central part which anchors the rotor blades by spherical elastomeric bearings. It transfers rotation from the transmission shaft to the rotor blades. There has to be a splined connection between the transmission shaft and the rotor hub. Transmission shafts are generally made of machined corrosive resistant steel. Rotor hubs are generally made of forging of titanium or steel. The pitch control lever works as a retention to the blade root and it transmits the control input from the pitch link to the rotor blade. Pitch control levers are generally made of aluminum machined parts.

Structurally, an elastomeric bearing is formed of laminated steel rings and special rubber assembled as one part. It is modeled in numerical computations as a spherical bearing having a stiffness and a damping around the rotational degrees of freedom. Elastomeric bearings cannot work under compressive loading; hence, they are placed in the rotor hub so that they are exposed to tensile loading only. Because of this reason, a tension link or a sleeve arm is used. The tension link is a part which connects the elastomeric bearing to the pitch horn. As the name implies, it operates under the effect of the centrifugal force. Therefore, it is a fatigue critical part. In sleeve type of rotors such as NH-90, the tension links and the pitch control levers are the same part.

There are control mechanisms to control blade pitch angles such as harmonic blade control or individual blade control (IBC). The individual blade control is carried out by separate actuators each installed on one blade. The harmonic control is carried out by a part called swashplate. The swashplate transfers the pilot input which comes from the rotor flight control system to the swashplate and to the blades. The tilt of the swashplate, tilts the thrust vector while the vertical displacement of the swashplate changes the magnitude of the thrust vector. The swashplate consists of two parts: the rotating swashplate and the nonrotating swashplate. There is a revolute connection which is a spherical ball bearing placed between the rotating and the nonrotating parts. The rotating swashplate receives the rotation from the mast by rotating scissors. The nonrotating swashplate receives input from the servo actuators as displacement strokes. The nonrotating swashplate transfers the pilot input to the rotating swashplate through the revolute bearing. There is a part called the uniball which is centered at the nonrotating swashplate acting as a spherical bearing. The uniball is guided by the mast and it moves vertically. It enables the tilt motion of the nonrotating swashplate.

Other parts that an articulated rotor have are the lag dampers, the rotating scissors and the nonrotating scissors. Since the articulated rotors are soft in plane; that is nondimensional lag frequency is less than 1, the ground resonance may occur. The lag dampers are employed to increase the lag frequency and to prevent the ground resonance. The rotating scissors are used to transfer the rotation from the mast to the rotating swashplate. The nonrotating scissors are used to prevent the undesired axial rotation on the nonrotating swashplate and the uniball which may occur due to the friction.

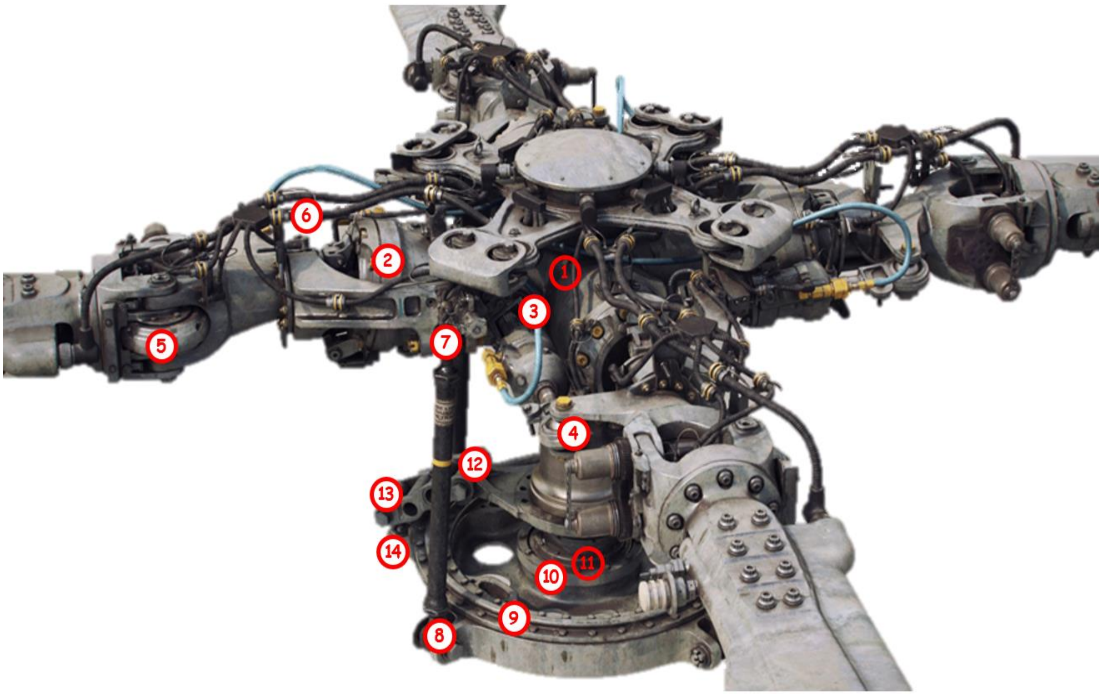

Figure 22 Joints of UH-60 Main Rotor Dynamic Model [50]

The joint types and the connected parts are given in Table 4 and the joint numbers are given in Figure 22.

Table 4 Joints in Dynamic Rotor Model

Joint ID	Connected Parts	Joint Type
1	mast - rotor hub	fixed
2	rotor hub - retention link	spherical
3	damper - rotor hub	spherical
4	damper - retention link	spherical
5	retention link - blade	fixed
6	pitch horn - tension link	fixed
7	pitch horn - pitch link	spherical
8	pitch link - rotating swashplate	spherical

Table 4 continued

9	rotating swashplate - nonrotating swashplate	revolute
10	nonrotating swashplate - uniball	universal
11	uniball-mast	prismatic
12	rotating scissor - mast	revolute
13	rotating scissor middle joint	revolute
14	rotating scissor - rotating swashplate	spherical

The dynamic model geometry of the isolated rotor is modeled using these parts prescribed above. First, connection points, reference frames and triads are defined in the dynamic model. A triad is a vector which only points a direction without application point. Then, at the points, the vertices are defined which are the computational nodes. These nodes are connected to each other with the edge elements. Joints, rigid connection elements and beam elements are attached on the edge elements.

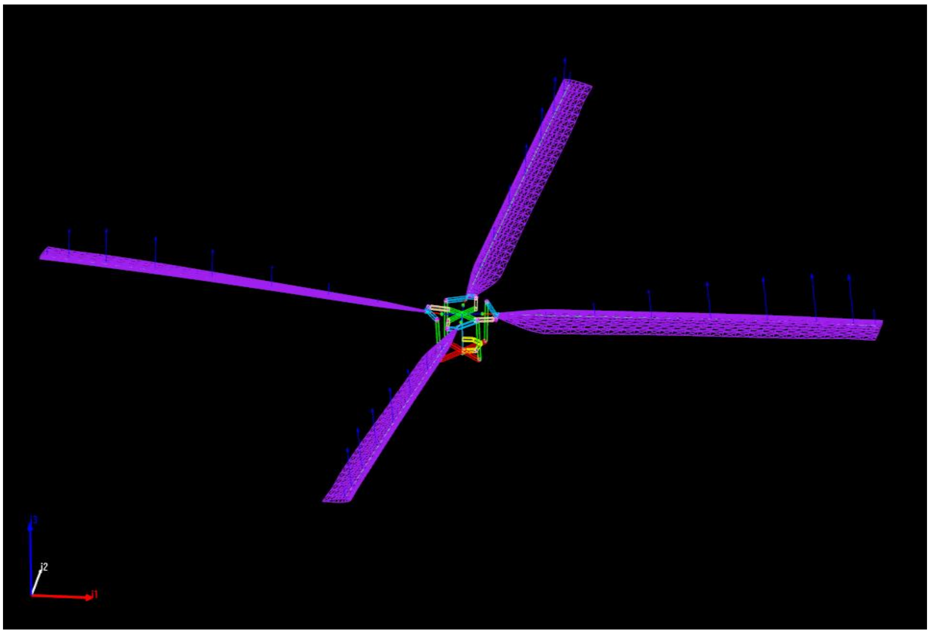

Figure 23 Four Blade Dynamic Model used in Trim Analysis

The four bladed model used in the trim analysis is given in Figure 23. All parts except the blades are modeled as massless. The chord length is taken as constant and it is given in Table 2. The one bladed model used in the simulation analyses is given in Figure 24.

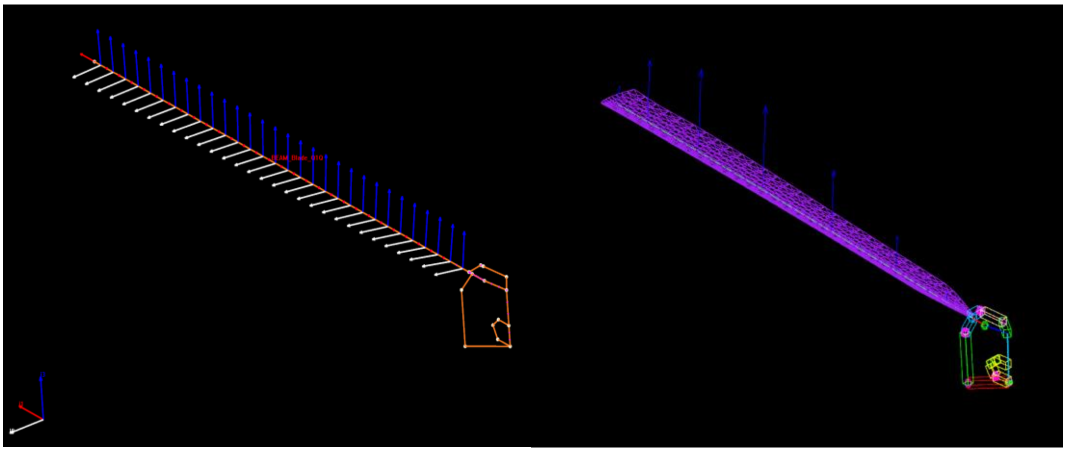

a) Blade twist distribution shown by coordinate systems at the blade structural stations
b) One blade model used in comparative simulation analysis

Figure 24 One Blade Dynamic Model used in Simulation Analysis after the Trim is achieved

The blade structural properties which are used in the dynamic model are given in Figure 25 as sectional properties such as blade twist distribution, mass distribution, axial stiffness (AE), shear stiffness, torsional stiffness (GJ) and flapwise bending stiffness (EI). Stiffness properties are calculated from the sectional analysis programs such as VABS (Variational Asymptotic Beam Section) or Section Builder.

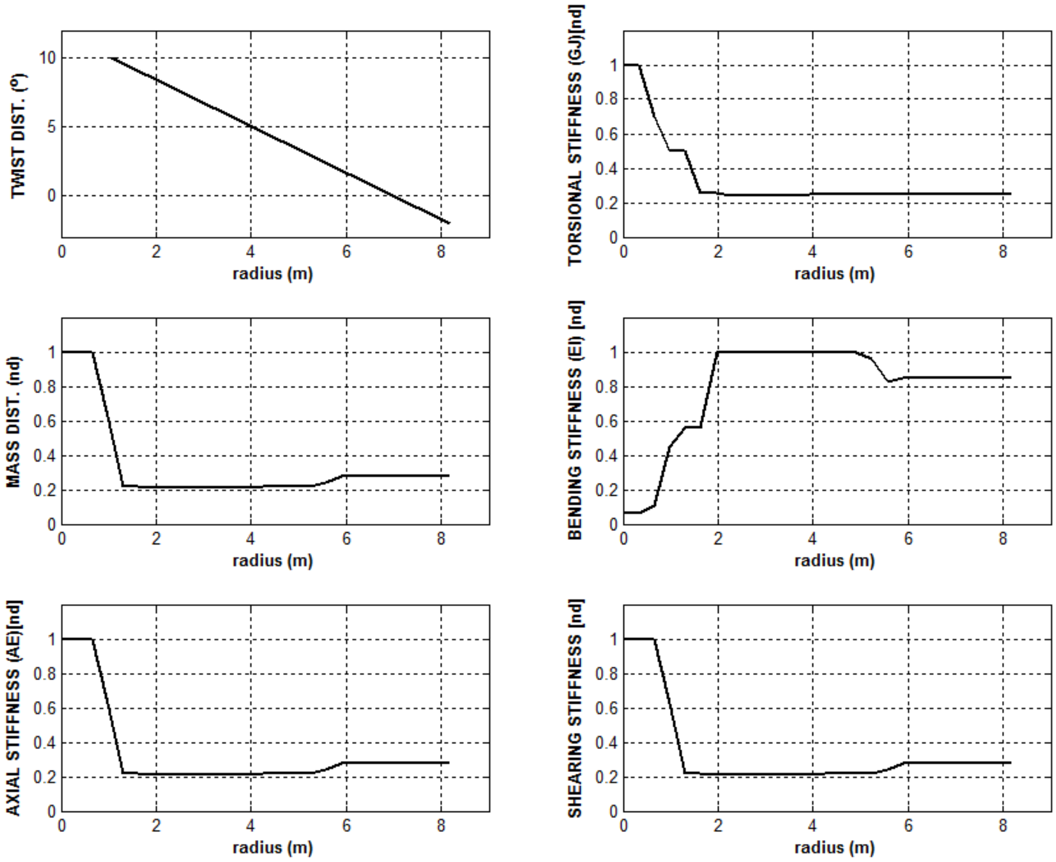

Figure 25 Structural Blade Properties entered in Dymore

Other blade properties such as the center of gravity offset and the shear center offset are kept as zero. The blade root corresponds to aproximately 0.7 m. The twist angle is 10° at the root and -2° at the tip of the blade and it varies linearly along the blade span. The axial stiffness, shearing stiffness and the mass of the sections are higher at the tip of the blade than the middle and the root section of the blade. Higher mass at the tip increases the natural frequencies at the nodes close to the tip. Similarly, increase in the axial stiffness at the blade tip is needed to balance the modal effect along the blade since there is a crossectional reduction at the blade tip. The flapwise bending stiffness is higher at the middle and the root sections since the flapwise bending moment is higher at the root when the loading is integrated from the tip to the root.

2.3. A Review on Rotor Aerodynamics

Theoretical investigation into the rotor aerodynamics starts with the momentum theory and the blade element theory. Firstly, induced flow is calculated by relying on the pressure difference across the rotor disk using the conservation of momentum and Bernoulli equations with an incompressible flow assumption. This is known as the momentum theory developed by Glauert [51]. This theory is coupled with the blade element theory for rotor applications and the resulting theory is named as the blade element momentum theory (BEM).

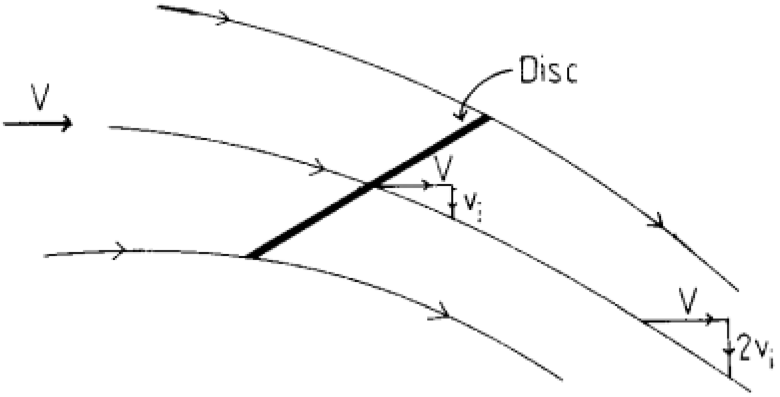

Figure 26 Interpretetation of Glauert Theory in Forward Flight [51]

Glauert proposes that the rotor disk acts like a wing in forward flight as shown in Figure 26. It reduces the need for the thrust in the forward flight which is an effect of the induced flow which is exerted on the rotor disk [51].

2.3.1. Inflow Theories

In simple theoretical calculations, the inflow is taken as constant and uniform throughout the rotor disk and it can be calculated iteratively from the Equation (44).

$$\lambda = \mu \tan \alpha_s + \frac{C_T}{2\sqrt{\mu^2 + \lambda^2}} \tag{44}$$

where the thrust coefficient (C_T) and the advance ratio (μ) are given in Equation (45), while λ is the inflow factor and α_s is the tilt angle of the tip path plane. In hover, the advance ratio is zero and the thrust is equal to the aircraft weight.

$$C_T = \frac{T}{\rho A(\Omega R)^2}, \qquad \mu = \frac{V\cos\alpha_s}{\Omega R} \approx \frac{V}{\Omega R} \tag{45}$$

where ρ is the density, A is rotor disk area, Ω is rotor speed, R is rotor radius and V is the farfield velocity. Velocity components acting on the rotor disc can be seen in Figure 27.

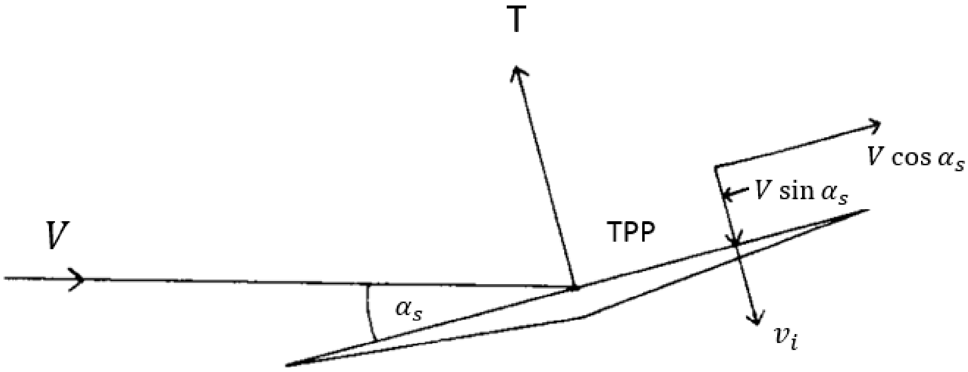

Figure 27 Tip Path Plane Incidence and Velocities on Rotor Disk in Forward Flight [51]

The first term in Equation (44) represents the inflow created by the forward velocity while the second term shows the inflow created by the rotation. The initial value for the inflow factor (λ_0) is calculated as shown in (46) and entered to the right hand side of Equation (44).

$$\lambda_0 = \frac{v_i}{\Omega R} \tag{46}$$

where v_i is the inflow velocity and λ_0 is initial inflow factor.

Inflow factor (λ) calculated from Equation (44) is reentered into the right hand side of the Equation (44) until the convergence is reached. This equation is valid for a constant and uniform inflow. It also proposes that the wake geometry is rigid based on the momentum theory.

Other theories related to the calculation of the inflow are the vortex wake methods (refer to section 4.2 of [42]) for which the rotor wake can be rigid, prescribed or deformable. The rigid wake models can be formulatized by an harmonic equation, the coefficients of which are determined by experimentally or numerically. Coleman (1945)[52] numerically modeled the wake as discrete circular rings and integrated these rings using the Biot-Savart Law when calculating the induced velocities along the blade span. Castles et de Leeuw (1954)[53] also modeled the wake as discrete circular rings. However, they integrated rings analytically and calculated the induced velocities from the Biot-Savart Law. Heyson et al (1957)[54] proposed to include other trailing vortices by not considering the tip vortices only as in Coleman's or Castles' work. Heyson et al. also specified that the filament strengths change linearly with the rotor radius. Drees (1949) model assumes that the trailing vortex filament strengths are constant in the radial direction and variable in the azimuthal direction.

Another model for the inflow calculation is derived by Mangler and Squire (1950) [55]. Mangler et al. derived an inflow model based on the linearized Euler equations for the incompressible flow. This inflow theory predicts the pressure distribution across the rotor disk by considering the inflow as a combination of the elliptical pressure distribution and a pressure distribution vanishing at the edge of the rotor disk. Leishman [56] summarized and tabulated the inflow theories related to vortex wake in section 3.5.2 of his book. Inflow factor can be expressed as given in the harmonic Equation (47),

$$\lambda = \lambda_{Glauert}\left(1 + \kappa_x r \cos\psi + \kappa_y r \sin\psi\right) \tag{47}$$

where harmonic coefficients κ_x and κ_y in Equation (47) are given according to related theories in Table 5 based on table 3.1 of reference [56]. r is radial distance, ψ is azimuth and $\lambda_{Glauert}$ is the inflow factor calculated from Equation (44).

Table 5 Vortex Wake Inflow Models [56]

Model	$\boldsymbol{\kappa_x}$	$\boldsymbol{\kappa_y}$
Coleman et al (1945)	$\tan(\chi/2)$	0
Drees (1949)	$(4/3)(1-\cos\chi-1.8\mu^2)\,/\sin\chi$	-2μ
Payne (1959)	$(4/3)[\mu/\lambda/(1.2+\mu/\lambda)]$	0
White & Blake (1979)	$\sqrt{2}\sin\chi$	0
Pitt & Peters (1981)	$(15\pi/23)\tan(\chi/2)$	0
Howlett (1981)	$\sin^2\chi$	0

In Table 5, the wake angle χ is the angle between the rotor axis and the wake central axis which is given by Equation (48).

$$\chi = \tan^{-1}\left(\frac{\mu}{\lambda}\right) \tag{48}$$

An example to the prescribed wake can be given in the model of Egolf and Landgrebe [57]. In the prescribed wake models, the vortex trajectory coordinates are prescribed by the experimental data. Scully [30] modeled the wake deformable under the influence of the wake elements leading to the free wake. Detailed information on the wake theories can be found in the survey of the inflow theories conducted by Chen [58], in the section 3.5.2 of reference [56] and in the section 4.2 of reference [42].

In general, the method used for the calculation of the inflow in the comprehensive rotor calculations is the dynamic inflow theory of Peters and He [2] (1995) which is derived based on the acceleration potential theory. The reason why this theory is used commonly is that the model is less expensive with sufficient accuracy. According to Peters, this theory is an intermediate level wake model between the simple momentum theory and the complicated freewake models. From the conservation of the mass and the conservation of the momentum, perturbation velocity potentials are related to the pressure field which is separated in forms of the convective pressure and the advective pressure. The acceleration potential is obtained by taking the spatial derivative of the momentum equation which leads to a Laplace equation for the convective and the unsteady part of the equation. Then, the acceleration potential is defined as the multiplication of two Legendre polynomials and a harmonic function after the separation of variables is applied to the Laplace equation written in the elliptical coordinates. All functions are in second order and dependent on the coordinate system variables (υ, η, ψ) with two constants namely the harmonic number and the radial mode number. The pressure at the edge of the rotor disk should be zero and the pressure at the infinity should be zero. According to these conditions, the acceleration potential is prescribed with Legendre functions which satisfy boundary conditions. Then, the acceleration potential is integrated for the induced flow and it is related to the pressure. The pressure distribution is obtained from the other aerodynamic models such as lifting line theory. Then, this system of equation is solved iteratively and the inflow distribution is obtained when the forcing of the equation set is the pressure distribution.

Main problems related to aerodynamics are the blade vortex interaction in the advancing side of the rotor disk and the reverse flow in the retreating side in the forward flight, the dynamic stall due to the reverse flow and transonic shocks at the blade tips. The disadvantage of the dynamic inflow theory, uniform inflow or prescribed inflow over the full CFD solutions or freewake solutions is that these theories do not include the blade tip vortices and do not predict the blade vortex interaction. Prandtl tip loss factor is used to include the tip effects in the lift distribution on the blade in these theories.

2.3.2. Blade Element Theory

Main theory used in the comprehensive analysis is the lifting line theory coupled with the blade element method. Different from Prandtl’s lifting line theory [59], the blade element theory is used in the analytical calculations and the numerical calculations to predict the airloads acting on the aerodynamic centers of the blades. The airloads are calculated based on the tabulated aerodynamic coefficients. Other powerful theories which can be used instead of the lifting line theory are the lifting surface theory and the vortex lattice method, which use Biot-Savart law in the calculation of the induced flow. The lifting line theory is a two dimensional theory while the lifting surface theory and the vortex lattice method are three dimensional theories. In the comprehensive analysis, the lifting surface theory and the vortex lattice method are generally used for the calculation of the induced flow while for the airload calculation, the tabulated coefficients are used. The induced flow is used to calculate the effective angle of attack and the aerodynamic coefficients are interpolated using the 2D performance tables. In-plane velocity distribution is given in Figure 28 and sectional velocity distribution is given in Figure 29.

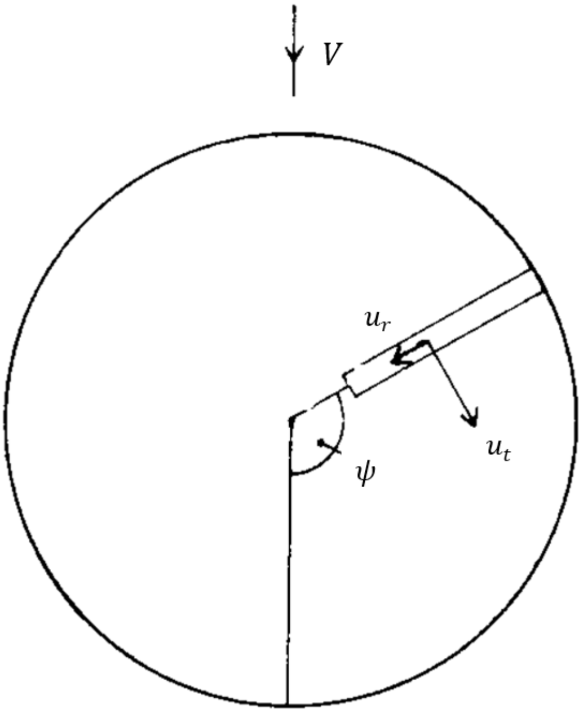

Figure 28 Top View of the Rotor Disc and Velocity Components in Forward Flight [51]

The aerodynamic loads acting on the blade section in the blade element theory are also shown in Figure 29.

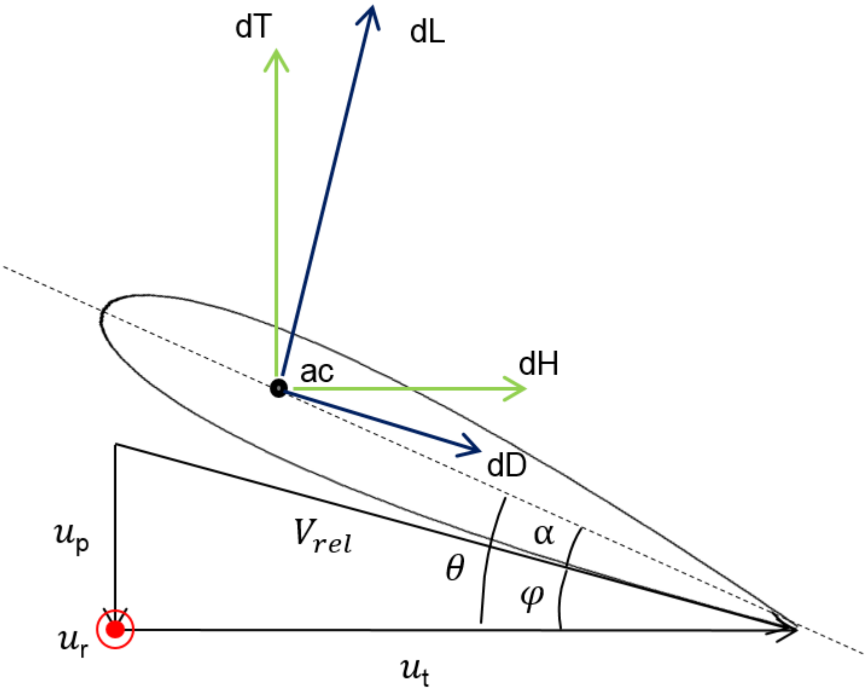

Figure 29 Blade Element Theory Applied in Forward Flight

$$u_t = \Omega(e + r) + \mu\Omega R \sin\psi \tag{49}$$

$$u_p = \lambda\Omega R \sin\beta + r\dot{\beta} + \beta\mu \sin\psi \cos\beta \tag{50}$$

$$u_r = \mu\Omega R \cos\psi \tag{51}$$

where u_t is tangential component, u_p is vertical component and u_r is radial component of the velocity acting on the blade in forward flight. Top view of the rotor disc is given in Figure 28 to show the tangential (u_t) and radial (u_r) velocity components. In Figure 29, tangential (u_t) and vertical (u_p) velocity components are shown.

In Equation (49), the first term and the second term are the tangential velocity oncoming to the blade section due to the rotational velocity and due to the forward flight speed. In the vertical velocity expression given by Equation (50), the first term stands for the axial inflow, the second term represents the flapping rate and the third term represents the contribution due to the forward velocity of the fuselage. The radial velocity only stems from the forward velocity of the fuselage as shown in Equation (51) and it is used to calculate the side forces in the hub frame. From the blade element theory, the sectional thrust and the drag force can be expressed in the hub plane by Equations (52) and (53),

$$dT = dL \cos \varphi - dD \sin \varphi \tag{52}$$

$$dH = dL \sin \varphi + dD \cos \varphi \tag{53}$$

where φ is the inflow angle. Using the small angle assumption, the drag term can be neglected in the sectional thrust coefficient calculation. After simplifications, the sectional thrust and the sectional side force equations can be written as,

$$dT \approx dL \tag{54}$$

$$dH \approx dL \sin \varphi + dD \tag{55}$$

Discrete sectional lift, drag and the sectional pitching moment can be written as,

$$dL = \frac{1}{2} \rho V_{\mathrm{rel}}^2 C_l ds \tag{56}$$

$$dD = \frac{1}{2} \rho V_{\mathrm{rel}}^2 C_d ds \tag{57}$$

$$dM = \frac{1}{2} \rho V_{\mathrm{rel}}^2 C_m c ds \tag{58}$$

where ds is the length of the discrete blade section along the blade span and V_{rel} is the relative velocity which is expressed in Equation (59).

In the lifting line method used in the comprehensive analysis tools, the numerical calculations of the sectional lift, drag and moment coefficients are interpolated from the two dimensional performance tables and they are used to calculate the sectional lift, drag and moment from these equations. These equations are dependent on the velocity and the angle of attack. Flow is assumed to be compressible given that the blade tip Mach number is less than the transonic Mach number limit of 0.8.

$$V_{rel} = \sqrt{{u_t}^2 + {u_p}^2} \tag{59}$$

The angle of attack is calculated in Equation (60) using Figure 29.

$$\alpha = \theta - \varphi \tag{60}$$

The inflow angle can be approximated as shown in Equation (61).

$$\varphi \approx \tan\varphi = \frac{u_p}{u_t} \tag{61}$$

After substituting α into the differential lift equation given by Equation (56), differential lift is expressed as in Equation (62).

$$dL = \frac{1}{2}\rho {V_{rel}}^2 c C_{l_\alpha}\left(\theta - \frac{u_p}{u_t}\right) dr \tag{62}$$

The moment created around the flapping hinge is given by Equation (63) which is obtained by integrating the moment of the differential lift along the blade span in the dynamic flap equation.

$$\begin{aligned} \mathrm{M}_{\text{aero,flap}} &= \int_e^R (r-e) dL \\ &= \frac{1}{2}\int_e^R \rho {V_{rel}}^2 c C_{l_\alpha}\left(\theta - \frac{u_p}{u_t}\right)(r-e) dr \end{aligned} \tag{63}$$

The aerodynamic lag moment around the lag hinge is given by Equation (65). Similar to the aerodynamic flapping moment, aerodynamic lag moment is obtained by integrating the moment of the differential horizontal force along the blade span.

$$\mathrm{M}_{\text{aero,lag}} = \int_e^R (r-e) dH \tag{64}$$

$$\mathrm{M}_{\text{aero,lag}} = \frac{1}{2}\int_e^R \rho {V_{rel}}^2 c \left[C_{l_\alpha}\left(\theta - \frac{u_p}{u_t}\right)\sin\varphi + C_d\right](r - e) dr \tag{65}$$

In unsteady aerodynamic calculations of the comprehensive analysis tools, the aerodynamic coefficients are updated with the unsteady models. Main assumptions are quasi-steadiness and the potential flow. The unsteady aerodynamic theories are mainly based on the thin airfoil theory. The thin airfoil theory proposes that an airfoil can be depicted as a vortex sheet prescribed along the chord line to produce the camber effect. From the fact that there should be no penetrating flow crossing the camber line, the net perpendicular velocity should be zero between the oncoming velocity and the induced effect of the vortices places on the camber line [59].

Theodorsen [43] investigated the unsteady aerodynamic behavior for a two dimensional airfoil in the frequency domain as Peters et al investigated the unsteadiness of the flow in time domain for a two dimensional airfoil [60] and for a three dimensional rotor disk [2]. According to the Leishman-Beddoes dynamic stall theory, the physical flow is examined in three phases namely unsteady attached flow, unsteady separated flow and unsteady dynamic stall vortex. Leishman-Beddoes model is a semi-empirical model. In the first phase of Leishman-Beddoes model, a set of first order ordinary differential equations are solved. The inputs are the angle of attack and the pitch rate while the outputs are the normal force coefficient and the pitching moment coefficient for this system. This is the phase where the unsteady attached flow is observed. The coefficient matrices for this set of ODE are given in detail in reference [61]. In the second phase, the separated flow is observed. Separation point at the trailing edge is determined based on the static data. The normal force coefficient and the moment coefficient are separated into a circulatory part which is due to the shed wake and a noncirculatory part. The dynamic stall formulation is also empirical. Leishman-Beddoes formulation and the empirical coefficients used in the formulation are given in references [3],[61]. On the other hand, in the ONERA dynamic stall model [5], a second order linear differential equation is solved. The circulation is the state variable and it is dependent on the difference between a linear static value extrapolated from the aerodynamic coefficients at low angle of attacks and the actual value. The parameters used in the ONERA theory is dependent on the airfoil shape and the Mach number [61].

Dymore uses the two dimensional Peters theory [62] for the unsteady attached flow and the Onera dynamic stall theory for the separated flow or Leishman-Beddoes theory for the attached flow and the separated flow. In this section information about unsteady aerodynamic analysis methods are provided in order to give background information about the unsteady theories and to show the modeling capability of the program. In this thesis study, the unsteady aerodynamic effects are neglected.

2.4. CFD Solvers and Used Parameters

In this section, formulations of XFOIL and SU2 and related turbulence models of SA and SST are briefly summarized. Parameters used in the analyses and computational domain used in the Navier-Stokes analyses are also provided. Formulations are taken from related publications given in subsections. Computational domain is generated in Pointwise software using a recorded macro. This macro is modified with desired parameters from another source code after it is created.

2.4.1. XFOIL – Panel Based Flow Solver

XFOIL [63] is a panel based airfoil design and analysis tool developed by Mark Drela at MIT. Using the panel method, it solves a linear set of equations for the inviscid flow. Then, it solves additional algebraic equations based on the integral momentum equation for the surface transpiration model which generates the boundary layer effect. XFOIL is developed for low Reynolds number flows for which the Reynolds number is less than 0.5 million. Karman-Tsien compressibility correction factor is used in XFOIL which is dependent on the Mach number. The panel method formulation is summarized by considering the XFOIL formulation in reference [63]. The inviscid formulation starts with writing a stream function in terms of the vortex strengths and the source strengths of the panels. In this formulation, the domain is discretized with N panels around the airfoil and the wake is discretized with N_w panels.

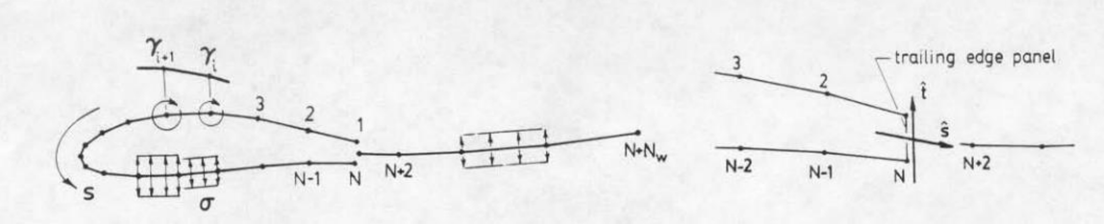

Figure 30 Source and Vortex Distribution on Panel Discretization in XFOIL formulation [63]

Nth panel is the trailing edge panel for a blunt edge airfoil. In the formulation, it is stated that each panel (wake and airfoil) have a constant source strength σ_i and each panel has a linear vortex strength defined in the nodes γ_i and γ_{i+1} as seen in Figure 30. The stream function is given by Equation (66).

$$\psi(x,y) = u_\infty y - v_\infty x + \frac{1}{2\pi}\int \gamma(s)\ln r(s)\,ds + \frac{1}{2\pi}\int \sigma(s)\,\theta(s)\,ds \tag{66}$$

S is the airfoil surface coordinate in the counter clockwise direction starting from the trailing edge. In Equation (66), the first two terms are the contribution of the farfield velocity while the last two terms are the contribution of the vortex and the source strengths of the panels in the flow field streamfunction. There are N panels for which the zero flow penetration condition given by Equation (67) can be written. This can be expressed mathematically including the induced effects of the other panels. This is the procedure in the panel methods written in terms of the potential function. In this case, unknowns are the source and the vortex strengths and the total number of unknowns are N+1 for the inviscid solution.

$$\nabla\phi \cdot \vec{n} = 0 \tag{67}$$

In XFOIL, the formulation is based on the stream function which has the same value on the airfoil surface. This condition is used instead of the no penetration condition given in Equation (67). The stream function is written for N panels as shown in Equation (68). In Equation (68), ψ_0 is the stream function value on the airfoil surface and a_{ij} and b_{ij} are the influence coefficients.

$$\sum_{j=1}^{N} a_{ij}\gamma_j - \psi_0 = -u_\infty y + v_\infty x - \sum_{j=1}^{N+N_w-1} b_{ij}\sigma_i \tag{68}$$

The influence coefficients (a_{ij}, b_{ij}) are the factors of the effects of other panel strengths ($i = 1 \ldots N$) on the panel strength of j for vortex strengths and source strengths respectively. a_{ij} and b_{ij} are calculated from the integrals given in Equation (66).

Source strengths (σ_i) of the panels are set to zero for the inviscid solution. The unknowns are stream function value (ψ_0) on the airfoil surface and vortex strengths

(γ_j) of the panels. In Equation (68), N equations can be written for N number of nodes and there are N+1 unknowns. Therefore, it is needed to have an extra equation to obtain the inviscid solution.

The extra equation comes from the Kutta condition which states that the flow leaves the trailing edge with the same velocity from the upper and the lower surfaces. This condition is given in Equation (69).

$$\gamma_1 + \gamma_N = 0 \tag{69}$$

A linear set of equation is created from Equations (68) and (69). It is stated that the inviscid solution can be obtained by setting the source strengths "σ_i" zero in the equation set. The unknowns are the stream function value on the airfoil surface ψ_0 and the panel vortex strength values. The system has N+1 equations and N+1 unknowns. Direct methods such as Gauss Elimination can be used to obtain the inviscid solution. The source terms are later used for the inviscid viscous coupling in the surface transpiration model.

In XFOIL, the boundary layer formulation [63][64] starts with the integral momentum (θ) equation, Equation (70) and the kinetic energy thickness (θ^*) equation, Equation (71) and the kinetic energy shape parameter (H^*) equation which is given by Equation (72)

$$\frac{d\theta}{ds} + (2 + H - M_e^2)\frac{\theta}{u_e}\frac{du_e}{ds} = \frac{C_f}{2} \tag{70}$$

$$\frac{d\theta^*}{ds} + \left(\frac{\delta^{**}}{\theta^*} + 3 - M_e^2\right)\frac{\theta^*}{u_e}\frac{du_e}{ds} = 2C_d \tag{71}$$

The kinetic energy shape parameter (H^*) equation (Equation (72)) is obtained from Equations (70) and (71).

$$\theta\frac{dH^*}{ds} + \left(2H^{**} + H^*(1 - H)\right)\frac{\theta}{u_e}\frac{du_e}{ds} = 2C_d - H^*\frac{C_f}{2} \tag{72}$$

where s is the streamwise coordinate, u_e is the edge velocity and M_e is the edge Mach number of the boundary layer velocity profile. H is the shape parameter, H^* is the kinetic energy shape parameter and H^{**} is the density thickness shape parameter which are given by Equation (73). δ^{**} is the density thickness, θ is the momentum thickness and θ^* is the kinetic energy thickness which are given by Equations (75), (76) and (77) respectively. C_f is the skin friction coefficient and C_D is the drag coefficient which are expressed in Equations 11 and 12 for laminar regions and Equations 14 and 20 for turbulent regions in [64].

$$H = \frac{\delta^*}{\theta}, \;\; H^* = \frac{\theta^*}{\theta}, \;\; H^{**} = \frac{\delta^{**}}{\theta} \tag{73}$$

Displacement thickness (δ^*) is given as,

$$\delta^* = \int_0^{n_e} \left(1 - \frac{\rho u}{\rho_e u_e}\right) dn \tag{74}$$

Density thickness (δ^{**}) is given as,

$$\delta^{**} = \int_0^{n_e} \frac{u}{u_e}\left(1 - \frac{\rho}{\rho_e}\right) dn \tag{75}$$

Momentum thickness (θ) is given as,

$$\theta = \int_0^{n_e} \frac{\rho u}{\rho_e u_e}\left(1 - \frac{u}{u_e}\right) dn \tag{76}$$

Kinetic energy thickness (θ^*) is given as,

$$\theta^* = \int_0^{n_e} \frac{\rho u}{\rho_e u_e}\left(1 - \left(\frac{u}{u_e}\right)^2\right) dn, \tag{77}$$

where ρ_e is the density at the edge of the boundary layer and ρ is the density inside the boundary layer.

In the laminar formulation, the kinetic energy shape parameter (H) is based on the Falkner-Skan profile and it is dependent on the kinematic shape parameter $H_k$when the density across the boundary layer is constant. This parameter is derived by

Whitfield [65] and it is given in reference [64]. The density flux shape parameter H^{**} is also derived for the laminar and the turbulent flow using H_k.

In addition to Equations (70) and (72), the maximum shear stress (C_τ) in Equation (78) is taken from the XFOIL formulation paper [63]. This equation is shear stress coefficient equation which is used in the calculation of drag coefficient (C_d) in turbulent regions (see Equation 20 in reference [64]).

$$\begin{aligned}\frac{\delta}{C_\tau}\frac{dC_\tau}{d\xi} &= 5.6\left(C_{\tau,EQ}^{0.5} - C_\tau^{0.5}\right) \\ &\quad + 2\delta\left\{\frac{4}{3\delta^*}\left[\frac{C_f}{2} - \left(\frac{H_k - 1}{6.7H_k}\right)^2\right] - \frac{1}{u_e}\frac{du_e}{d\xi}\right\}\end{aligned} \tag{78}$$

where ξ is the shear layer coordinate in streamwise direction. δ is the nominal boundary layer thickness and $C_{\tau,EQ}$ is equilibrium shear stress coefficient which are given by Equations 23 and 24 in reference [64]. The kinetic energy shape parameter (H_k) is calculated by taking the density across the boundary layer constant which is given by Equation 9 in reference [64].

Equation (78) is used for the turbulent regions. The variable is the shear stress coefficient (C_τ). A rate equation is used instead of the shear stress equation for the laminar regions for which in the program a critical amplification factor is used. This equation determines the transition location when the amplitude growth of the Tollmien-Schlichting wave becomes equal to n_{crit}. The relationship used in the laminar region is given by Equation (79).

$$\frac{d\tilde{n}}{d\xi} = \frac{d\tilde{n}}{dRe_\theta}(H_k)\frac{dRe_\theta}{d\xi}(H_k, \theta) \tag{79}$$

This method is commonly known as e^N method. Re_θ is the momentum thickness Reynolds number. First term on the right hand side is the emprical rate between the amplification factor $\tilde{n}$ and the momentum thickness Reynolds number which is derived from the Orr-Sommerfield equation. When $\tilde{n}$ reaches the user entered value in the rate calculation, the transition from the laminar flow to the turbulent flow occurs at that point on the airfoil surface. Second term can be calculated by assuming that the boundary layer has a Falkner-Skan velocity profile. Then, the skin friction coefficient C_f and the dissipation coefficient are calculated from the Swafford formulation [66] for the turbulent regions. Equations (70), (72) and (78) which is the shear stress equation are used to solve for the main variables; the mass thickness, the momentum thickness and the shear stress coefficient. This nonlinear set of equation is solved iteratively using the Newton method. It is coupled with the inviscid solution using the edge velocity (u_e) and the source term. Detailed information for the inviscid-viscous coupling can be found in reference [64].

Compressibility corrections are applied on top of the subsonic solution in order to make the viscous-panel solution compressible in XFOIL. The correction factors found in the literature are formulated by Prandtl and Glauert, Karman and Tsien and Laitone. Prandtl-Glauert compressibility factor is given by Equation (80) and it is most commonly used to apply compressibility correction to wind tunnel test data as in McCroskey's classification [6] for the NACA 0012 airfoil test data or in Totah's classification [13] for the SC1095 airfoil test data.

$$C_p = \sqrt{1 - M^2}\, C_{p,0} \tag{80}$$

Karman-Tsien compressibility factor is given by Equation (81). Karman-Tsien compressibility correction factor is used in XFOIL.

$$C_p = \frac{C_{p,0}}{\sqrt{1 - M^2} + \frac{M^2}{1 + \sqrt{1 - M^2}} \frac{C_{p,0}}{2}} \tag{81}$$

In Equation (81), $C_{p,0}$ and C_p are the incompressible and the compressible pressure coefficients, respectively. Same relations are applicable between C_l, C_d and C_m as in C_p.

In this study, initially XFOIL has been integrated into Dymore to replace the aerodynamic performance tables with instantenaous sectional panel solutions. It is selected because the panel method is much faster than the Navier-Stokes solvers. However, in XFOIL, sometimes it is hard to obtain a viscous solution around the stall regions at large angles of attack. The solution can be obtained only by forcing the transition location or changing the other viscous parameters. However, these kind of adjustments are not simply applicable from the outer main program in the automatical process. Since the prediction capability of the panel code beyond the stall region is not satisfying, it has been decided to switch the panel code with an open source Navier-Stokes solver, SU2 in the multibody dynamics solver, Dymore. Therefore, sectional CFD analyses are also performed in SU2 for the calculation of aerodynamic coefficients Cl, Cd and Cm in coupled simulations. Dymore-XFOIL coupled program is first used for the low angle of attack case at which no collective input is given and the maximum angle of attack is 10 degrees at the blade root where the tangential speed is low. These results are given in section 0. Moreover, XFOIL is used to calculate the zero lift drag coefficient, Cd_0, in SU2 and Dymore coupled simulations. NACA0012 is a symmetric airfoil and the zero lift occurs when the angle of attack is zero. The zero lift drag coefficient can be calculated by setting the angle of attack to zero and taking the Mach number in the hub plane.

In this study, the total panel number on the airfoil surface is taken as 240 and the panel spacing is set to 0.01 at the leading edge of the airfoil. The maximum panel angle is 4.56 degrees. XFOIL model prepared is given in Figure 31.

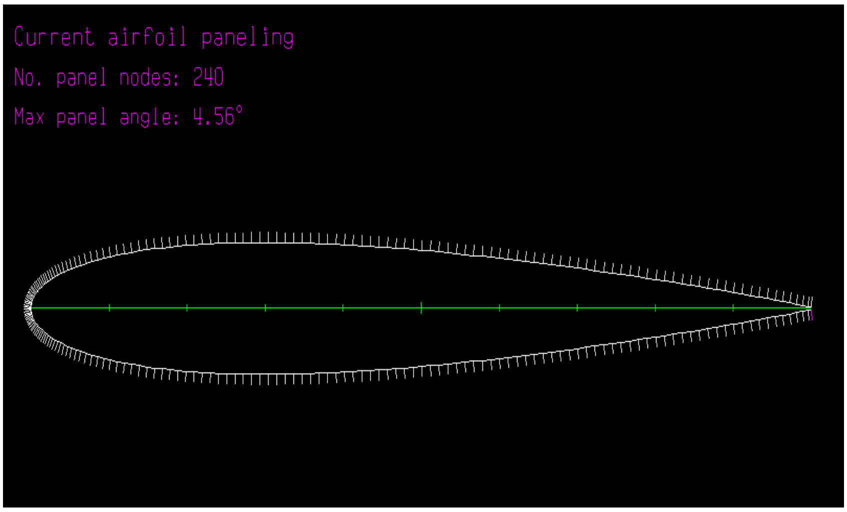
Current airfoil paneling

No. panel nodes: 240

Max panel angle: 4.56°

Figure 31 Airfoil Paneling for the NACA0012 Airfoil

In viscous parameters, the critical amplification factor is set to 4 which corresponds to a turbulence intensity level of 0.563 percent. The maximum iteration number is set to 1000. The transition is forced at the % 1 of the chord length on the top surface so that for all range of angle of attack, especially for the stall region, flow solution can be obtained in automatic calculation process. The transition is set free on the bottom surface of the airfoil. Parameters are summarized in Table 6.

Table 6 XFOIL Analysis Parameters

panel number	240
panel spacing at the leading edge	0.01
Reynolds number	0.75e-6
critical amplification factor	4
maximum iteration number	1000
transition location on top surface	0.01
transition location on bottom surface	1.00

As mentioned in Mayda's work [22], the compressibility correction may be invalid in XFOIL for high Mach numbers and high angle of attacks. For this reason he proposed to perform simulations in incompressible viscous setting by entering the Mach number as 0 and using the Mach-Reynolds proportionality constant of 12.4 x 10^6. Initially, in this study, XFOIL analyses are performed by using this proportionality constant and the Reynolds number is calculated by multiplying the Mach number with the proportionality constant. However, at the Mach number of 0.4, the Reynolds number becomes 0.4 x 12.4 x 10^6 = 4.96 x 10^6 which causes higher maximum lift coefficient and delayed stall prediction in XFOIL analyses. On the other hand, in the linear region, the coefficients calculated with the Reynolds number of 4.96 x 10^6 are in good correlation with the coefficients interpolated from the airfoil performance tables. In the XFOIL analyses and the XFOIL-Dymore coupled simulations, Reynolds number is set to 0.75 x 10^6 and the compressibility correction of Karman-Tsien which is given by Equation (81) is used.

2.4.2. SU2 – Unsteady Reynolds Averaged Navier-Stokes Solver

SU2 [67] is an open source RANS solver developed in Stanford University. It has one equation Spalart-Allmaras and two equation Menter-SST turbulence models. SU2 have many discretization schemes for time derivatives, convective terms, diffusive terms and turbulent terms for RANS equations. Available schemes are discussed shortly and the schemes which are used in this study are given in more detail in this section.

In SU2, the convective terms can be discretized in schemes of Roe, JST, Lax-Friedrich or CUSP, AUSM (Advanced Upstream Splitting Method), HLLC, TURKEL_PREC, MSW. Roe's scheme is an approximate Riemann solver. JST (Jameson-Schmidt-Turkel) scheme is a second order central difference scheme. Lax-Friedrich is unstable with CFL numbers larger than 1. In this study, Roe scheme is used for convective term discretization for the steady and the transient analyses. Implicit schemes are more stable than the explicit schemes in time discretization. Available schemes are Runge-

Kutta Explicit, Euler Explicit and Euler Implicit. Runge-Kutta Explicit is used in the transient analyses while Euler implicit scheme is used in the steady analyses. Spatial gradients in the diffusive terms can be calculated in the Weighted Least Squares or Green Gauss methods. Green Gauss may perform better for the unstructured and distorted grids and also it may act better in the flows with high Reynolds numbers in terms of convergence speed. Spatial derivatives in the turbulence equation is discretized with Scalar Upwind scheme. Order of this discretization can be 1st order, 2nd order or 2nd order with slope limiter. If the slope limiter is used Venkatakrishnan or minmod methods are available in SU2. The time discretization in the turbulence equation is in the implicit Euler scheme.

In the formulation of SU2 the conservative equations which are based on Reynolds Transport Theorem (RTT) are given in Equation (82) in integral form.

$$\frac{D}{Dt}\int_{\mathrm{V}(t)} \Phi d\Omega = \int_{\mathrm{V}(t)} \frac{\partial \Phi}{\partial t} d\Omega \; + \int_{S(t)} \Phi \vec{u} \cdot \vec{n}\, ds \tag{82}$$

Left side of Equation (82) is the material derivative which is the change in the conservative variable in a control mass according to the Lagrangian approach. Right side of the equation is formed from the quantity of the conservative variable which is produced inside the control volume and the quantity of conservative variable which enters or leaves through the control volume boundaries according to the Eulerian approach. Using the RTT equation the conservation of mass, momentum and energy equations can be derived. From the divergence theorem, the flux through the control surfaces can be written in terms of the divergence of the conservative variable as shown in Equation (83).

$$\int_{S(t)} \Phi \vec{u} \cdot \vec{n}\, ds = \int_{V(t)} \nabla \cdot (\Phi \vec{u}) d\Omega \tag{83}$$

Using Equation (83) and Reynolds Transport Equation (82) and by taking ϕ as ρ conservation of mass equation can be written as in Equation (84).

$$
\begin{aligned}
\frac{D}{Dt}\int_{\mathrm{V}(t)} \rho d\Omega &= \int_{\mathrm{V}(t)} \frac{\partial \rho}{\partial t} d\Omega \ + \ \int_{S(t)} \rho \vec{u} \cdot \vec{n}\, ds \\
&= \int_{\mathrm{V}(t)} \left(\frac{\partial \rho}{\partial t} + \nabla \cdot (\rho \vec{u}) \right) d\Omega = \ 0
\end{aligned}
\tag{84}
$$

The continuity equation in the differential form is given by Equation (85).

$$
\frac{D\rho}{Dt} = \frac{\partial \rho}{\partial t} + \nabla \cdot (\rho \vec{u}) = 0 \tag{85}
$$

Conservative momentum equation is given by Equation (86) in differential form as,

$$
\frac{\partial (\rho \vec{u})}{\partial t} + \nabla \cdot (\rho \vec{u}\vec{u}) = \nabla \cdot \bar{\bar{T}} + \rho \vec{f_b} \tag{86}
$$

where the first term is the time dependent term, the second term is the convective term, the third term is the diffusive term and the fourth term is the body force term. $\bar{\bar{T}}$ tensor is expressed in Equation (87) which consists of pressure and viscous parts. Shear stress tensor is given by Equation (88).

$$
\bar{\bar{T}} = -p\bar{\bar{\mathrm{I}}} + \bar{\bar{\tau}} \tag{87}
$$

$$
\bar{\bar{\tau}} = \mu \left[\nabla \vec{u} + (\nabla \vec{u})^T - 2 \frac{(\nabla \cdot \vec{u})}{3} \bar{\bar{\mathrm{I}}} \right] \tag{88}
$$

Conservative energy equation in differential form is given by Equation (89).

$$
\frac{\partial (\rho e_t)}{\partial t} + \nabla \cdot (\rho e_t \vec{u}) = \nabla \cdot \left(\bar{\bar{T}} \cdot \vec{u} \right) - \nabla \cdot \vec{q} + \vec{u} \cdot \rho \vec{f_b} \tag{89}
$$

where the first term is thet time rate of change of the total energy, the second term is the total energy flux, the third term is the rate of work done by the surface forces, the fourth term is the rate of the heat transfer and the fifth term is the rate of work done by the body forces. Conservative variables are $\{\rho, \rho u, \rho v, \rho w, \rho e_t\}$. System of equation can be combined in the differential form as shown in Equation (90).

$$\frac{\partial}{\partial t}\begin{Bmatrix}\rho\\ \rho\vec{u}\\ \rho e_t\end{Bmatrix}+\nabla\cdot\begin{Bmatrix}\rho\vec{u}\\ \rho\vec{u}\vec{u}-\bar{\bar{T}}\\ \rho e_t\vec{u}+\vec{q}-\bar{\bar{T}}\cdot\vec{u}\end{Bmatrix}=\begin{Bmatrix}0\\ \rho\vec{f}_b\\ \vec{u}\cdot\rho\vec{f}_b\end{Bmatrix} \tag{90}$$

Differential forms are used for the finite difference method while integral forms are used for the finite volume method. The integral form of the equation set given in differential form by Equation (90) is used in the formulation in SU2. Reynolds averaging part is summarized by refering to reference [68]. Instantaneous velocity at any field point in the computation domain is formed by the time averaged mean velocity and the time dependent oscillatory velocity.

$$u(x,t)=\bar{u}(x)+u'(x,t) \tag{91}$$

Reynolds Averaged Navier-Stokes equations can be expressed in nonconservative form as,

$$\rho\left(\frac{\partial\overline{u_i}}{\partial t}+\overline{u_k}\frac{\partial\overline{u_i}}{\partial x_k}\right)=-\frac{\partial\bar{p}}{\partial x_i}+\frac{\partial}{\partial x_j}\left(\mu\frac{\partial\overline{u_i}}{\partial x_j}\right)+\frac{\partial R_{ij}}{\partial x_j} \tag{92}$$

where Reynolds stresses are given by Equation (93).

$$R_{ij}=-\rho\overline{u_i'u_j'} \tag{93}$$

Boussinesq hypothesis relates Reynolds stresses to the mean rate of deformations using the eddy viscosity given by Equation (94),

$$\begin{aligned}R_{ij}=-\rho\overline{u_i'u_j'}=\mu_t\left(\frac{\partial\overline{u_i}}{\partial x_j}+\frac{\partial\overline{u_j}}{\partial x_i}\right)-\frac{2}{3}\mu_t\frac{\partial u_k}{\partial x_k}\delta_{ij}\\ -\frac{2}{3}\rho k\delta_{ij}\end{aligned} \tag{94}$$

where the turbulence kinetic energy k is given by Equation (95).

$$k=\frac{1}{2}\left(\overline{u'^2}+\overline{v'^2}+\overline{w'^2}\right) \tag{95}$$

Equations are developed to predict the Reynolds stresses, starting from the algebraic models, one equation model of Spalart-Allmaras (SA), two equation models; k-ε and k-ω, seven equation Reynolds Stress Model (RSM) to additional transitional models with turbulence models; k-kl-ω and Langtry-Menter SST transition model while increasing the complexity and the computational cost. Detached Eddy Simulation (DES) and Large Eddy Simulation (LES) are more costly than the methods above and less costly than Direct Numerical Simulation (DNS). Spalart-Allmaras is useful for bigger meshes and it is computationally cheaper. However, it performs worse than the two equation models if there is large flow separation. k-ε models are robust; however, k-ω models performs better than k-ε models for the boundary layer flows. k-ε models require y+ value bigger than 30 when the wall functions are used while k-ω models require y+ value less than 1. SU2 currently has standard formulation of Spalart-Allmaras (SA) model [69], the modified form of the Spalart-Allmaras model [70] (SA-neg) and the Menter's Shear Stress Transport model (SST) [71]. In this study k-ω SST turbulence model is used since it is prescribed as a good combination between standard k-ε and k-ω models [67]. The formulation of SA and SST models are summarized in the next subsections.

SA turbulence model [69] is one equation turbulence model governed by a second order partial differential equation given in the nonconservative form by Equation (97) where the state variable is turbulent kinematic viscosity ($\tilde{v}$). Next, this variable is plugged into the equation (96) to calculate the turbulent eddy viscosity (μ_t) .

$$\mu_t = \rho \tilde{v} f_{v1} \tag{96}$$

$$\begin{aligned} \frac{\partial \tilde{v}}{\partial t} + u_j \frac{\partial \tilde{v}}{\partial x_j} &= c_{bl}(1 - f_{t2})\tilde{S}\tilde{v} - \left[c_{w1} f_w - \frac{c_{b1}}{\kappa^2} f_{t2}\right]\left(\frac{\tilde{v}}{d}\right)^2 \\ &+ \frac{1}{\sigma}\left[\frac{\partial}{\partial x_j}\left((v + \tilde{v})\frac{\partial \tilde{v}}{\partial x_j}\right) + c_{b2}\frac{\partial \tilde{v}}{\partial x_i}\frac{\partial \tilde{v}}{\partial x_i}\right] \end{aligned} \tag{97}$$

In the standard SA equation is given by Equation (97), f_{v1}, x and the kinematic viscosity "v" are given by Equation (98),

$$f_{v1} = \frac{x^3}{x^3 + c_{v1}^3}, \quad x = \frac{\tilde{v}}{v}, \quad v = \frac{\mu}{\rho} \tag{98}$$

and f_{t2} and f_w are given by Equation (99).

$$f_{t2} = c_{t3}\exp(-c_{t4}x^2), \qquad f_w = g\left[\frac{1+c_{w3}^6}{g^6+c_{w3}^6}\right]^{\frac{1}{6}}$$
$$g = r + c_{w2}(r^6 - r), \qquad r = \min\left[\frac{\tilde{v}}{\tilde{S}\kappa^2 d^2}, 10\right] \tag{99}$$

$\tilde{S}$ tensor is given by Equation (100).

$$\tilde{S} = \Omega + \frac{\tilde{v}}{\kappa^2 d^2} f_{v2}, \quad \Omega = \sqrt{2W_{ij}W_{ij}}, \quad W_{ij} = \frac{1}{2}\left(\frac{\partial u_i}{\partial x_j} - \frac{\partial u_j}{\partial x_i}\right) \tag{100}$$

f_{v2} is given by Equation (101).

$$f_{v2} = 1 - \frac{x}{1 + x f_{v1}} \tag{101}$$

In the above equations, constants are given by Equation (102).

$$c_{b1} = 0.1355, \qquad c_{b2} = 0.622,$$
$$c_{w2} = 0.3, \qquad c_{w3} = 2,$$
$$c_{v1} = 7.1, \qquad c_{t3} = 1.2, \qquad c_{t4} = 0.5, \qquad \kappa = 0.41, \tag{102}$$
$$c_{w1} = \frac{c_{b1}}{\kappa^2} + \frac{1 + c_{b2}}{\sigma}, \qquad \sigma = \frac{2}{3}$$

Finally, boundary conditions are given by Equation (103).

$$\tilde{v}_{wall} = 0, \qquad \tilde{v}_{farfield} = 3V_\infty : to : 5V_\infty \tag{103}$$

Menter-SST [71] is a two equation turbulence model which is formulized as a blending between k-ε and k-ω turbulence models. State variables are the turbulence kinetic energy (k) and the specific dissipation rate (ω). Turbulence eddy viscosity is given by Equation (105).

$$\mu_t = \frac{\rho a_1 k}{max(a_1 \omega, \Omega F_2)} \tag{104}$$

The transport equation is written for the turbulent kinetic energy in the conservative form as,

$$\begin{aligned} \frac{\partial(\rho k)}{\partial t} + \frac{\partial\left(\rho \overline{u_j} k\right)}{\partial x_j} \\ &= R_{ij} \frac{\partial \overline{u_\imath}}{\partial x_j} - \beta^* \rho \omega k \\ &+ \frac{\partial}{\partial x_j}\left[(\mu + \sigma_k \mu_t) \frac{\partial k}{\partial x_j}\right] \end{aligned} \tag{105}$$

where ρ is the density, k is turbulent kinetic energy, ω is the specific dissipation rate, $\overline{u_j}$ is the average mean velocity, R_{ij} is Reynolds stress tensor, μ is dynamic viscosity and μ_t is turbulent eddy viscosity.

Specific dissipation rate is written in the conservative form as,

$$\begin{aligned} \frac{\partial(\rho \omega)}{\partial t} + \frac{\partial\left(\rho \overline{u_j} \omega\right)}{\partial x_j} \\ &= \frac{\gamma}{\upsilon_t} R_{ij} \frac{\partial \overline{u_\imath}}{\partial x_j} - \beta \rho \omega^2 \\ &+ \frac{\partial}{\partial x_j}\left[(\mu + \sigma_\omega \mu_t) \frac{\partial \omega}{\partial x_j}\right] \\ +2(1 - F_1) \frac{\rho \sigma_{\omega 2}}{\omega} \frac{\partial k}{\partial x_j} \frac{\partial \omega}{\partial x_j} \end{aligned} \tag{106}$$

where ρ is the density, k is turbulent kinetic energy, ω is the specific dissipation rate, $\overline{u_j}$ is the average mean velocity, R_{ij} is Reynolds stress tensor, μ is dynamic viscosity, μ_t is turbulent eddy viscosity and υ_t is the turbulent kinematic viscosity.

Reynolds stress tensor is given by Equation (107).

$$R_{ij} = \mu_t\left(\frac{\partial \overline{u_i}}{\partial x_j} + \frac{\partial \overline{u_j}}{\partial x_i} - \frac{2}{3}\frac{\partial u_k}{\partial x_k}\delta_{ij}\right) - \frac{2}{3}\rho k \delta_{ij} \tag{107}$$

The variables used in Equations (105) and (106) are calculated according to Equation (108) in order to blend the coefficients of the k-ε model given as ϕ_1 and the k- ω model given as ϕ_2.

$$\phi = F_1\phi_1 + (1 - F_1)\phi_2 \tag{108}$$

F_1 and F_2 functions are given by Equation (109).

$$F_1 = \tanh(arg_1^4)\,, \qquad F_2 = \tanh(arg_2^2) \tag{109}$$

arg_1 and arg_2 terms are given by Equations (110) and (112) respectively.

$$arg_1 = \min\left[\max\left(\frac{\sqrt{k}}{0.09\omega y}, \frac{500\nu}{y^2\omega}\right), \frac{4\varrho\sigma_{\omega 2}k}{CD_{k\omega}y^2}\right] \tag{110}$$

In Equation (110), y is the distance from the wall and $CD_{k\omega}$ is the cross-diffusion term which is given by Equation (111).

$$CD_{k\omega} = \max\left(2\rho\sigma_{\omega 2}\frac{1}{\omega}\frac{\partial k}{\partial x_j}\frac{\partial \omega}{\partial x_j}, 10^{-20}\right) \tag{111}$$

$$arg_2 = max\left(2\frac{\sqrt{k}}{0.09\omega y}, \frac{500\nu}{y^2\omega}\right) \tag{112}$$

The coefficients which show up in the k-ε model are given in Equations (113) and (114).

$$\phi_1 = \{\sigma_{k_1}, \sigma_{\omega_1}, \beta_1, \gamma_1\} \tag{113}$$

$$\sigma_{k_1} = 0.85, \qquad \sigma_{\omega_1} = 0.5, \qquad \beta_1 = 0.075$$

$$\gamma_1 = \frac{\beta_1}{\beta^*} - \frac{\sigma_{\omega_1}\kappa^2}{\sqrt{\beta^*}} = 0.553 \tag{114}$$

The coefficients which show up in the k- ω model are given in Equations (115) and (116).

$$\phi_2 = \{\sigma_{k_2}, \sigma_{\omega_2}, \beta_2, \gamma_2\} \tag{115}$$

$$\sigma_{k_2} = 1.0, \qquad \sigma_{\omega_2} = 0.856, \qquad \beta_2 = 0.0828$$

$$\gamma_2 = \frac{\beta_2}{\beta^*} - \frac{\sigma_{\omega_2}\kappa^2}{\sqrt{\beta^*}} = 0.44 \tag{116}$$

Other coefficients are given in Equation (117).

$$a_1 = 0.31, \qquad \kappa = 0.41 \tag{117}$$

In the present study, Dymore-SU2 integration has been performed and SU2 runs have been called from Dymore for the solution of the compressible viscous flow. During the Dymore simulations for the hover condition, the sectional angle of attack can exceed the stall angle. Therefore, in the present study two dimensional aerodynamic analyses have been performed in SU2 in order to compare the lift and the drag coefficients with the experimental data available for the NACA 0012 airfoil. For this purpose, the angle of attack range is selected as -5^{o} to 20^{o}. SU2 analyses have been performed in this angle of attack range with increments of 1^{o} for Mach numbers 0.4 and 0.7. It has been noted that around the stall angles, it is hard to get a converged solution in the steady analysis. Hence, the steady analysis is turned into the transient analysis as explained in the sectional CFD analysis methodology presented in Figure 32. Lift, drag and moment coefficients are calculated from the time history data of the transient CFD analysis by calculating the mean value of time dependent data between two maximum peaks.

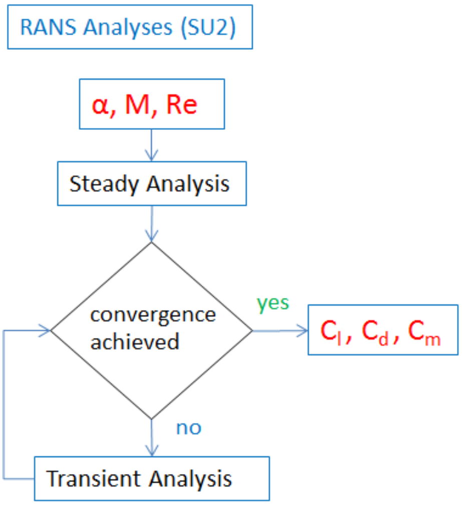

Figure 32 SU2 Steady and Transient Analyses Methodology

Freestream properties are calculated in SU2 in the following manner;

- The speed of sound is calculated from the gas constant and the freestream temperature.
- The freestream velocity is calculated from the angle of attack and the Mach number.
- The freestream viscosity is calculated from Sutherlands Law using the freestream temperature. Sutherlands Law is given in Equation (118),

$$\mu = \mu_{ref}\left(\frac{T}{T_{ref}}\right)^{3/2}\frac{T_{ref}+S}{T+S} \tag{118}$$

where T_{ref} is the reference temperature, μ_{ref} is the reference viscosity at the reference temperature and S is the Sutherland temperature.

- Using the Reynolds number, the freestream temperature, the freestream viscosity and the freestream velocity, freestream density is calculated from,

$$Re = \frac{\rho_\infty V_\infty c}{\mu} \tag{119}$$

where V_∞ is the flow velocity, ρ_∞ is the freestream density, c is the chord length and μ is the freestream viscosity. Finally, the freestream pressure is calculated from the perfect gas law using the freestream temperature, the gas constant and the freestream density. Nondimensionalization can be applied to the flow properties. The flow properties used in SU2 analyses are given in Table 7. SU2 parameters is set for the compressible flow.

Table 7 Flow Properties

Reynolds Number	6.5x10^6
T_freestream	288.15 K
Specific heat ratio	1.4
Gas constant	287.87 J/(kgK)
Prandtl number (laminar)	0.72
Prandtl number (turbulent)	0.9
Bulk modulus	1.42e5

Computational grid which is shown in Figure 33 is prepared using Pointwise software with the help of the record macro option. An automatic script is generated when the grid is created. Then, only by changing the parameters in the script, a mesh having the desired properties can be regenerated. A code is written in FORTRAN to read the mesh parameters from a text file and create the executable Pointwise macro which is given in Appendix D. The grid parameters are summarized in Table 8.

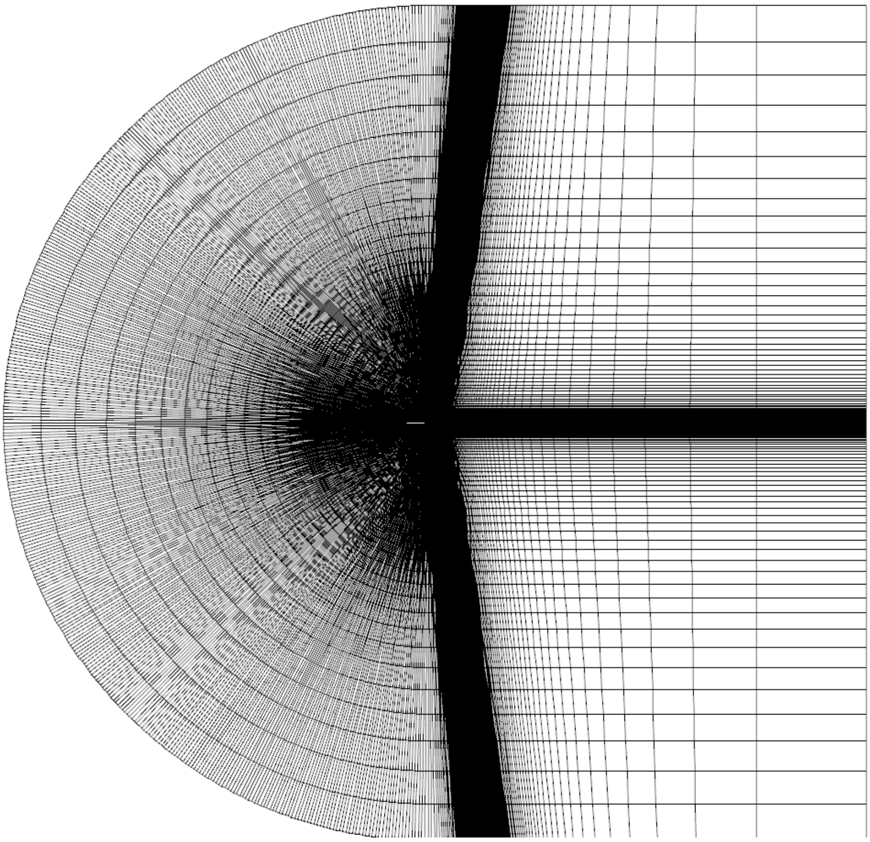

Figure 33 NACA0012 C-grid used in SU2 analyses

Figure 34 shows the grid density around the airfoil surface where wall boundary condition is defined.

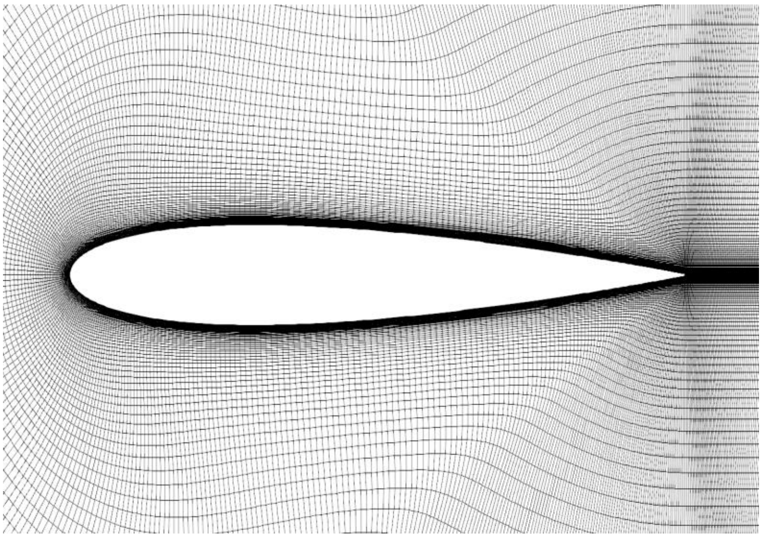

Figure 34 Grid spacing around airfoil surface

Figure 35 shows the grid distribution at the blunt trailing edge of the airfoil.

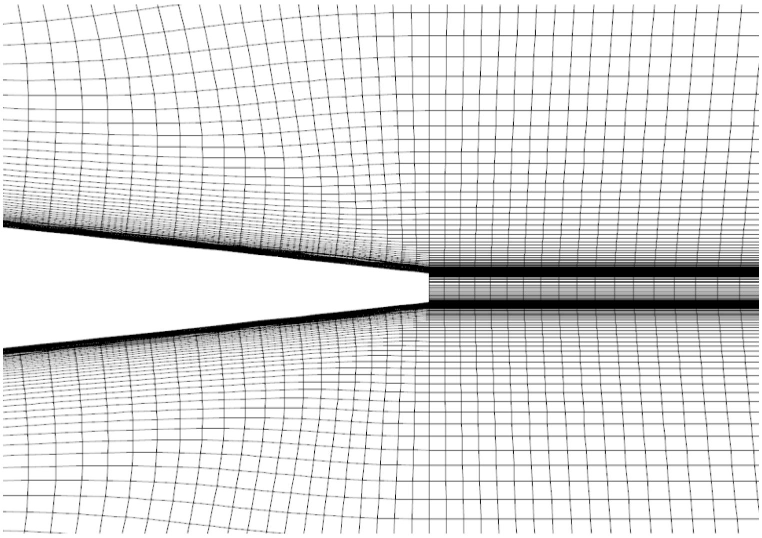

Figure 35 Grid spacing around trailing edge

The farfield is prescribed as the pressure farfield and the airfoil is prescribed as the wall boundary condition with no heat flux across it. Multigrid acceleration is switched off during the automatized sweep simulations because of the reason that it may cause the divergence.

Table 8 Grid Properties

Grid topology	c-grid
Type	structured
Domain size	439x151
Total cell count	115913
Growth rate	1.1
Surface points	400
First wall height	1e-6
Leading edge spacing	0.001
Trailing edge spacing	0.001
Stop height	15 chords

A summary of the discretization parameters used in the steady and the transient analyses are given in Table 9. Convective terms are discretized using the Roe flux splitting methodology. Time discretization is the implicit scheme for the steady analyses and the explicit scheme for the transient analyses. If the solution does not converged in steady analysis, analysis type is switched to transient analysis.

Table 9 Discretization Parameters

flux discretization	Roe
spatial discretization	2nd order limiter
slope limiter	Venkatakrishnam
time discretization	Euler Implicit
turbulence	scalar upwind
spatial order	1st order
spatial gradients	Green Gauss

Analysis parameters used in the steady computations are given in Table 10.

Table 10 Steady Analysis Parameters

CFL Number	30
residual	1e-12
residual criteria	drag
total iteration number	500

Analysis parameters used in the unsteady computations are given in Table 11.

Table 11 Unsteady Analysis Parameters

temporal scheme	2nd order dual time stepping
time step	0,00235
CFL Number	10
residual	1e-12
residual criteria	drag
internal iteration number	100
external iteration number	200

SU2 can be integrated into another program by changing its source code in order to turn it into a subroutine and compile as a static or dynamic library. In this process, SU2 is called from the main program automatically. In order to preserve code structure, only the angle of attack, the Mach number and the Reynolds number are sent to SU2 subroutine. Other parameters are kept same in the steady and transient analysis which are read from the SU2 input files.

2.5. Comprehensive Analysis

In this study, an isolated main rotor architecture which is described in section 2.2.3 is modeled in Dymore. Analysis methodology is to make a trim analysis first and to continue with the dynamic simulation. In the trim analysis a linear automatic controller is used which is basically a Jacobian matrix between the trim inputs and the targets. The trim targets are the rotor thrust, the roll moment and the pitch moment around the rotor hub while the trim variables are the collective, the longitudinal cyclic and the lateral cyclic swashplate inputs. Once the trim targets are reached in the first dynamic analysis, simulations are performed at the trim conditions to compare the lookup table results with the CFD coupled results. The comprehensive analysis methodology followed in this study is given in Figure 36.

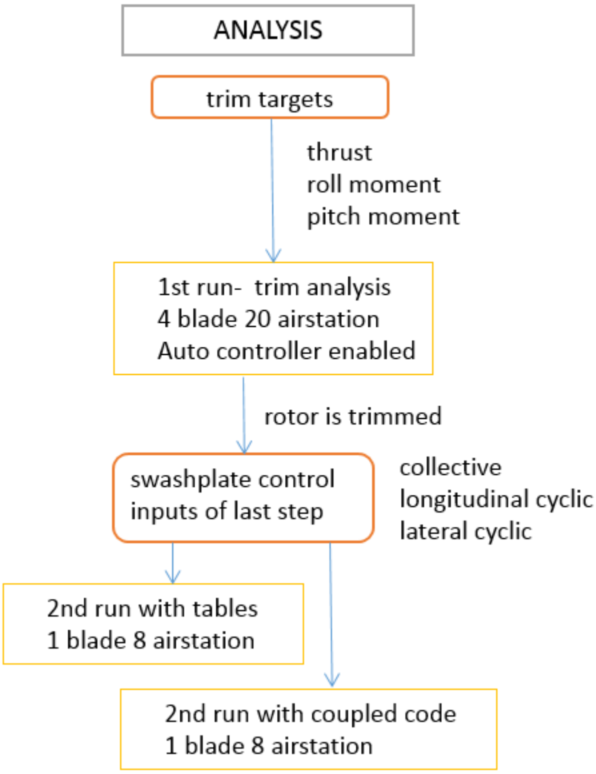

Figure 36 Methodology for the Comprehensive Analysis

In the trim analysis, aerodynamic calculations are performed by the interpolation from the aerodynamic performance tables prepared for NACA0012 which is given in Appendix A. Cl, Cd and Cm tables are supplemented to the program with an input file. In this study, these coefficients are calculated from the aerodynamic solvers instead of the lookup tables using the angle of attack and Mach number information. The calculated aerodynamic coefficients are resupplied to the aerodynamic stations of the dynamic model for the load calculation. More information related to Figure 36 is given in subsections 2.5.1, 2.5.2 and 2.5.3.

2.5.1. Eigenvalue Analysis and Static Analysis

Eigenvalue analysis is performed in Dymore at each time step of the static or dynamic analysis for the dynamic model when this option is set. Hence, the program calculates the natural frequencies and displays the mode shapes of the dynamic model if the user enables this option. For this study, the eigenvalue analysis is performed to compare the natural frequencies with the natural frequencies found in the literature only before the static analysis. Main purpose of the eigenvalue analysis is to verify that the model is constructed structurally correct. Natural frequencies of the dynamic model used in this thesis study are compared in Table 12 with the eigenvalues of the study carried out by Kumar [72].

Table 12 Mode Shapes and Natural Frequencies of the Dynamic Rotor Model

Mode Shape	UH60 Dymore Model		Reference [72]
	rad/s	/rev	rad/s
1st chordwise bending	7.13	0.26	7.26
1st flapwise bending	27.93	1.03	28
2nd flapwise bending	74.63	2.76	72.4
1st torsion	124.24	4.60	123.5
2nd chordwise bending	134.86	4.99	134.4
3rd flapwise bending	141.93	5.25	148

First natural frequency is the lead-lag frequency which completes its cycle approximately in four rotor rotation. The second and the third modes are 1st and 2nd flapping modes. After the eigenvalue analysis, the static analysis is performed by switching off the aerodynamics and the controller. Gravity and rigid rotation loads are applied in the static analysis. The rigid rotation stiffens the blades under the effect of the centrifugal force.

2.5.2. Trim Analysis

After the static equilibrium is reached, the rotor is trimmed to the hover condition in dynamic analysis using the linear controller. The trim analysis is performed using four blades each having 20 aerodynamic stations. The trim solution is obtained by using the aerodynamic lookup tables in the internal aerodynamic module of Dymore. The results are saved. The trim condition is achieved with a linear controller which constructs a gradient matrix (3x3) between the trim targets and the trim variables. The trim variables are swashplate inputs related to collective, longitudinal and the lateral cyclic inputs. The trim targets are thrust, pitching moment and rolling moment at the hub center. The rolling and the pitching moments are taken as zero for simplicity in the calculations. Trim airload at the end of the first simulation is summarized with the required control inputs. The collective input which is modified by the controller and the thrust versus time plots are given in Figure 37 during an interval of 20 seconds of the trim simulation. Only the collective input is plotted since cyclic inputs are assumed to be zero.

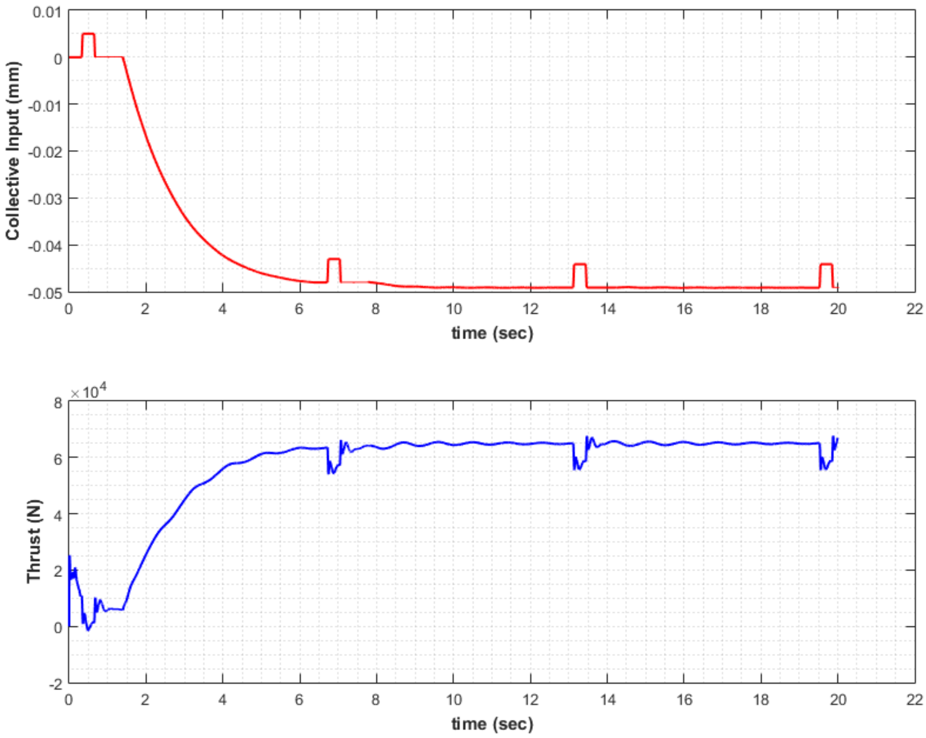

Figure 37 Collective Input and Thrust vs time plots throughout Trim Analysis

In Figure 37, the steady value of the collective input is 50 mm and the steady value of the rotor thrust is 65000 N which are the trim values. Linear controller calculates Jacobian matrix between the trim targets and the trim inputs in disturbed regions which can be seen in Figure 37. The controller gives smaller perturbations to the trim inputs and monitors the change in the trim targets in time marching solution.

2.5.3. Simulation Analysis

Second dynamic analysis is started with the control inputs at the end of the first simulation. In this analysis, the automatic controller is deactivated. Instead of four blade analysis, one blade is used for the rotation to save from the computational effort. The time step size is selected so that 5^o azimuthal spacing is attained between the time steps in the rotation. This analysis is performed using the aerodynamic performance tables of NACA 0012 given in Appendix A. The same analysis is also performed with the Dymore and XFOIL/SU2 coupled suite. However, the coupled simulations with RANS are computationaly expensive. Hence in the coupled simulations 8 airstations are used for 1 blade. The flexible set of the multibody system is nonlinear. Therefore, 5 Newton iterations are performed at each time step. The results are given in section 3.2.

2.5.4. Coupling of XFOIL and SU2 with Dymore

In this study, source codes of DYMORE (C), XFOIL (FORTRAN) and SU2 (C++) are compiled together. Dymore is the main program. SU2 and XFOIL are written as subroutines and they are called from the main program. Dymore and XFOIL are coupled by directly passing variables between the subroutine and the main program using the C-Fortran interoperability functions. Figure 38 describes the coupling methodology implemented.

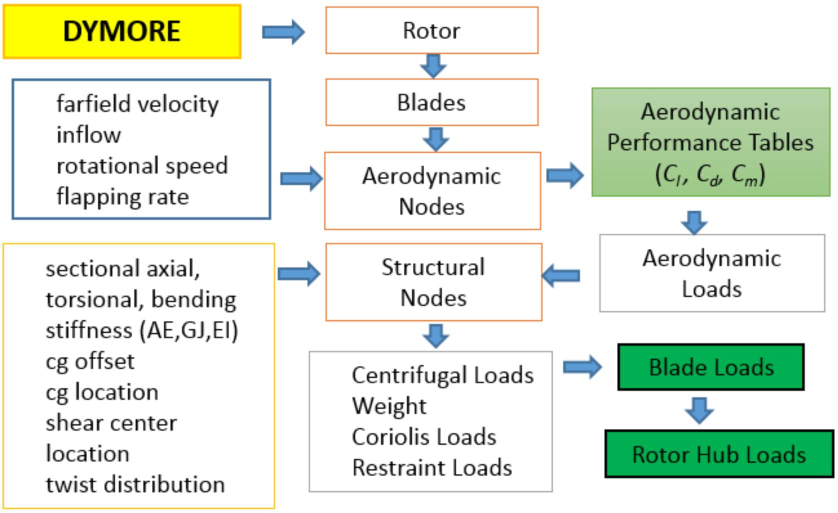

(a) Aerodynamic coefficients are read from look-up tables

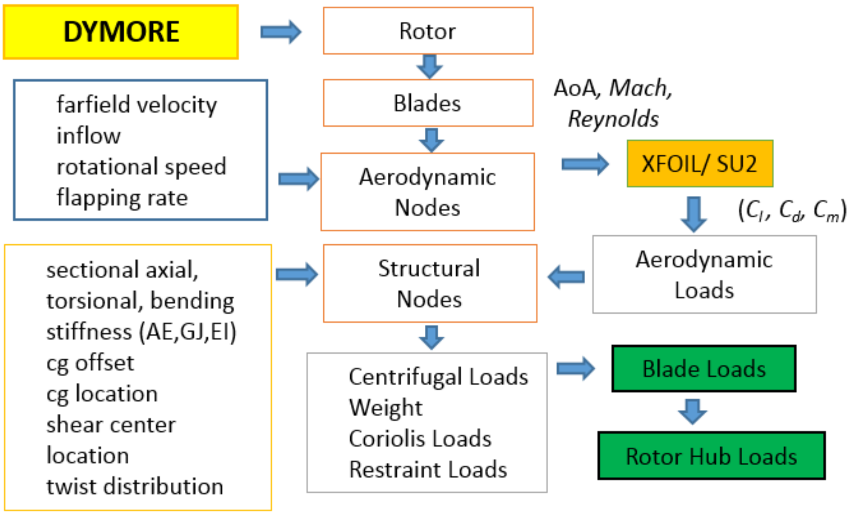

(b) Aerodynamic coefficients are calculated with CFD analysis

Figure 38 Coupling Methodology of the Multibody Dynamics Code Dymore and XFOIL/SU2

During the multibody simulation of the rotor in Dymore, the information on the effective angle of attack, the Mach number and the Reynolds number are passed to SU2 and XFOIL subroutines. The aerodynamic coefficients are returned from XFOIL by passing coefficients directly. The coefficients are written to a shared external structure in SU2 where the main program gets the coefficients.

2.5.5. Parallelization

Dymore (C) and SU2 (C++) coupled program is parallelized using Message Passing Interface (MPI) functions. Total computation is performed with 128 processors for 8 aerodynamic sections. Each aerodynamic section of the rotor blade is solved on a separate group of 16 processors. For each section, domain is partitioned with Metis subroutines which are already embedded in SU2. For this implementation, **“MPI_Comm_Split”** function is used to split the communication world of 128 processors into 8 communication worlds each consisting of 16 processors. Dymore and XFOIL are made parallel by distributing 8 section to 8 head cores of 128 processors. Figure 39 shows the double level parallel computation in SU2 and DYMORE coupled simulations.

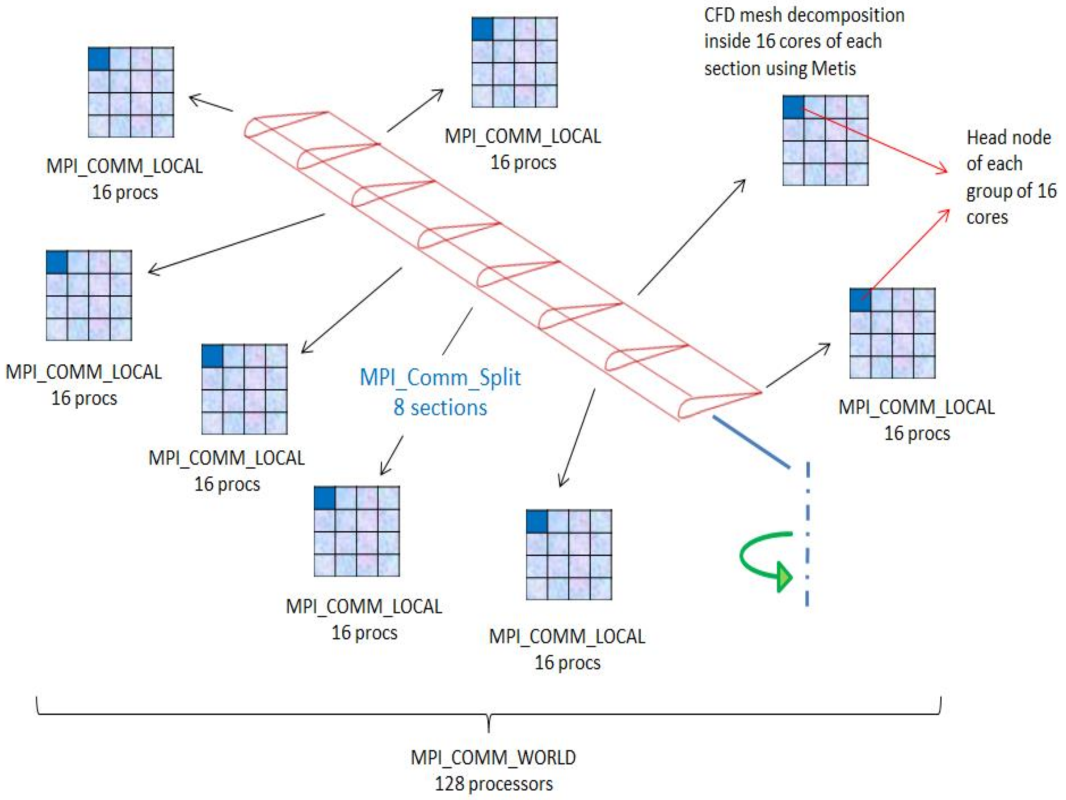

Figure 39 Double Level Parallel Computation in SU2 and DYMORE Coupled Simulations

CHAPTER 3

RESULTS OF COUPLED XFOIL/SU2-DYMORE ANALYSIS

In this chapter, firstly, sectional validation studies are performed to compare the aerodynamic coefficients obtained from XFOIL and SU2 with the aerodynamic coefficients interpolated from the lookup tables given in Appendix A. The sectional analyses are performed at the Mach numbers of 0.4 and 0.7 for the angle of attack range between -5^{o} and 15 ^{o}. Selected cases for the sectional analyses are illustrated after the comparison data of the sweep analyses. The pressure coefficient distribution and the boundary layer velocity profiles are given for XFOIL cases as well as the numerical data for the lift and the drag coefficients. Similarly, the pressure, the eddy viscosity and the Mach contours are plotted for SU2 cases. Also, the evolution of the lift and the drag coefficients over the iteration history are given for SU2 cases. A case at which the angle of attack is near to the stall condition is solved with the transient analysis in SU2. In the second section, coupled analyses in Dymore and XFOIL/SU2 are given in three subsections. First part contains the solution obtained from the Dymore-XFOIL coupled simulation which is obtained by only rotating the rotor without giving any pilot input. The reason is that XFOIL may not calculate the aerodynamic coefficients at large angles of attack. In this case, the transition location parameters should be changed in order to obtain the solution in XFOIL. However, in this automatized process it is not easy to change these parameters. Hence, the CFD tool of the coupled program is switched to SU2. In the second subsection, SU2 simulation is validated with the first case in which no control input exists. In the last subsection, results related to Dymore-SU2 coupled simulation that run by applying collective input are given. All simulations are compared with the table lookup simulations. The compared data are the blade angles and the rotor airloads at the hub center.

3.1. Validation of Two Dimensional Sectional Analysis

Before moving on to coupled simulations with the comprehensive code, the sectional CFD analyses are performed to validate the XFOIL and SU2 data with the look-up table data using parameters which are given in sections 2.4.1 and 2.4.2. Two dimensional sectional analyses for the NACA0012 profile are performed at Mach numbers between 0 and 1 at the angles of attack through -5^o to 15 ^{o}. However as mentioned in reference [15] most governing sections of the helicopter blade are exposed to Mach numbers of 0.4 and 0.7. Therefore, the validation analyses are performed at Mach numbers 0.4 and 0.7. The data obtained from the automatized analyses in XFOIL and SU2 are compared with the experimental table data of NACA0012. The steady analyses are performed in SU2 between angles of attack of -5^o to 10^o. After 10^o angle of attack, transient analyses are performed. In the transient analyses, the flow separation is observed after 13^o angle of attack. SU2 analyses are performed for Reynolds number of 6.5 million. This Reynolds number is taken from the study of Mayda and Dam [22] in which generation of aerodynamic coefficient tables are automatized. The analysis type is compressible viscous both in SU2 and in XFOIL.

3.1.1. SU2/XFOIL Simulations at Mach 0.4

The lift and drag coefficients obtained by XFOIL and SU2 simulations are compared with the aerodynamic performance table values for the NACA0012 profile in Figures 40 and 41 at Mach 0.4. Sweep analyses are performed at Reynolds number of 0.75 million in XFOIL while the analyses are performed at a Reynolds number of 6.5 million in SU2. In XFOIL analysis, the closest results to the table values are obtained at Reynolds number of 0.75 million while at Reynolds number of 6.5 million, XFOIL gives unreasonable results which are higher maximum lift coefficient prediction and delayed stall angle of attack. It is also stated in the manuals of XFOIL that XFOIL is applicable to the problems which have Reynolds number of 0.5 x 10^6.

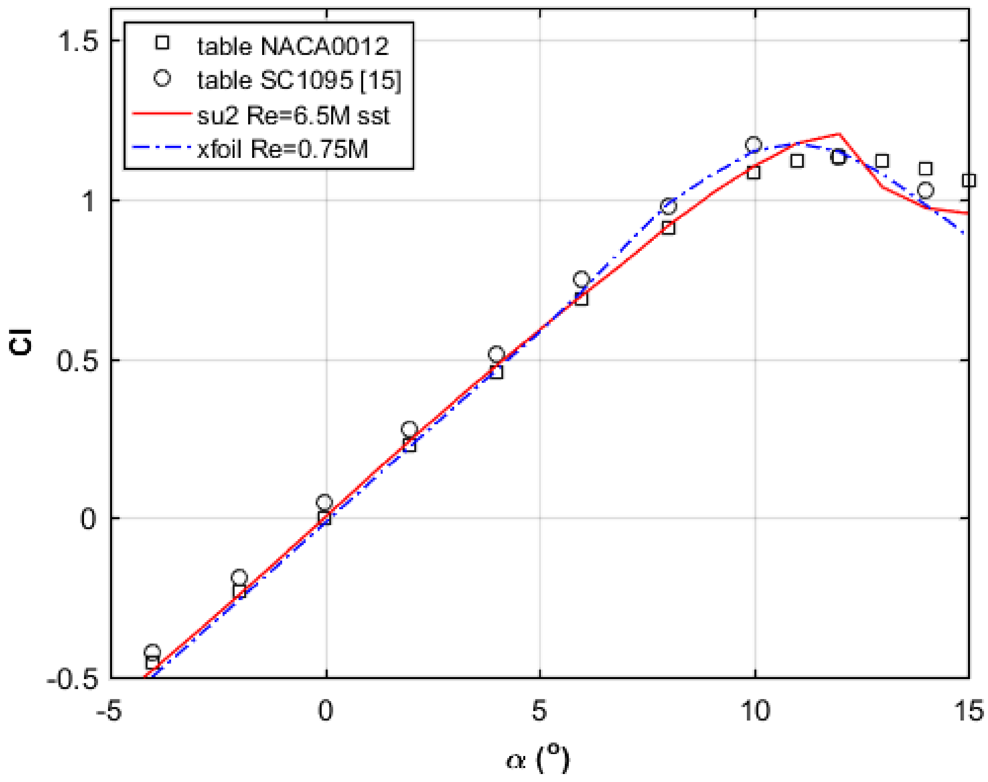

Figure 40 Cl Comparison of Angle of Attack Sweep at M=0.4 between XFOIL, SU2 and Aerodynamic Coefficients Lookup Table

In Figure 40, it is noticed that the lift coefficient prediction in XFOIL is a little higher than the airfoil table values close to the stall region. In this region, the compressibility correction may not be applied by the program since the local speed becomes too high on the airfoil surface. The reason is that the compressibility corrections are applicable when the flow Mach number is less than 1. It should be noted that the flow becomes supersonic on the airfoil surface if the oncoming flow speed is high. On the other hand, using the Mach-Reynolds proportionality constant to the Reynolds number without the compressibility correction gives good correlation in the linear region; however, it causes delay in the stall angle of attack and predicts maximum lift coefficient 50% higher. This case is not plotted here since the results are not reasonable. Figure 40 shows the good agreement between the coefficients obtained from SU2, XFOIL and the coefficients existed in the lookup table for the linear regions. In the stall region, the coefficients obtained from SU2 and XFOIL are not close enough to table coefficients in order to accurately predict the flow separation behavior. Detached Eddy Simulation (DES) may be performed to predict the stall behavior correctly; however, DES is computationally more demanding.

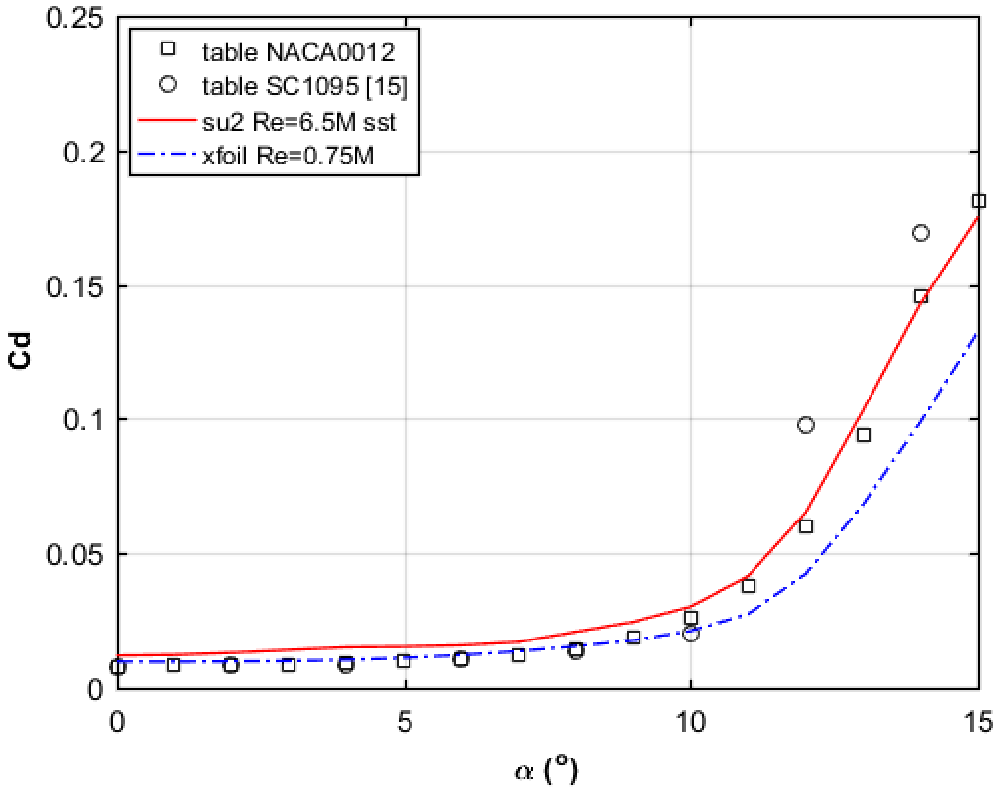

Figure 41 Cd Comparison of Angle of Attack Sweep at M=0.4 between XFOIL, SU2 and Aerodynamic Coefficients Lookup Table

As seen from Figure 41, similar behavior can be observed in the drag coefficient sweep between SU2, XFOIL and the performance table. XFOIL drag coefficient prediction is closer to the performance table drag coefficient for angles of attack below the drag divergence than the SU2 drag coefficient prediction. For high angles of attack, SU2 gives closer prediction to the lookup table values. The lookup tables are taken from the UH-60 test cases which can be found within the folders of the comprehensive analysis tools of Dymore, Flightlab or CHARM; however, the composition and the reference to the tables are not clear. For example, there is not enough information about the Reynolds number at which the table is prepared or on the method used for the determination of the aerodynamic coefficients. Whether the CFD analysis, wind tunnel tests or the extrapolation method is used is not clear. This is also specified in a previous work done by [73] (section 4.1.1).

The Cp distribution and the boundary layer profiles on the airfoil surface are given for angles of attack of 5°, 10°, 15° and 20° at Mach number of 0.4 in Figures 42-45. These results are taken from XFOIL computations.

3.1.1.1. Solution at M= 0.4 and α=5° in XFOIL

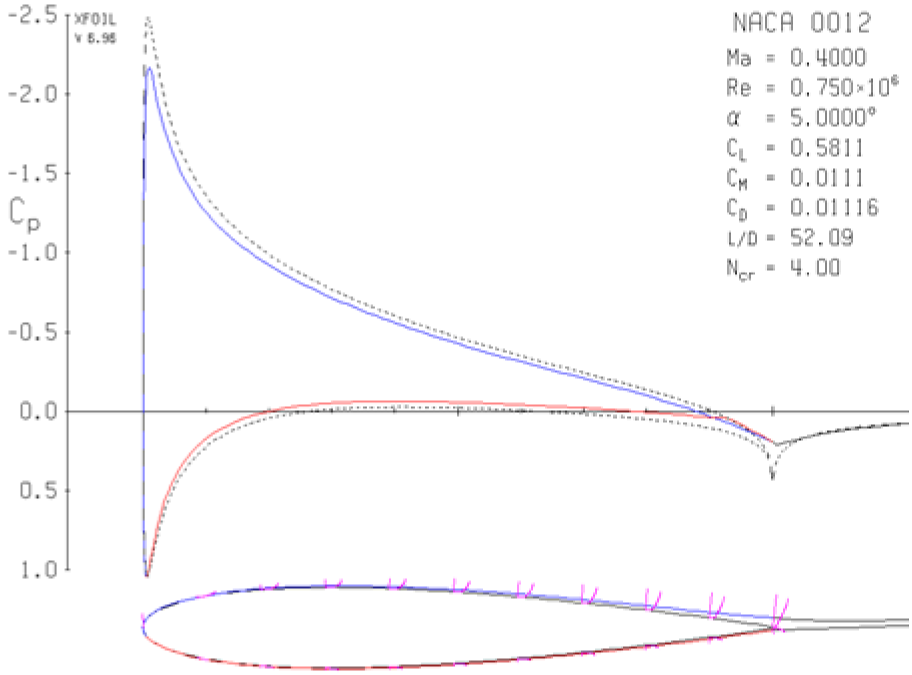

Figure 42 Cp Distribution of NACA 0012 at Mach 0.4 at 5 degrees Angle of Attack / XFOIL Computation

In Figures 42-45, the inviscid solution is given with the dashed line for which the viscous boundary layer effect is not included. Pink lines on the airfoil surface shows the velocity profiles in the boundary layer. It can be interpreted from the boundary layer velocity profiles that the flow is laminar and attached.

3.1.1.2. Solution at M= 0.4 and α=10° in XFOIL

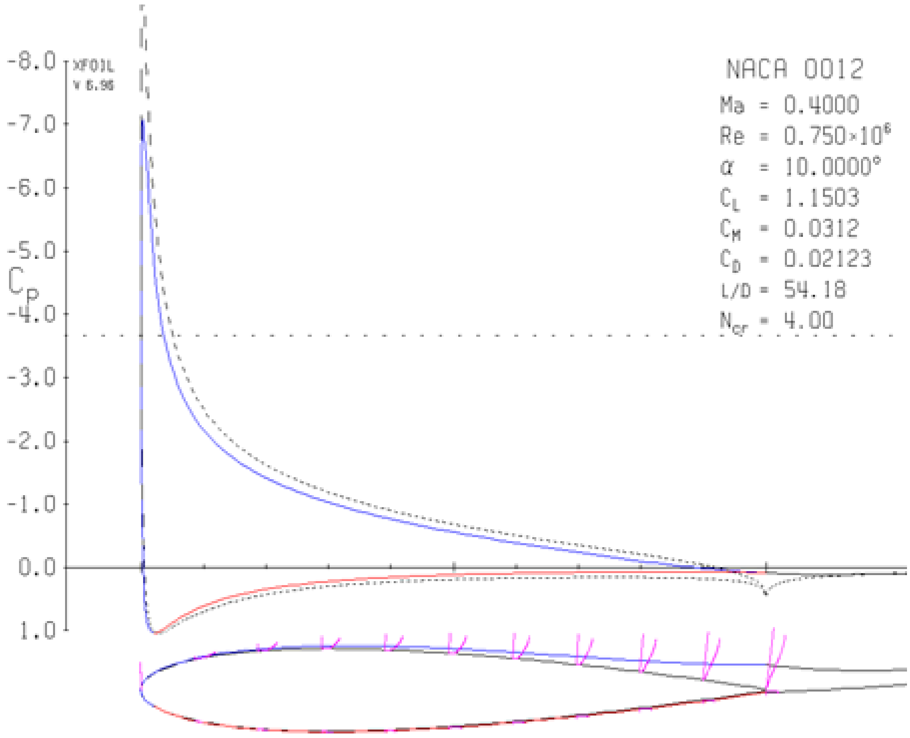

Figure 43 Cp Distribution of NACA 0012 at Mach 0.4 at 10 degrees Angle of Attack / XFOIL Computation

At 10 degrees of angle of attack, the flow shows mainly laminar behavior while the boundary layer thickness grows at the top surface of the airfoil which can be seen in Figure 43.

3.1.1.3. Solution at M= 0.4 and α=15° in XFOIL

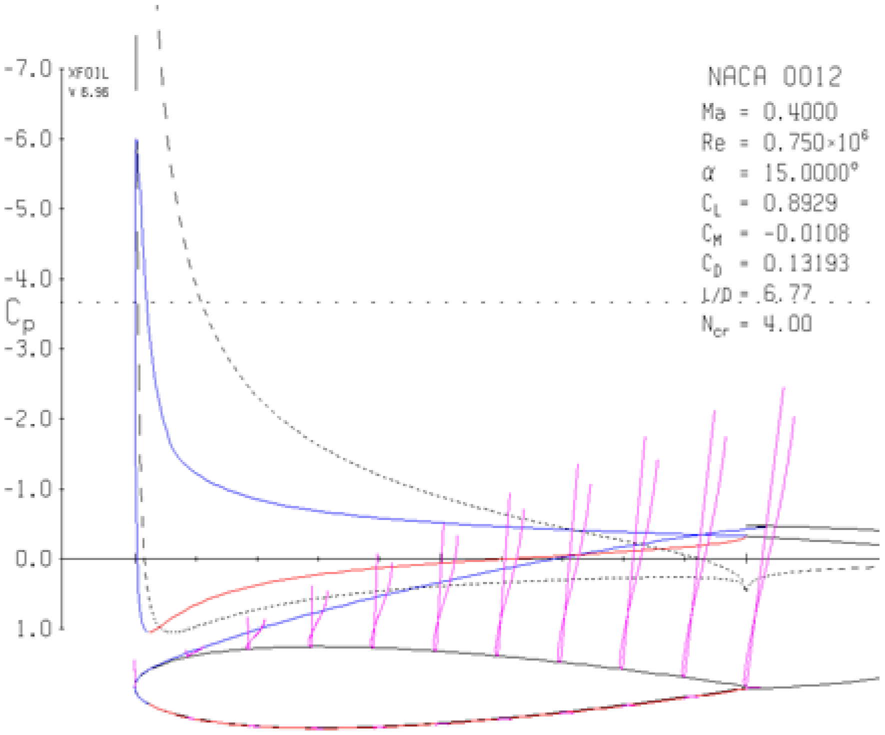

Figure 44 Cp Distribution of NACA 0012 at Mach 0.4 at 15 degrees Angle of Attack / XFOIL Computation

Around 15 degrees of angle of attack, viscous forces on the airfoil surface overcomes the inertial forces which thickens the boundary layer and causes flow separation. This can be observed by the boundary layer velocity profiles in Figure 44. The suction pressure drops drastically compared to the inviscid solution on the top surface of the airfoil which causes significant drop in the lift coefficient prior to stall.

3.1.1.4. Solution at M= 0.4 and α=20° in XFOIL

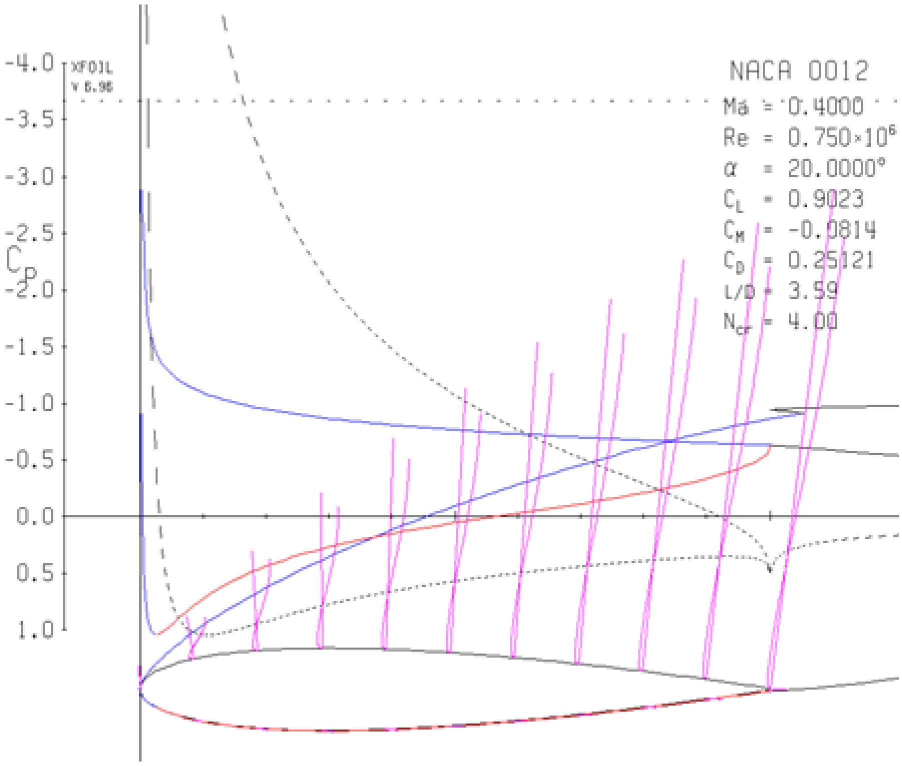

Figure 45 Cp Distribution of NACA 0012 at Mach 0.4 at 20 degrees Angle of Attack / XFOIL Computation

The transition occurs from the laminar flow to the turbulent flow. It starts with the formation of the separation bubble at the leading edge. Then, the separation bubble moves to trailing edge and sheds away. This behaviour is interpreted from the boundary layer velocity profiles around the airfoil at 20° angle of attack given in Figure 45.

3.1.1.5. Solution at M= 0.4 and α=5° in SU2

In Figures 46-50, the pressure distribution, the eddy viscosity distribution and the Mach distribution contours and the lift coefficient and the drag coefficient histories obtained by SU2 analyses are plotted. Field variables are obtained in steady analysis at 5° angle of attack and at Mach number 0.4.

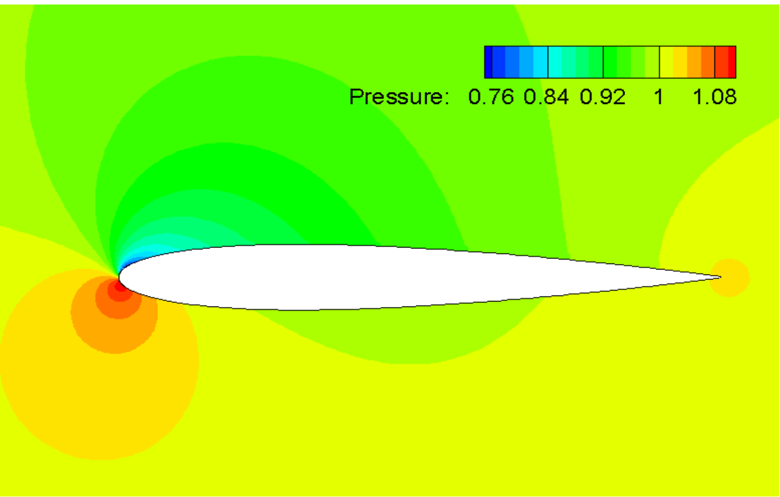

Figure 46 Pressure Distribution at Mach number 0.4 and Angle of Attack of 5° / SU2 Computation

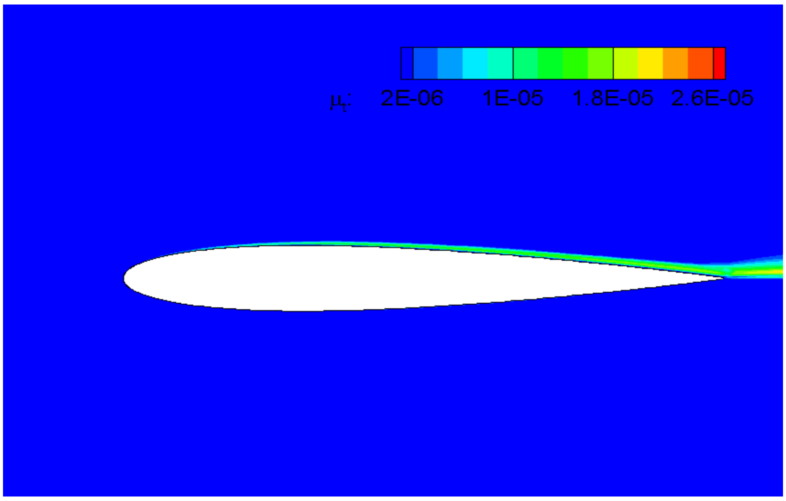

Figure 47 Turbulent Viscosity (μ_t) Distribution at Mach number 0.4 and Angle of Attack of 5° / SU2 Computation

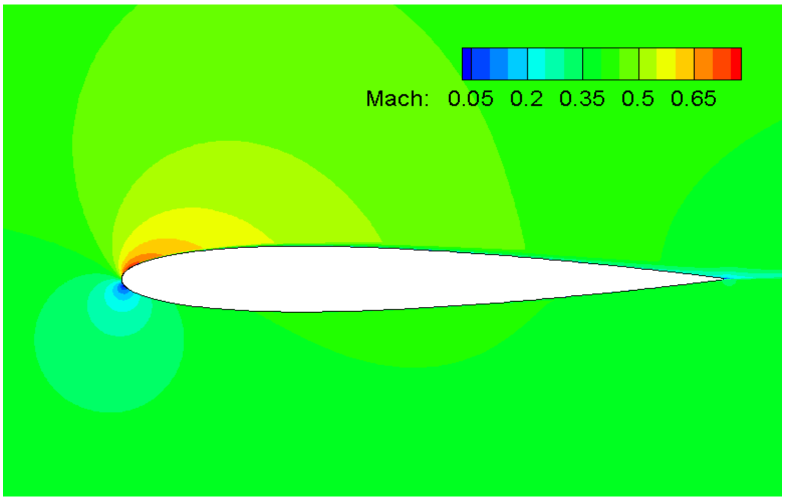

Figure 48 Mach Number Distribution at Mach number 0.4 and Angle of Attack of 5° / SU2 Computation

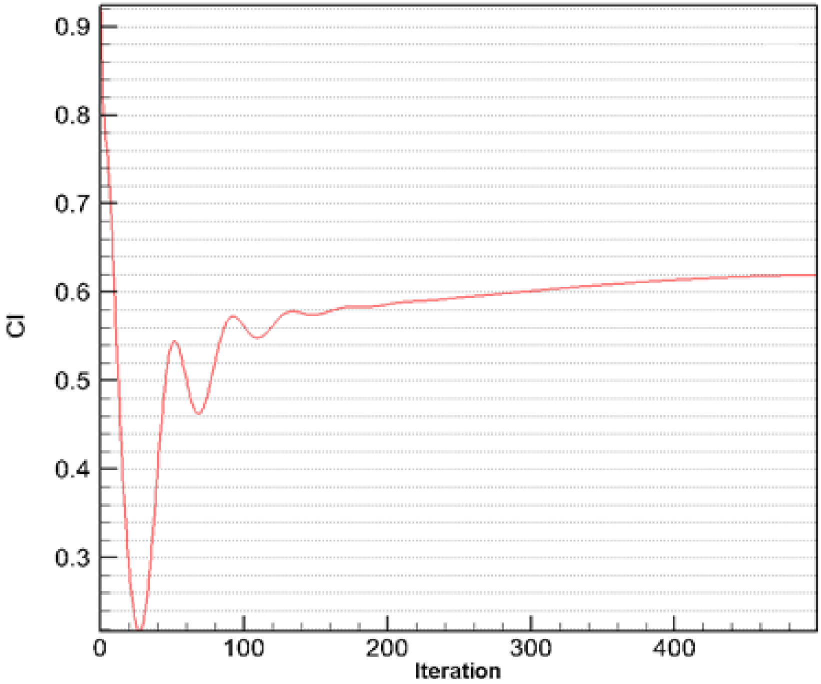

Figure 49 Cl at Mach number 0.4 and Angle of Attack of 5° / SU2 Computation

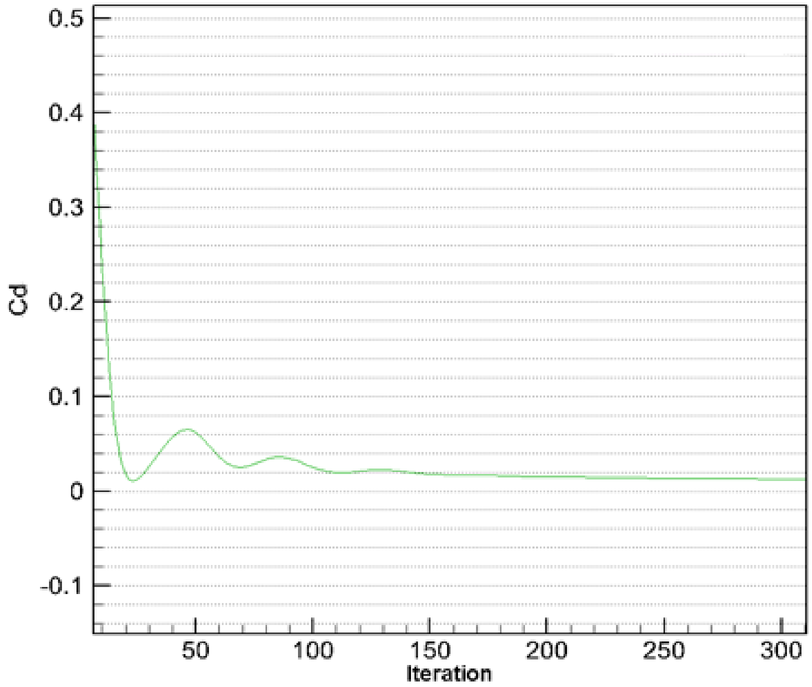

Figure 50 Cd at Mach number 0.4 and Angle of Attack of 5º / SU2 Computation

Cp distributions obtained from SU2 analyses at 0.4 Mach and 5º angle of attack for Reynolds numbers of 0.75 x 10^6 and 6.5 x 10^6 and from XFOIL analysis at Reynolds numbers of 0.75 x 10^6 are plotted in Figure 51.

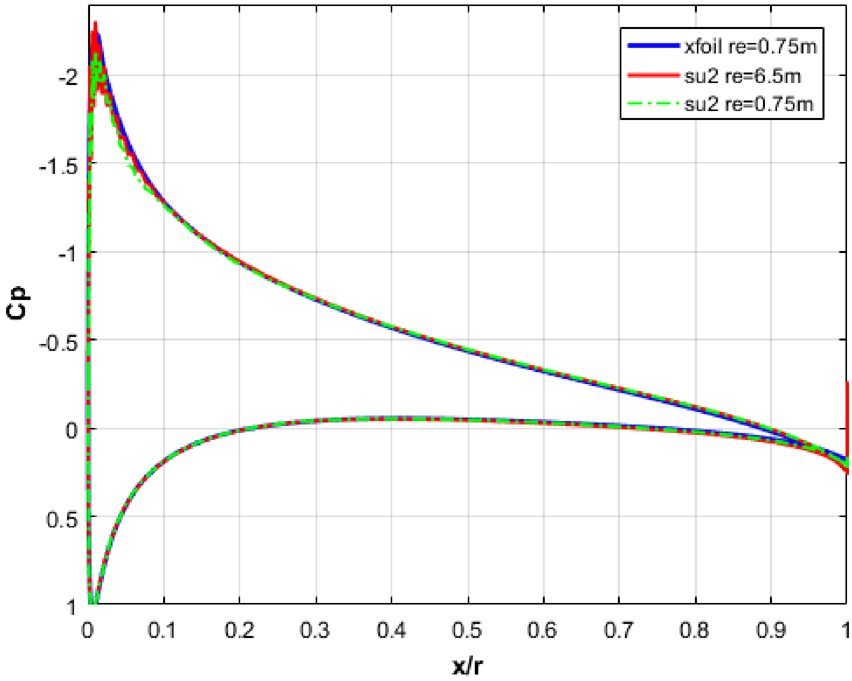

Figure 51 Cp Comparison Between XFOIL and SU2 at 5º Angle of Attack at M=0.4

3.1.1.6. Solution at M= 0.4 and α=10° in SU2

The field variables are given in Figures 52-54 for the steady analysis at the Mach number of 0.4 and the angle of attack of 10°.

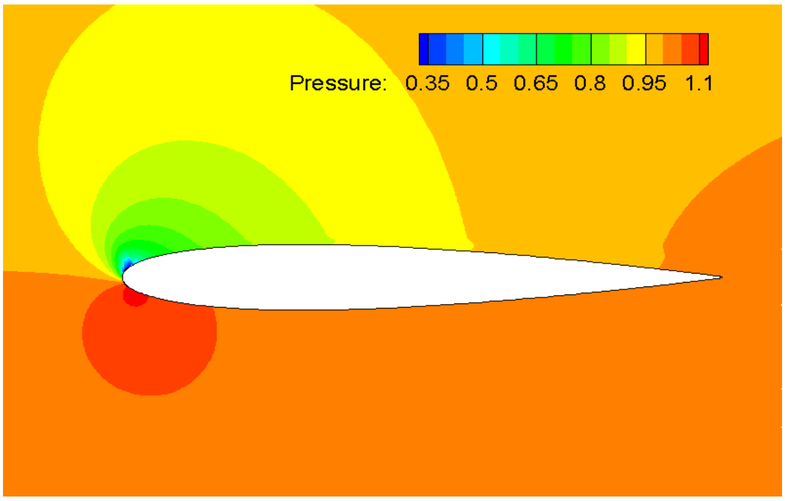

Figure 52 Pressure Distribution at Mach number 0.4 and Angle of Attack of 10° / SU2 Computation

The pressure distribution which is given in Figure 52 shows similar behavior with the analysis performed at the angle of attack of 5°. However, the analysis performed at 10 degrees angle of attack shows that the pressure contours on the upper surface closer to leading edge are more dispersive. Contour colors are different from the previous case because of the maximum and minimum limits of the color scaling of the plot.

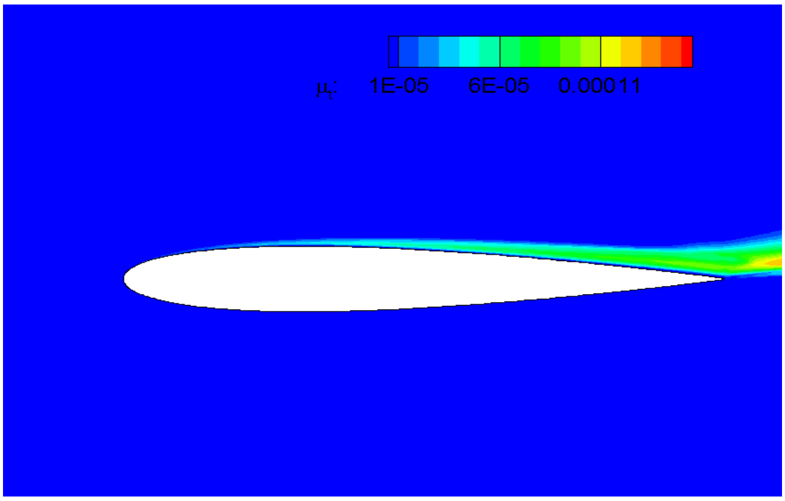

Figure 53 Turbulent Viscosity (μ_t) Distribution at Mach number 0.4 and Angle of Attack of 10° / SU2 Computation

The boundary layer is thicker for the analysis at the angle of attack of 10 degrees than the analysis at the angle of attack of 5 degrees. The boundary layer shows laminar behavior.

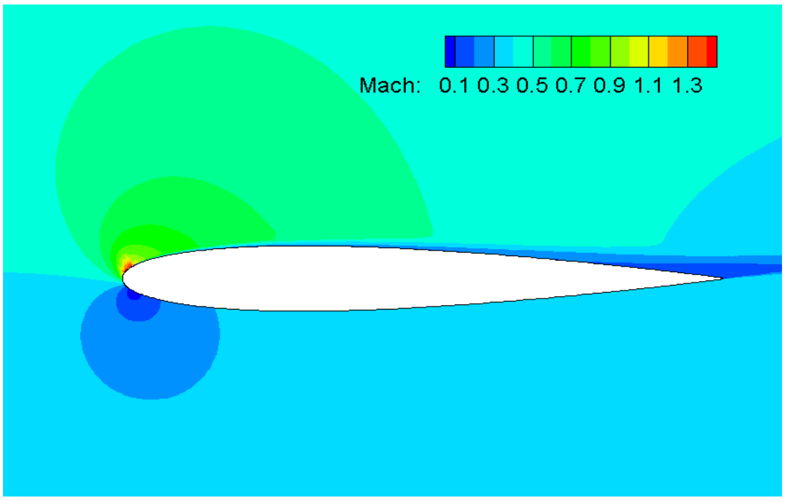

Figure 54 Mach Number Distribution at Mach number 0.4 and Angle of Attack of 10° / SU2 Computation

Figure 54 shows that the flow velocity is greater than the speed of sound in a smaller section at the leading edge. Figures 55 and 56 show the evolution of the lift and the drag coefficient with the iteration number.

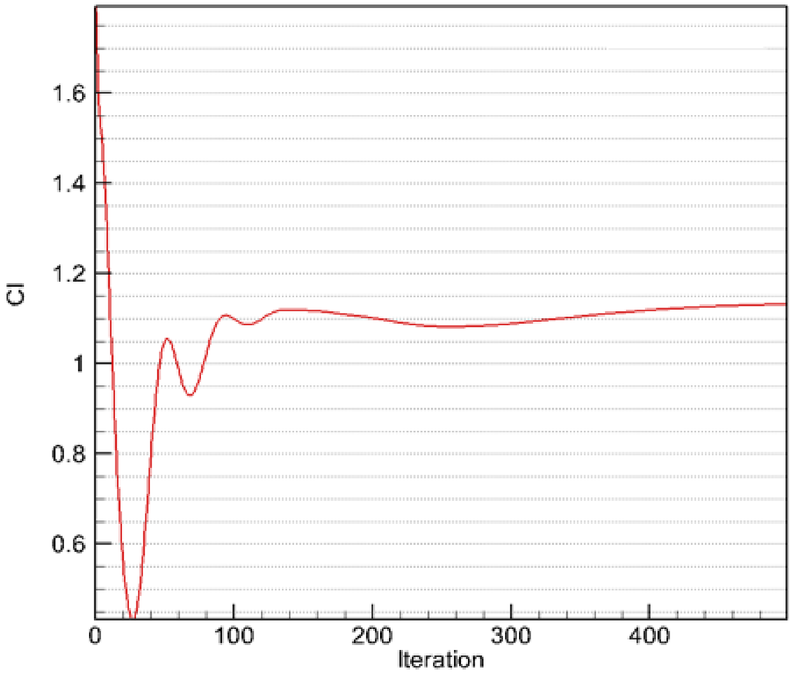

Figure 55 Cl at Mach number 0.4 and Angle of Attack of 10º / SU2 Computation

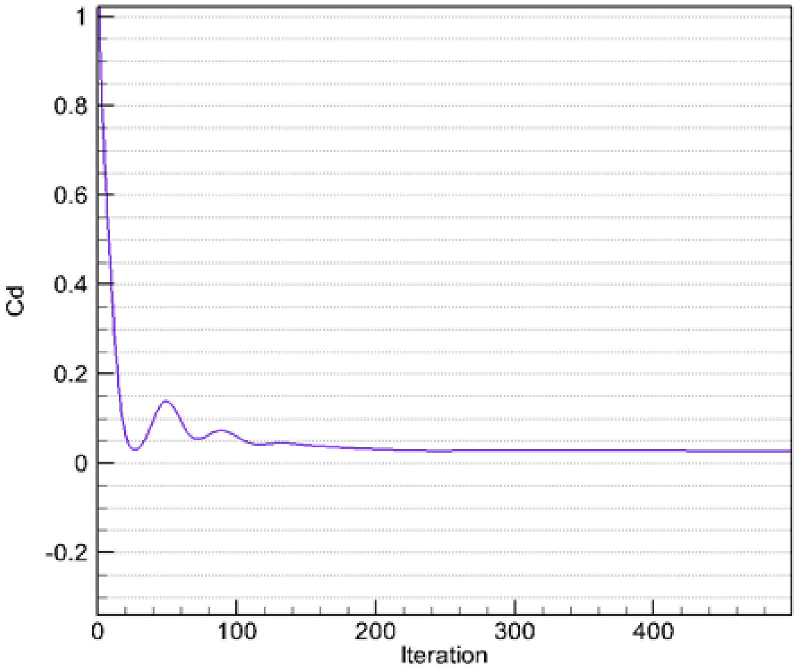

Figure 56 Cd at Mach number 0.4 and Angle of Attack of 10º / SU2 Computation

It can be seen from Figure 55 that more iterations are required to verify the convergence; however, drag coefficient is selected as the convergence criteria in the calculations and interpretations. Solution gets converged faster in 5^o angle of attack case than 10^o angle of attack case. It can be seen from steady behaviour of both cases in the same iteration period.

Cp distributions obtained from SU2 analyses at 0.4 Mach and 10^o angle of attack for Reynolds numbers of 0.75 x 10^6 and 6.5 x 10^6 and from XFOIL analysis at Reynolds numbers of 0.75 x 10^6 are plotted in Figure 57.

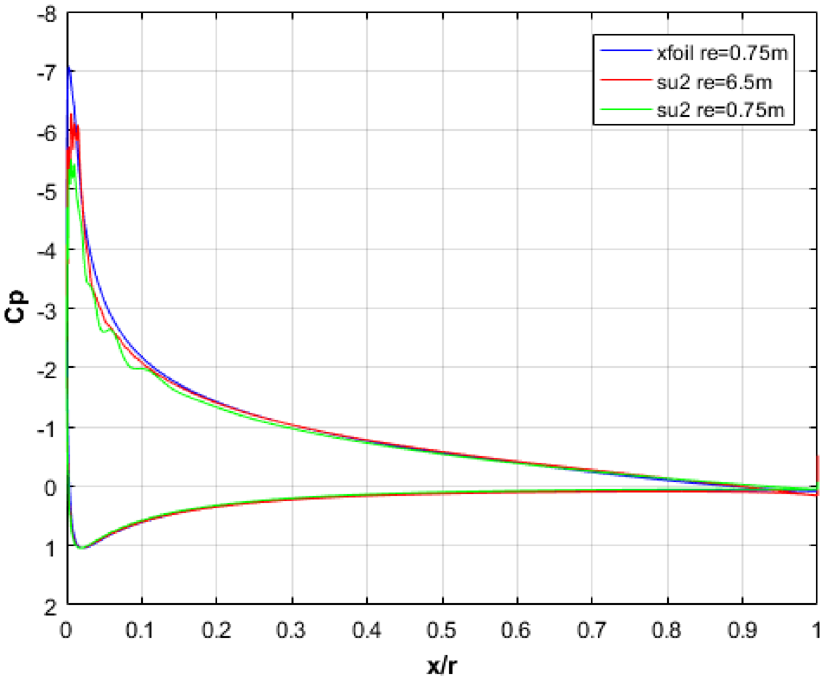

Figure 57 Cp Comparison Between XFOIL and SU2 at 10^o Angle of Attack at M=0.4

3.1.1.7. Solution at M= 0.4 and α=15^o in SU2

The transient analyses are performed for the conditions close to stall which may occur at high angle of attacks and at high Mach numbers. In this case, Mach number is selected as 0.4 and angle of attack is set to 15^o. Same grid is used in the transient analysis. This grid was prepared so that vortex shedding is properly observed and a steady solution can be obtained. For this reason, seed points on the airfoil surface are increased. The pressure distribution obtained as a result of the transient analysis is given in Figure 58 to illustrate the flow separation.

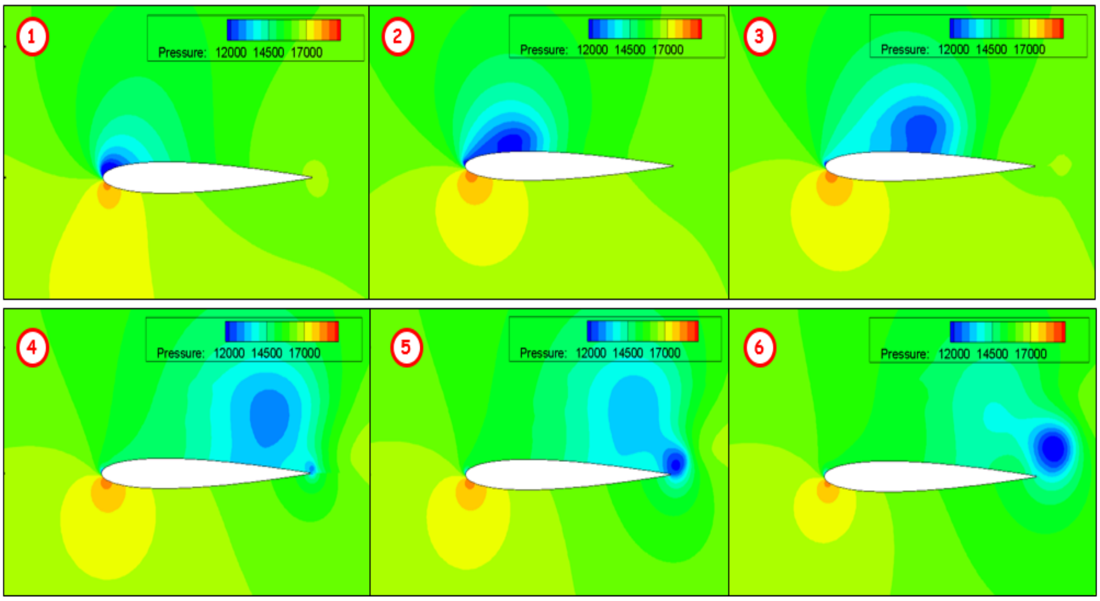

Figure 58 Pressure Distribution in Transient Analysis at Mach number 0.4 and Angle of Attack of 15º

In Figure 58, the formation of the separation bubble at the leading edge can be observed in the first steps. Then, this separation bubble moves on the top surface of the airfoil and it is shed away from the trailing edge. The eddy viscosity distribution is given in Figure 59.

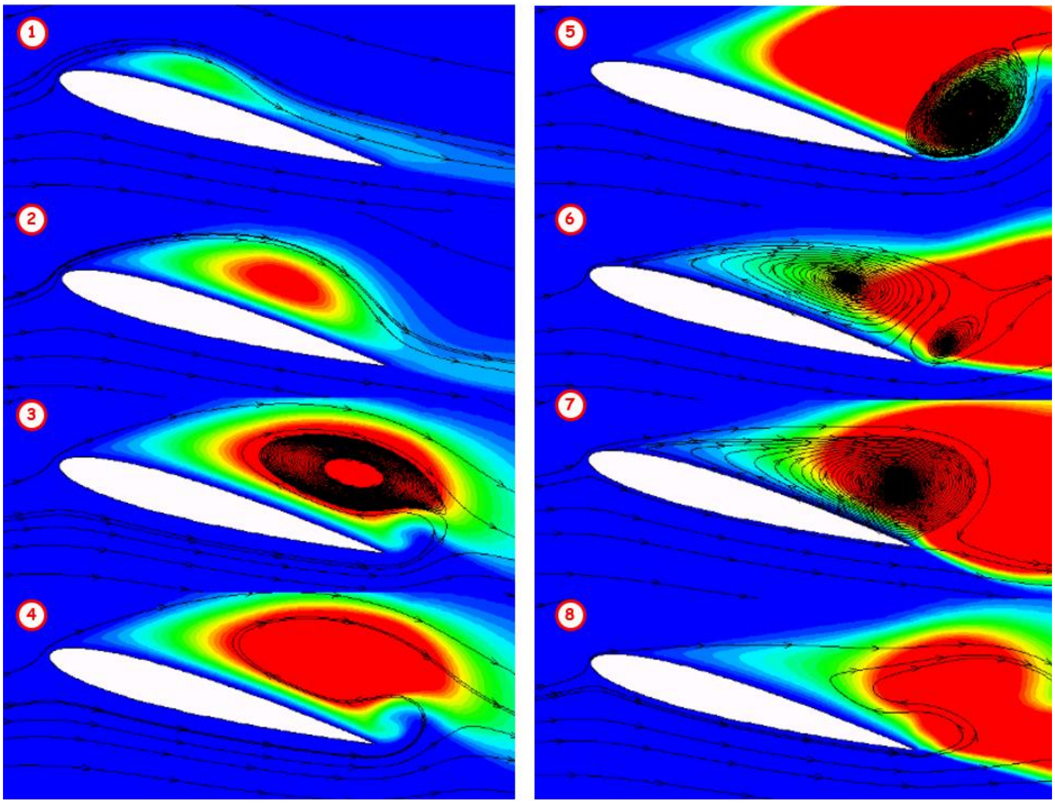

Figure 59 Turbulent Viscosity Distribution at Mach number 0.4 and Angle of Attack of 15º

Boundary layer velocity profiles at the beginning of the simulation are given in Figure 60 when the separation bubble is formed at the leading edge.

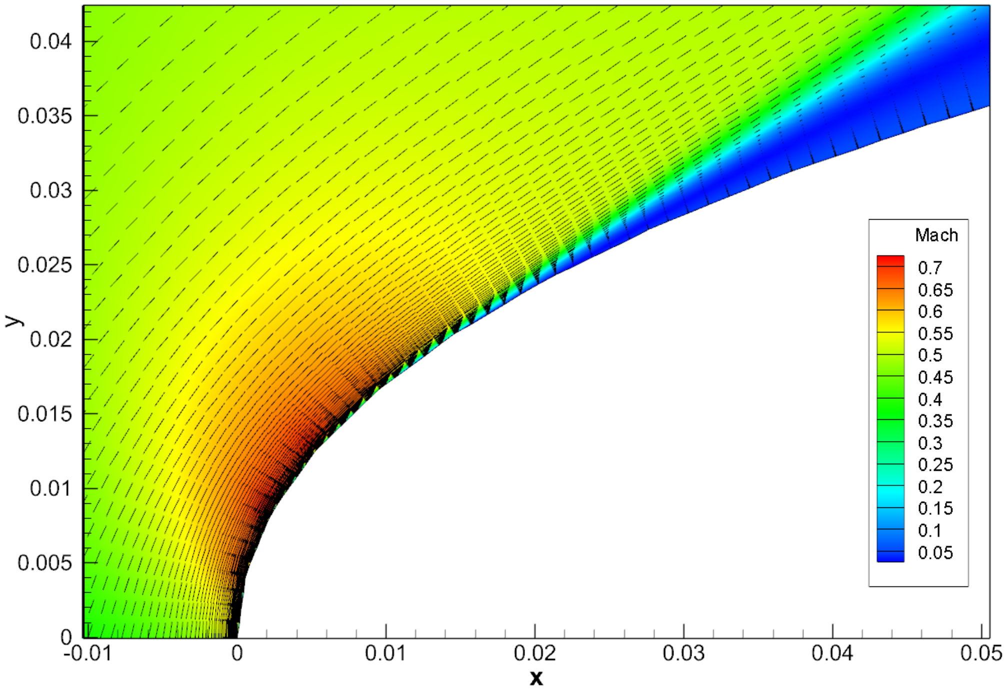

Figure 60 Mach Number Distribution and Boundary Layer Velocity Profiles at the beginning of Flow Separation at Mach number 0.4 and Angle of Attack of 15°

Figure 60 is taken from initial steps of the transient analysis performed at Mach 0.4 and 15° angle of attack. This figure is given to show the boundary layer velocity profiles before the flow separation. Mach number is less than 1 around the airfoil surface at the beginning of the transient analysis although Mach number is greater than 1 around the airfoil surface in the steady analysis performed at 10° angle of attack. This can be explained by that the flow is not steady at the beginning of the analysis. In the following time iterations, high velocity region moves toward the leading edge, shock formation is observed and Mach number gets values higher than 1. Transition point can be predicted from the boundary layer velocity profiles close to 0.02 chord.

In transient analysis, temporal integration is in dual-time stepping scheme. In this scheme, internal iterations are performed at each external time iteration. The lift and drag versus external time iteration curves obtained from the transient analysis at 0.4 Mach and 15° angle of attack are given in Figures 61 and 62.

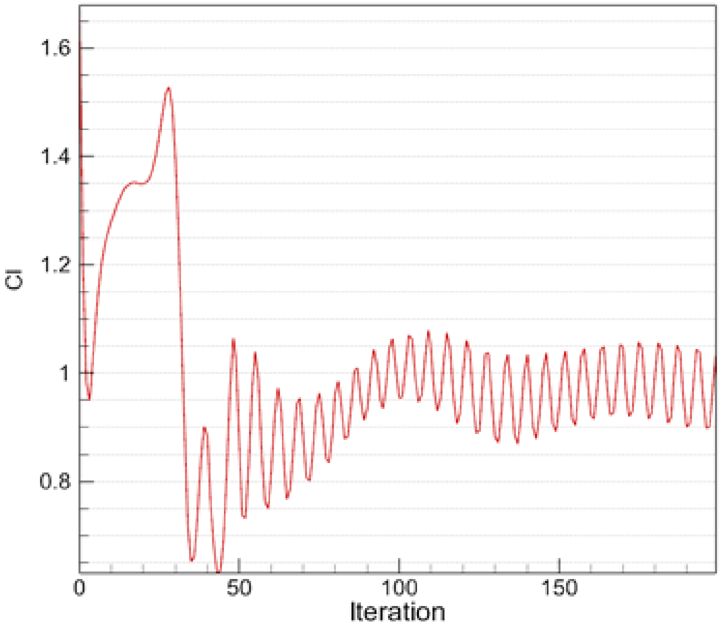

Figure 61 Cl in Transient Analysis in SU2 at Mach number 0.4 and Angle of Attack of 15^o

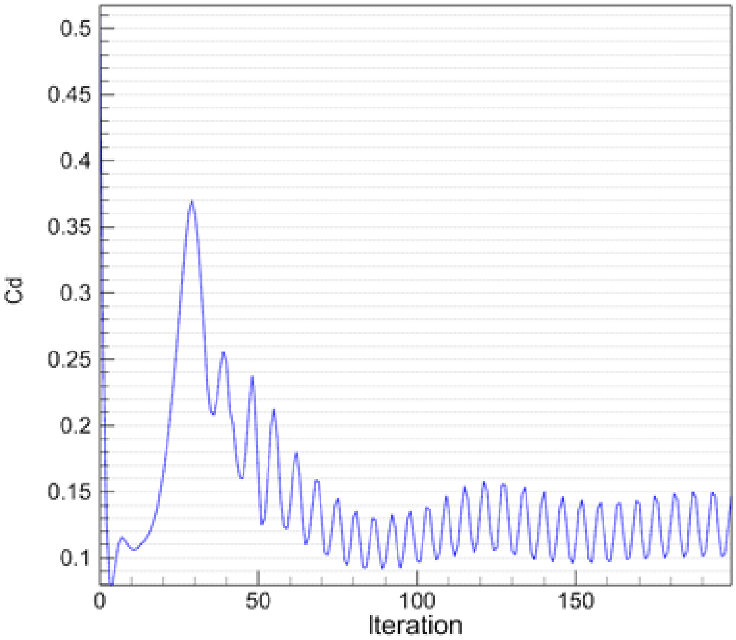

Figure 62 Cd in Transient Analysis in SU2 at Mach number 0.4 and Angle of Attack of 15^o

Last 5 oscillations from maximum peak to peak are taken to calculate the mean value of the lift, the drag and the moment coefficients in the transient analysis. It should be noted that a convergent oscillatory behavior is observed in the lift and the drag plots.

Periodic convergent oscillatory behavior can be seen from the residuals of conservative variables $(\rho, \rho u, \rho v)$ which are given in Figure 63.

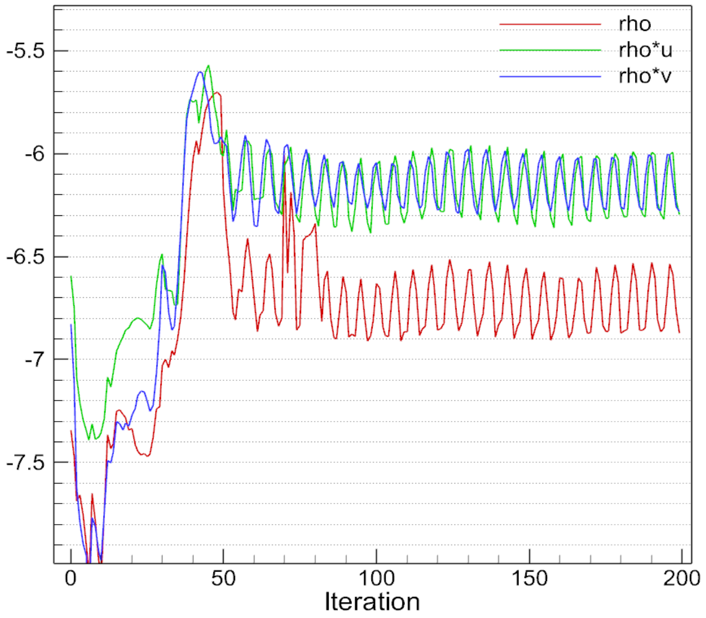

Figure 63 Residuals of Conservation Equations in Transient Analysis in SU2 at Mach number 0.4 and Angle of Attack of 15°

The residuals of variables in turbulence equations which are the turbulent kinetic energy (k) and the dissipation frequency (ω) are plotted in Figure 64.

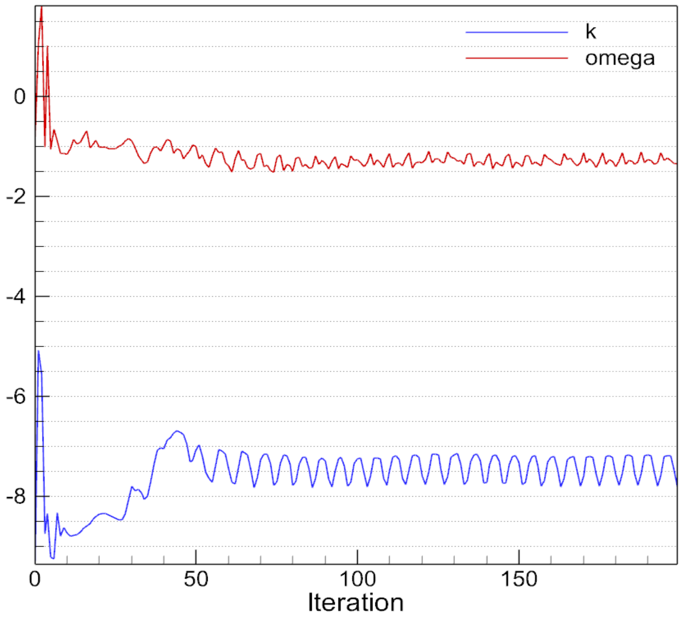

Figure 64 Residuals of Turbulence Equations in Transient Analysis in SU2 at Mach number 0.4 and Angle of Attack of 15°

3.1.2. SU2/XFOIL Simulations at Mach 0.7

The lift and the drag coefficient obtained by XFOIL and SU2 are compared with the aerodynamic performance table values for the NACA0012 profile in Figures 65 and 66 at Mach 0.7.

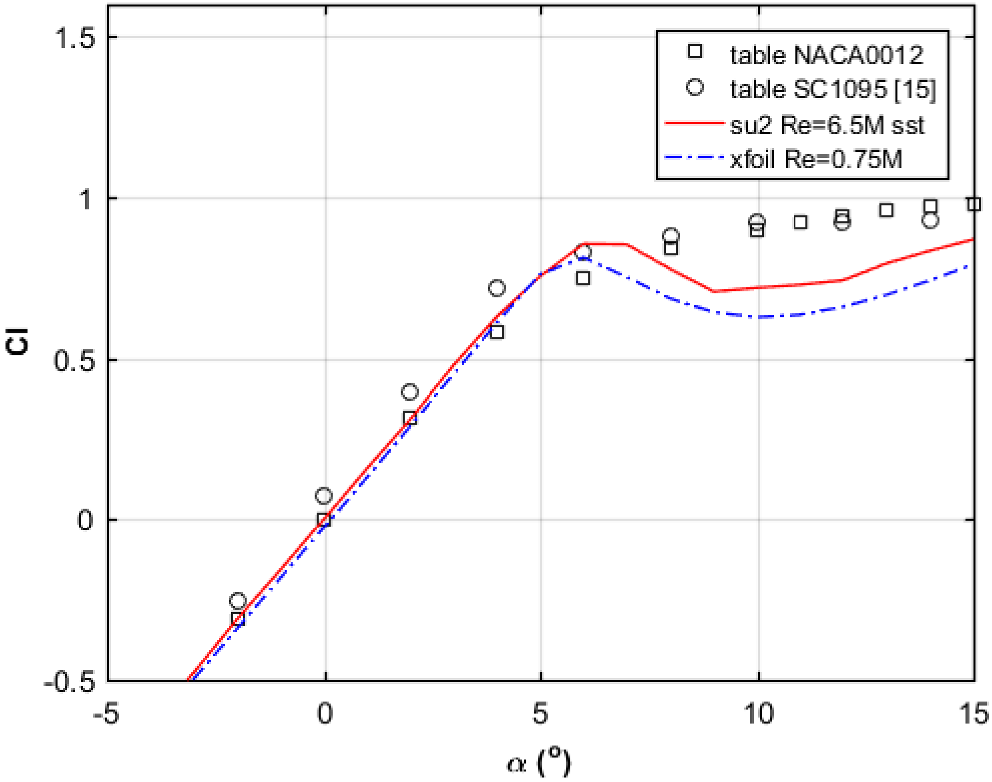

Figure 65 Cl Comparison of Angle of Attack Sweep at M=0.7 between XFOIL, SU2 and Aerodynamic Coefficients Lookup Table

Similar trends can be observed in the lift coefficient between XFOIL and SU2 results in Figure 65. The stall occurs at an angle of attack between 6-7 degrees which is smaller than the stall angle of attack which is predicted utilizing the lookup tables. Furthermore, as seen in Figure 65, the stall angle of attack may not be clearly determined utilizing the aerodynamic coefficient lookup tables. On the other hand, the second stall behavior can be observed in XFOIL-SU2 results. The maximum lift coefficient is higher in the lookup tables than the maximum lift coefficient obtained from the analyses performed in XFOIL and SU2.

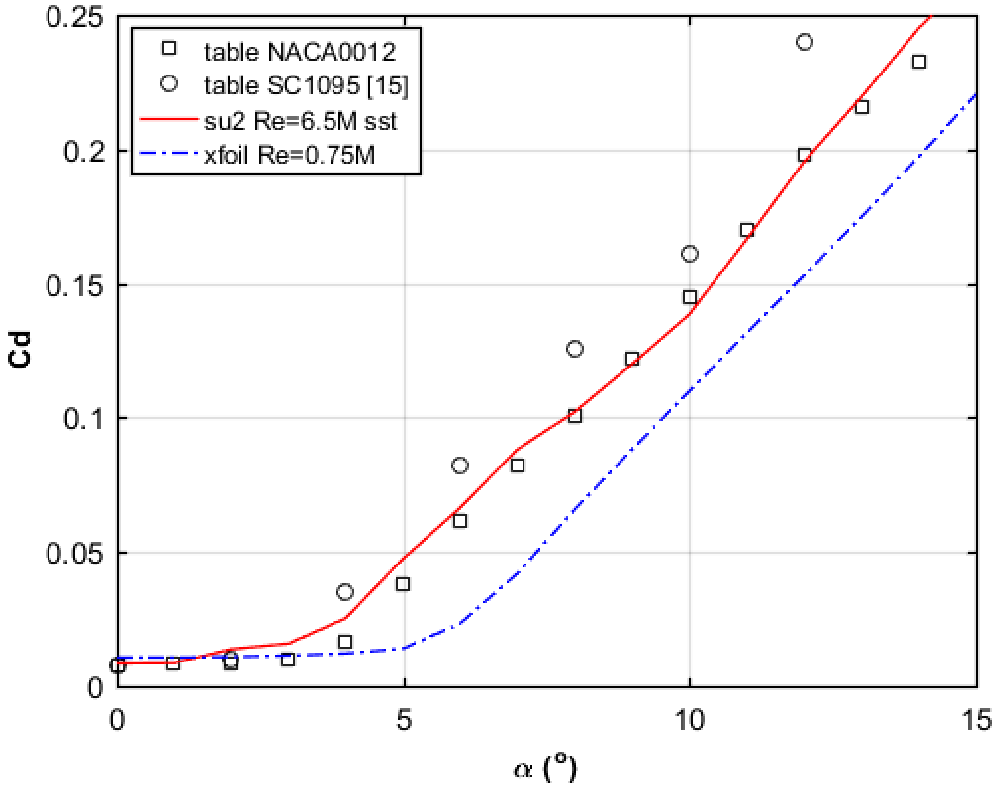

Figure 66 Cd Comparison of Angle of Attack Sweep at M=0.7 between XFOIL, SU2 and Aerodynamic Coefficients Lookup Table

Drag coefficients of read from the lookup table and the drag coefficients calculated from SU2 shows good agreement for the Mach number of 0.7. XFOIL has a delay in the drag divergence compared to the SU2 analysis and the performance table values. For the low angles of attack, XFOIL gives closer results to lookup table values while for the high angles of attack, SU2 gives closer results. It should also be noted that the lookup table values are dependent on the wind tunnel tests and some correction factors might have been applied on the test data. However, coefficients calculated from SU2 and XFOIL analyses are in similar trends with the table coefficients.

3.1.2.1. Solution at M= 0.7 and α=5° in SU2

The pressure distribution, the turbulent viscosity distribution, the Mach distribution around NACA0012 airfoil in the steady analysis which is performed at Mach number 0.7 and the angle of attack of 5° are given in Figures 67-69.

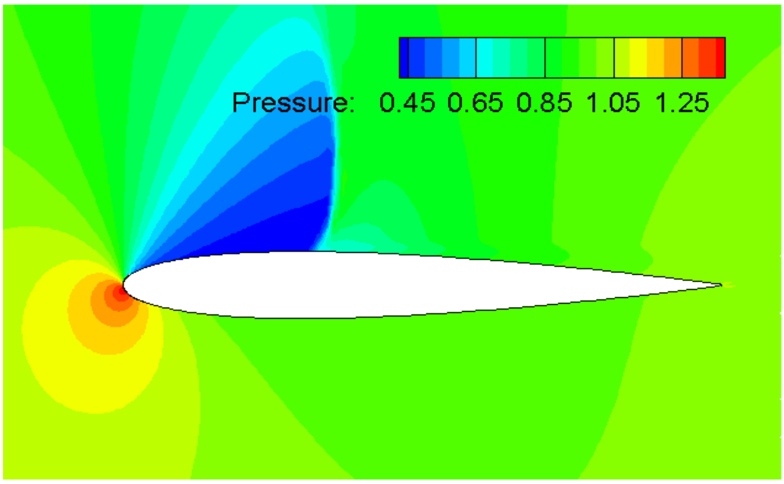

Figure 67 Pressure Distribution at Mach number 0.7 and Angle of Attack of 5° / SU2 Computation

Figure 67 shows the pressure distribution in SU2 analysis at Mach 0.7 and at 5° angle of attack. Shock formation at the leading edge can be observed from the pressure drop. Also, the stagnation point on the airfoil surface can be seen in Figure 67.

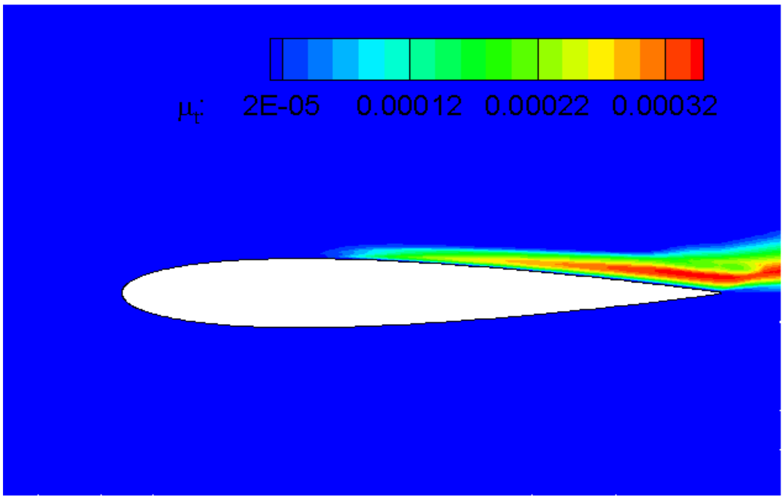

Figure 68 Turbulent Viscosity (μ_t) Distribution at Mach number 0.7 and Angle of Attack of 5° / SU2 Computation

In Figure 68, the boundary layer shows the the turbulent behavior which can be seen from the turbulent viscosity distribution and trailing edge vortex at the trailing edge.

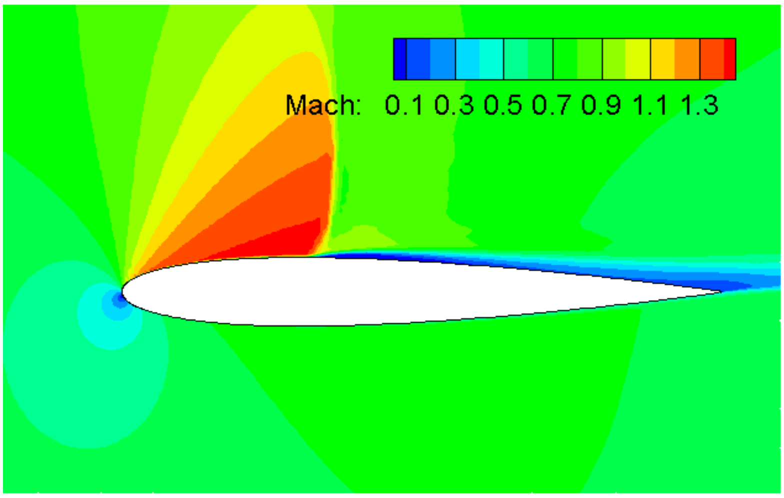

Figure 69 Mach Number Distribution at Mach number 0.7 and Angle of Attack of 5° / SU2 Computation

As seen from Figure 69, on the top surface of the airfoil, the velocity of the air becomes higher than the speed of sound close to the leading edge. In this region, an expansion wave and a normal shockwave is observed where the total pressure drops and the static pressure increases. The stagnation point is at the lower side of the leading edge. In the boundary layer in Figure 69, the velocity close to the airfoil surface is in the reverse direction with the oncoming flow in the boundary layer which is plotted by blue contours. Therefore, Mach number is lower close to the airfoil surface in Figure 69.

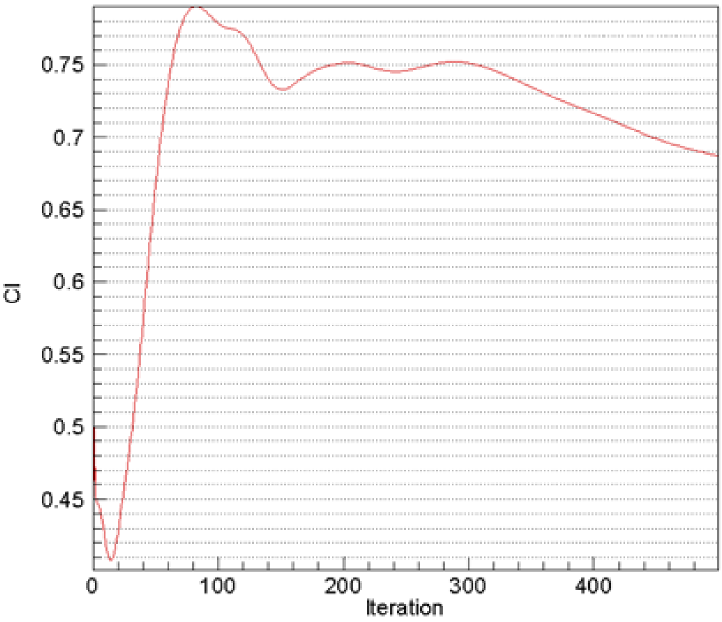

Figure 70 Cl at Mach number 0.7 and Angle of Attack of 5°/ SU2 Computation

After obtaining the convergent behavior in Figure 70, the solution gets diverged because of the instability which may be caused by a shock or the multigrid acceleration. However, steady data between iterations 200 and 300 are taken for the lift coefficient calculation in Figure 70.

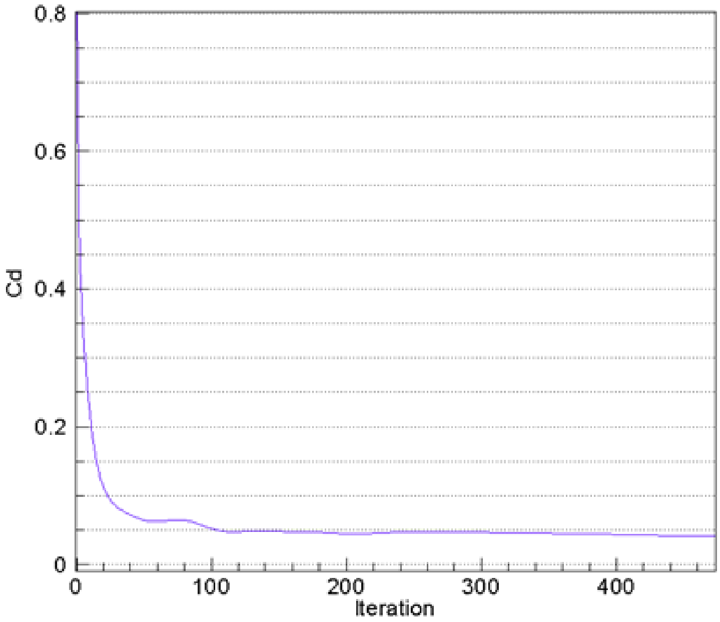

Figure 71 Cd at Mach number 0.7 and Angle of Attack of 5°/ SU2 Computation

In Figure 71, the drag coefficient obtained from SU2 analysis at Mach 0.7 and 5^{o} angle of attack is plotted. It is seen that the drag coefficient converges after 100 iterations.

3.2. XFOIL/SU2-Dymore Coupled Simulations

After having validated flow solver parameters by sectional analyses with table data, first XFOIL-Dymore and then SU2-Dymore coupled analyses are performed. First, a coupled analysis is performed in XFOIL. XFOIL may not give reasonable results at high angles of attack after 0.4 Mach number. Therefore, no collective input is given to the rotor in the first case. In the second case, first case is repeated with SU2 and compared with both the XFOIL solution and the internal aerodynamic solution. In the final case, collective input is given to the rotor in SU2 coupled program.

3.2.1. XFOIL-Dymore Coupled Solution at Zero Collective Input

In this section, blade angles, rotor aerodynamic loads, the sectional angle of attack and the Mach number values obtained from the Dymore-XFOIL coupled simulation with no control input are presented. For the coupled XFOIL-Dymore simulations, 20 aerodynamic stations along the blade span are considered in the computations since the coupling with XFOIL is computationaly not demanding. The comparisons are made at two different azimuths, however for the periodic hover case there is little dependence on the azimuth.

In Figure 72, the angle of attack distribution and the Mach number distribution at the aerodynamic computation points along the blade span can be seen when the rotor rotation is performed by prescribing zero control input to the swashplate. This proves that the angle of attack is only dependent on the blade twist angle for this case. Also, no farfield velocity is prescribed. The velocity at each aerodynamic node is basically the tangential velocity due to the rotation. The maximum angle of attack and the maximum Mach number which the aerodynamic stations are subjected to are about 10 degrees and 0.65 respectively.

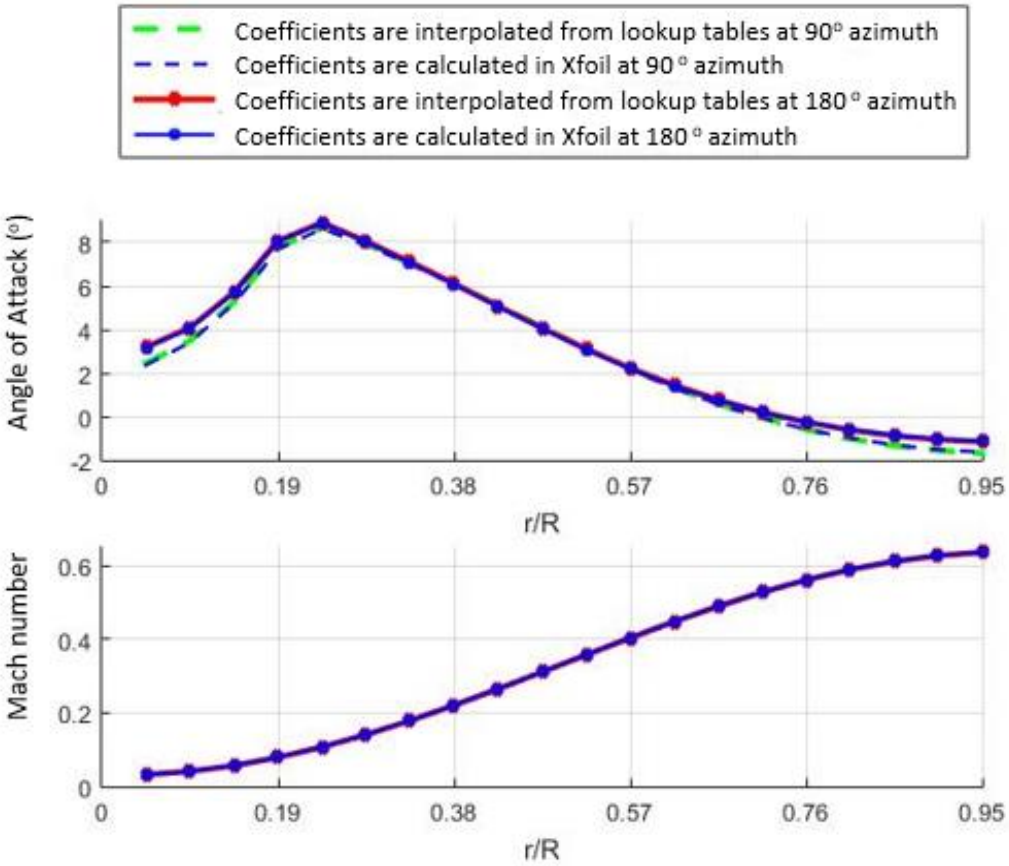

Figure 72 Angle of Attack and Mach Values at Blade Aerodynamic Stations in Dymore-XFOIL Coupled Simulation

Figure 73 compares the local lift, drag and moment coefficients along the blade span. In the aerodynamic performance tables, the moment coefficients are taken as zero which can be seen in table 3 of Appendix A. The moment coefficients obtained from XFOIL analyses are also very close to zero, but at the radial stations between r/R=0.19 and r/R=0.38 trends of the moment coefficient shows that divergence has occurred in XFOIL analyses.

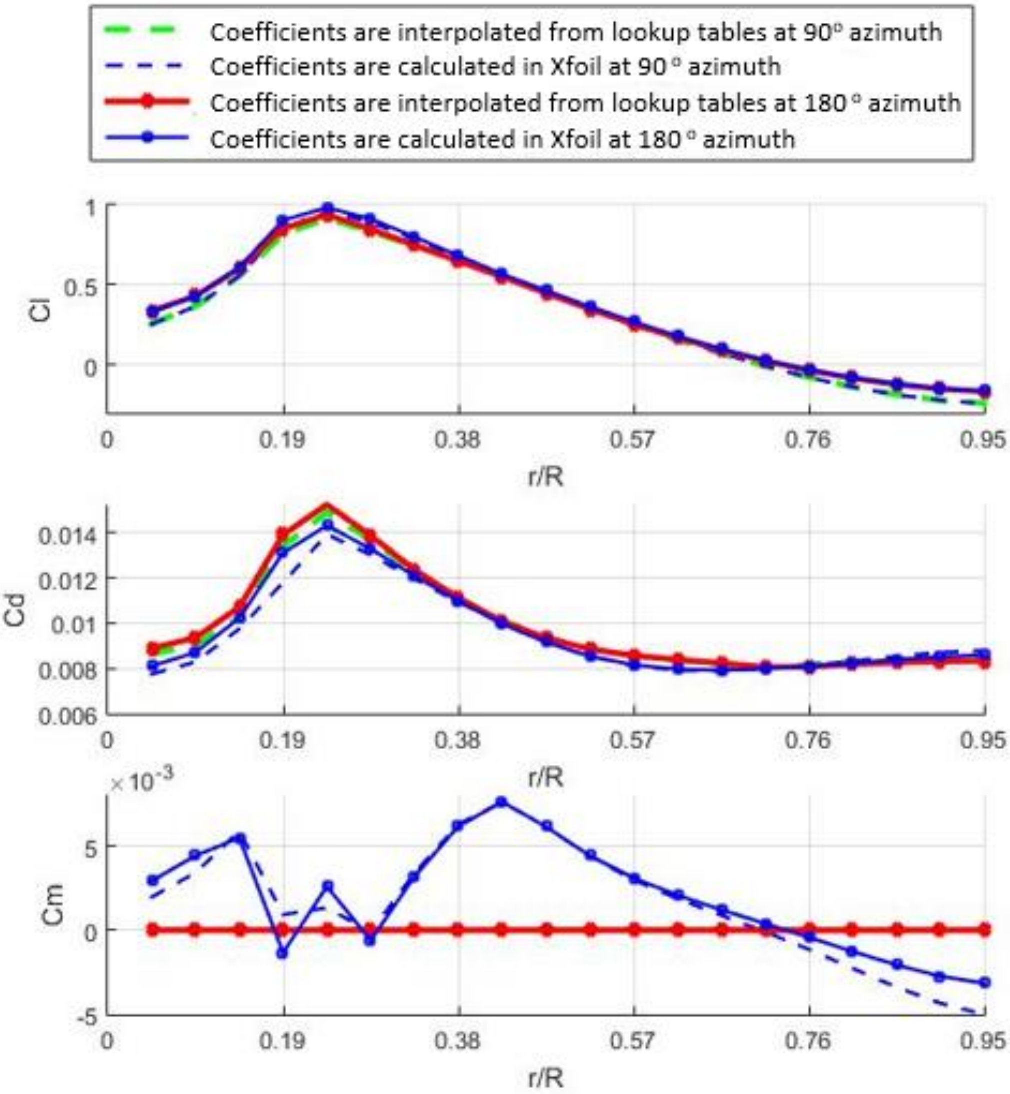

Figure 73 Lift, Drag, Moment Coefficients at Blade Aerodynamic Stations in Dymore-XFOIL Coupled Simulation

In Figure 74, flap, lead-lag and feathering angles are given at the start of the simulation for a period of 4 rotations. Initially, the dynamic response do not show periodic oscillatory settled behavior. After a few more rotations periodic oscillations will be observed with respect to the flap and the lead-lag frequencies (flapwise and chordwise frequencies) given in Table 12. Furthermore, a reasonable input value to swashplate is good to prove the realistic behavior of the rotor. On the other hand, only purpose here is to simply compare the XFOIL coupled solution with the lookup table solution for low angles of attack. As understood from this part, the dynamic behavior of the blades are similar in both solutions.

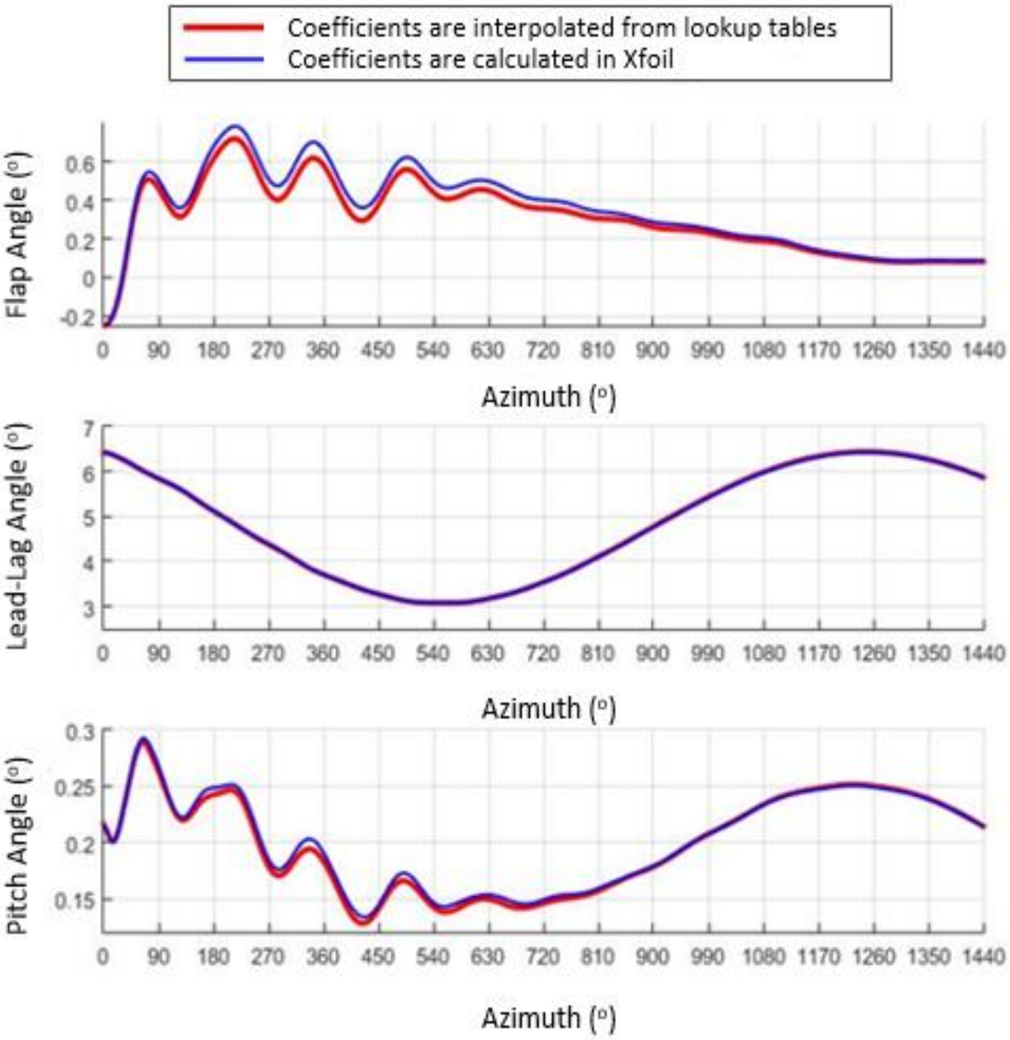

Figure 74 Rotor Blade Angles Calculated by Coupled Dymore-XFOIL Simulations

In Figure 75, thrust, torque, roll moment, pitching moment and lateral forces due to the aerodynamic forces and moments are given at the hub center. Results are given for one blade. Except for the torque values, all other data seem to be compatible with the lookup table results. The thrust values calculated by coupled XFOIL-Dymore is a little higher than the thrust values obtained with the lookup table solutions. The difference in torque is due to lower drag coefficient prediction in XFOIL which occurred at high angles of attack. In summary, the hub in-plane forces calculated by coupled XFOIL-Dymore simulations are lower than the forces calculated from the lookup tables while for the hub out-of-plane forces this condition is reversed.

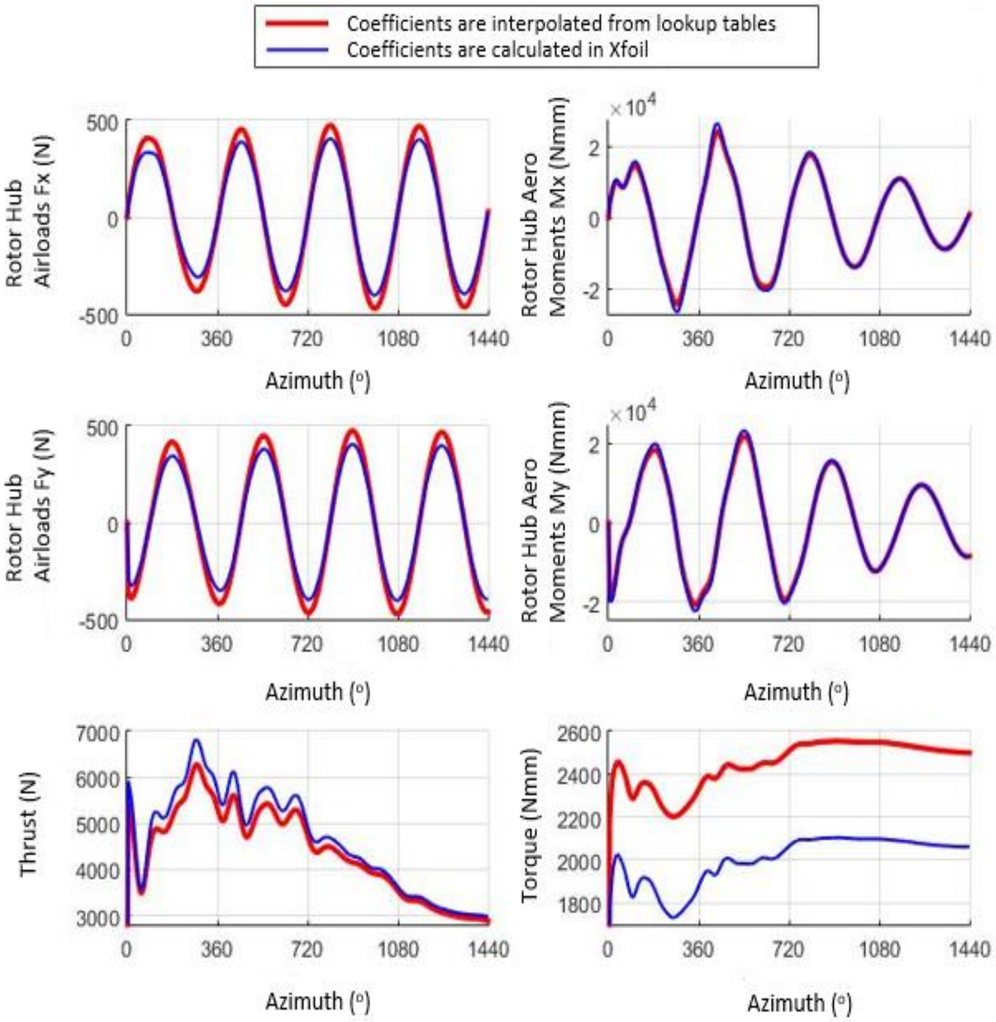

Figure 75 Rotor Hub Airloads Calculated by Coupled Dymore-XFOIL Simulations

3.2.2. SU2-Dymore Coupled Solution at Zero Collective Input

In this section, the blade angles and the rotor aerodynamic loads obtained from the Dymore-SU2 coupled simulation with no control input are presented on top of the previous computation performed with the Dymore-XFOIL coupled simulation to compare the SU2 coupled simulation with the XFOIL coupled simulation.

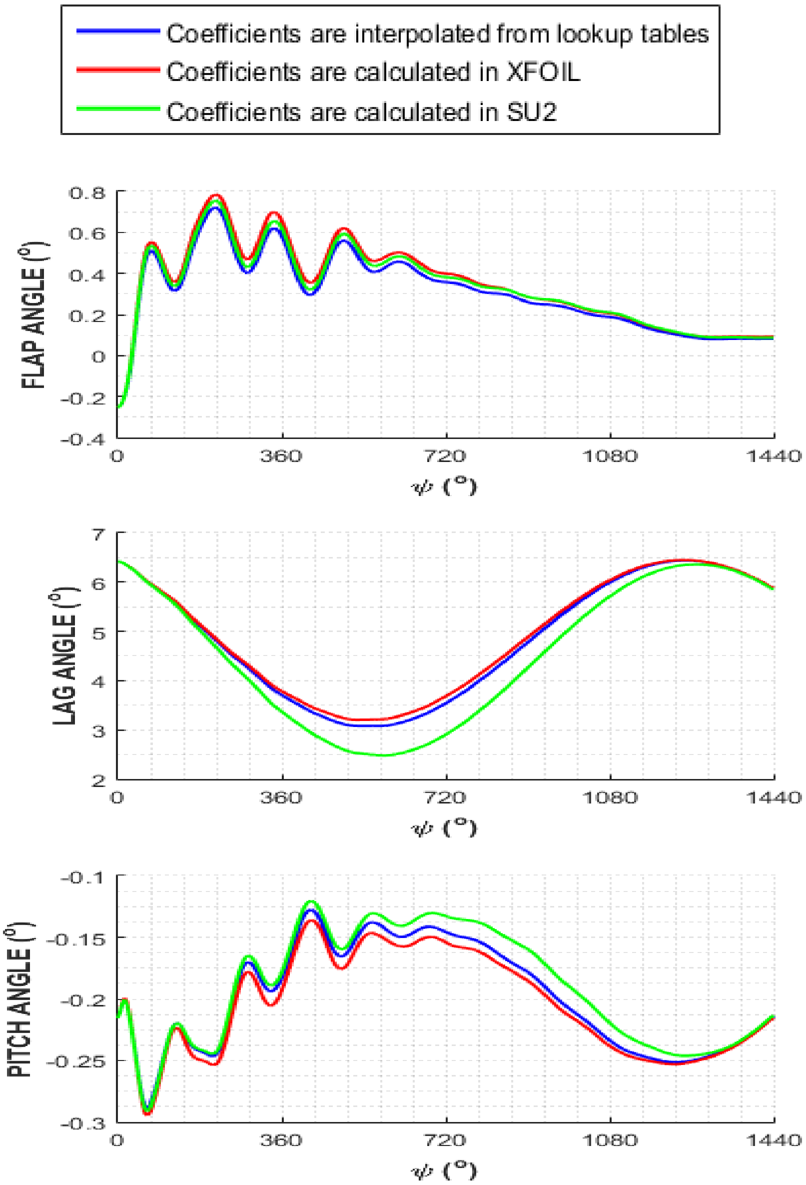

Figure 76 Rotor Blade Angles for Dymore-XFOIL/SU2 Coupled Simulation for Zero Collective Input

In Figure 76, flap, lead-lag and feathering angles are given at the start of the simulation for a period of 4 rotations. Flap, pitch and lag angles are in close agreement in both XFOIL and SU2 coupled simulations with the simulations performed using the lookup tables. The lag angles calculated from the SU2 coupled simulations came out to be less than the values found in the XFOIL coupled simulations and the lag angles calculated using the lookup table. The reason for this difference is that as in seen in Figure 41, the drag coefficient prediction of SU2 is higher than the drag coefficients available in the lookup tables or the prediction of XFOIL coupled simulations at low angles of attack. Therefore, it can be inferred that the lead-lag angle is strongly governed by the drag coefficient for the hover case. Similarly, the flap angle is mainly governed by the lift coefficient. Figure 76 shows that SU2-Dymore coupled simulation gives closer lift coefficient results to the table lookup values compared to the lift coefficients predicted by XFOIL-Dymore coupled simulations. Again, Figure 40 shows that lift coefficient prediction is better in SU2-Dymore coupled simulations than the XFOIL-Dymore coupled simulations at low angles of attack.

It should also be noted that when the rotation axes of the blade are not orthogonal to each other, the pitch input given to the blade kinematically creates a lag motion or a flap motion. This is known as the pitch lag coupling or the pitch flap coupling respectively which is mainly caused by the eccentricity between the rotation center and input location. Rotor model used in this thesis has kinematic couplings. Therefore, pitch angle is affected also by the lag angle and the flap angle.

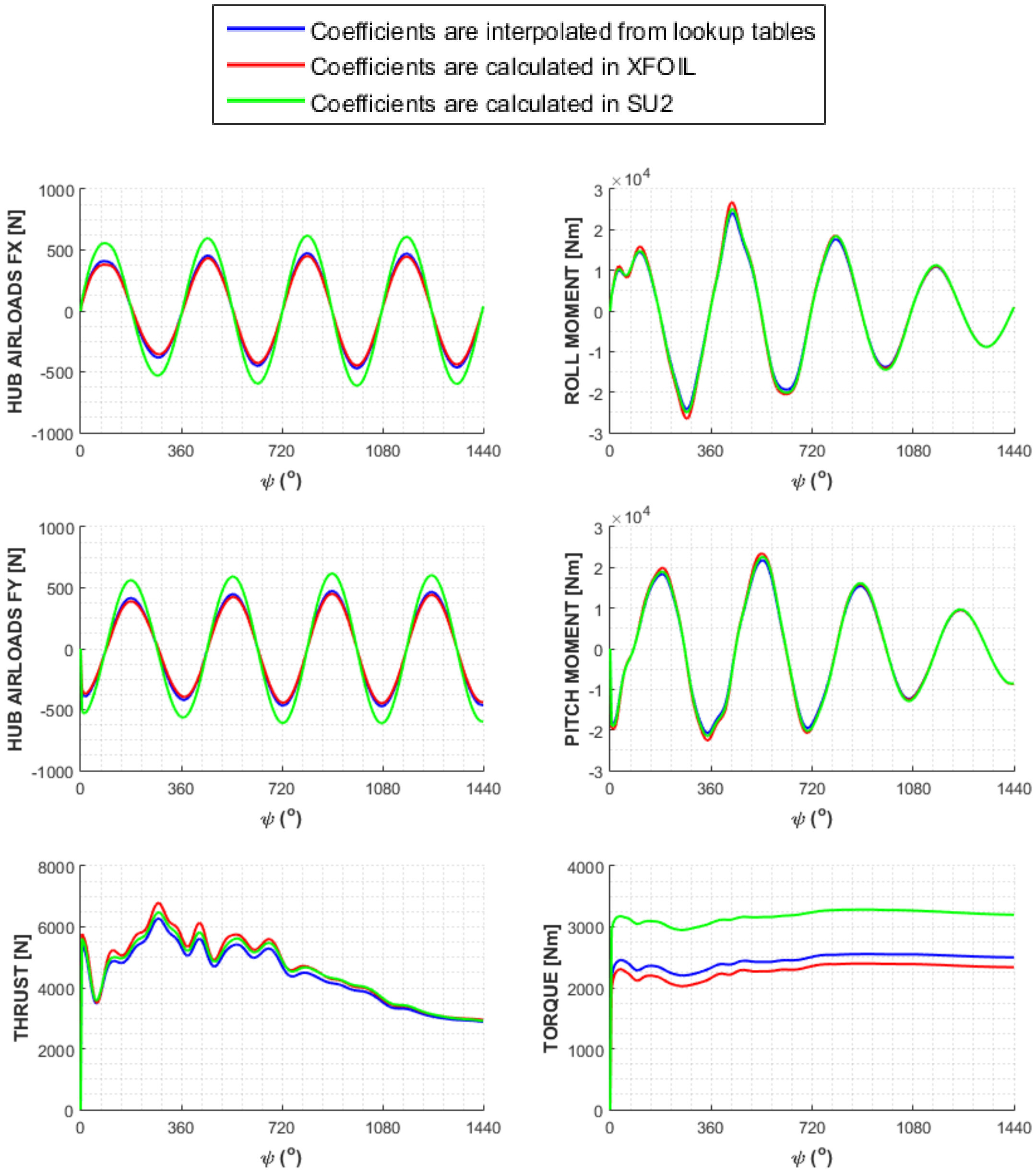

Figure 77 Rotor Hub Airloads for Dymore-XFOIL/SU2 Coupled Simulation for Zero Collective Input

Figure 77 gives the rotor hub airloads obtained by Dymore-XFOIL/SU2 coupled simulations for zero collective input. Thrust value is predicted better in the SU2 coupled simulation which is related to closer lift coefficient prediction at low angles of attack as seen in Figure 40. The torque value is predicted %23 higher in the SU2 coupled simulation with respect to the performance tables and the XFOIL coupled simulation at low angles of attack. This is again due to higher drag coefficient prediction in the SU2 coupled simulation which is seen in Figure 41. Higher drag coefficients obtained from SU2 are more reliable over the XFOIL results since Navier-Stokes analyses are performed bettter in compressible viscous flows rather than panel methods. XFOIL predicts the coefficients closer to the table values. However, the method used in the generation of baseline lookup table is not clearly known. To sum up, the hub-in-plane forces and the torque are mainly governed by the drag coefficient while the hub-out-of-plane forces are mainly governed by the lift coefficient.

3.2.3. Coupled SU2-Dymore Solution at 50mm Collective Input

In this section, the blade angles and the rotor aerodynamic loads obtained from the Dymore-SU2 coupled simulation with the collective input are presented. In this case, the flow comes to the sections in high angle of attack (~18^o) which can be approximately calculated by adding the pitch angle given (~8^o) in Figure 78 to the blade twist angle (~10^o) given in Figure 25. Since it is hard to obtain solution for these angles of attack in XFOIL, coupled XFOIL-Dymore simulations could not be performed for a given collective input of 50 mm.

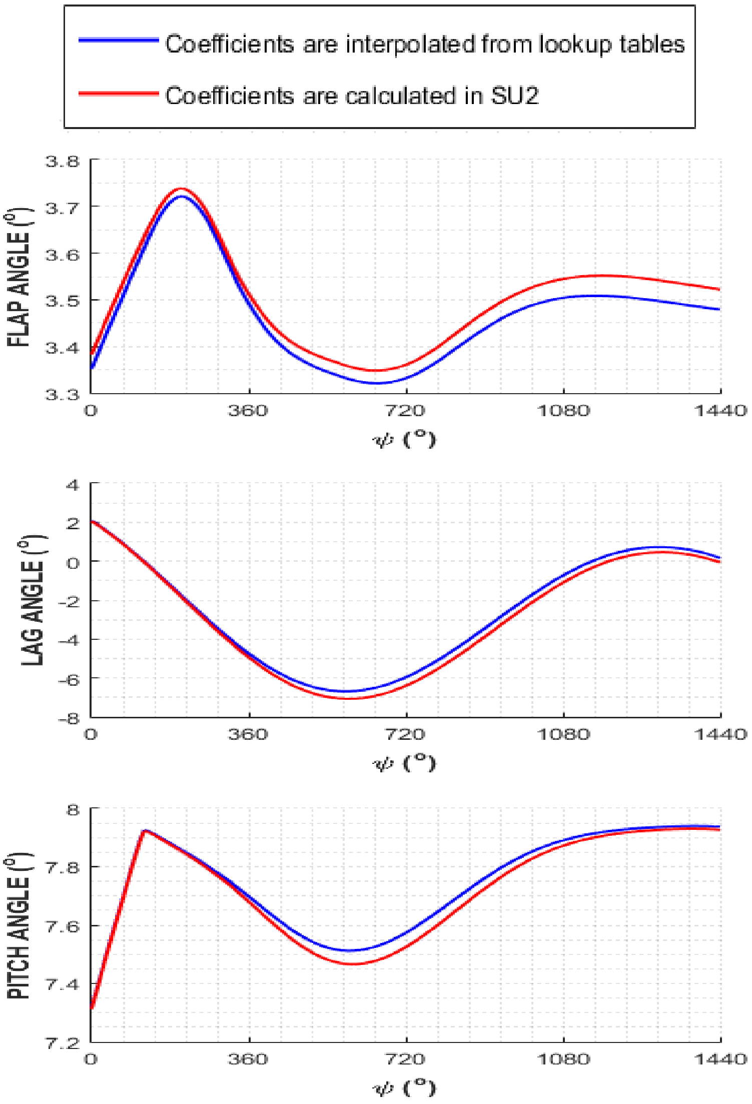

Figure 78 Rotor Blade Angles for Dymore-SU2 Coupled Simulation for 50mm Collective Input

In Figure 78, flap, lead-lag and feathering angles are given when 50 mm collective input is given as the vertical displacement at the swashplate. It is shown that the pitch angle is in compliance with the flap angle since only the collective input is considered. If the cyclic input were given, a phase difference of approximately 90^{o} should be expected between the pitch input and the flap angle. The blade angles calculated by the coupled SU2-Dymore simulations are in close correlation with the corresponding angles determined using the lookup table in the simulations.

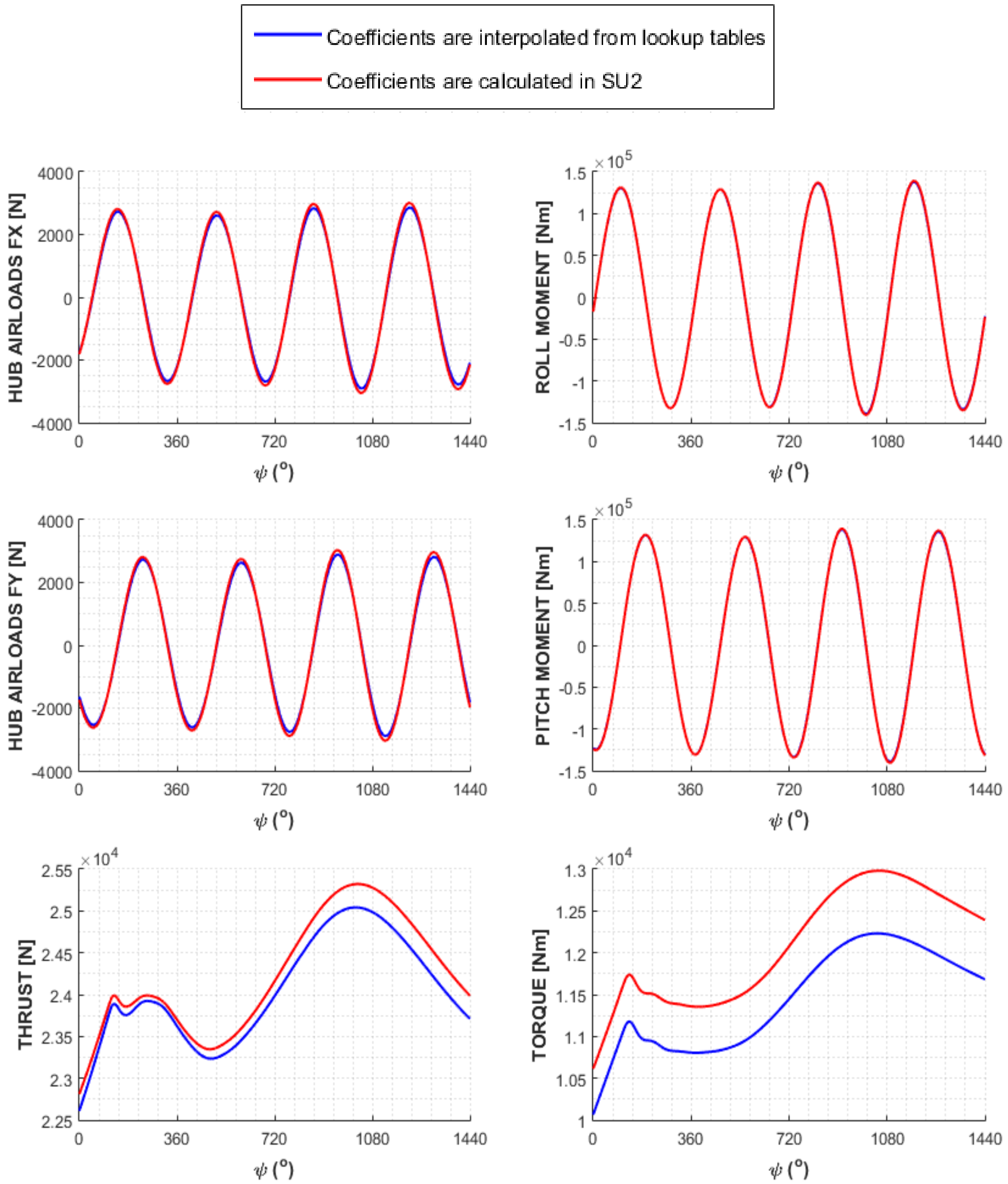

Figure 79 Rotor Hub Airloads for Dymore-SU2 Coupled Simulation for 50mm Collective Input

In Figure 79, the rotor hub airloads calculated with the Dymore-SU2 coupled simulations are given. The thrust and the torque values are overpredicted by 1% and 6% respectively. These results show that the thrust and torque values obtained by the coupled SU2-Dymore simulations are in good correlation with the thrust and torque values obtained using the lookup tables for high angles of attack. Other in-plane forces and moments are also in good agreement with the corresponding results obtained using the lookup table data. SU2-Dymore coupled calculations approximately take 110 hours for one blade with 8 airstations. Computational time is reduced to 20 hours by preventing the computation for the repetitive cases with similar angle of attack and the Mach number. In these cases, coefficients are read from stored history files.

Sample sectional solution at r/R=0.38 in this coupled simulation is presented in the following part. At this section, Mach number is 0.2, twist angle is 6^{o} and pitch angle is 8^{o}. Maximum angle of attack which the section receives at 50 mm collective input is approximately 14^{o}. The pressure distribution, turbulent viscosity distribution and the Mach distribution are given respectively in Figures 80-82 for the section at r/R=0.38 in SU2-Dymore coupled analyses in hover at 50 mm collective input. In the pressure distribution given in Figure 80, the formation of air bubble at the leading edge can be observed. It should be noted that in Figure 80, the pressure distribution is normalized to 1.

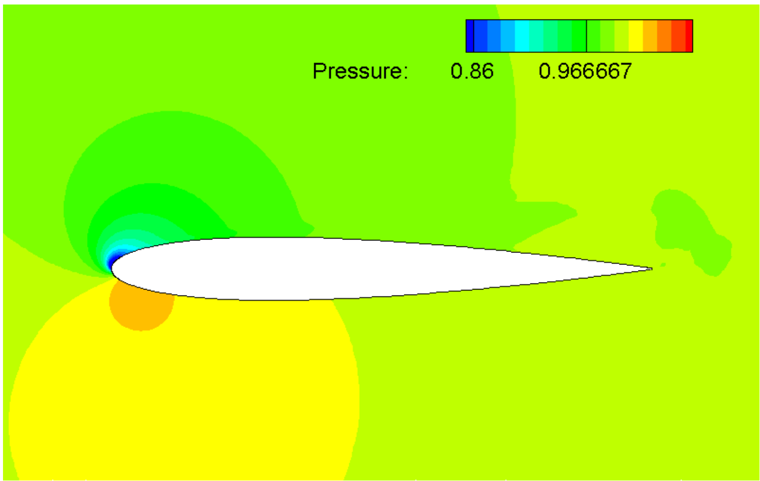

Figure 80 Pressure Distribution in SteadyAnalysis in SU2 at Mach number 0.2 and Angle of Attack of 14^{o}

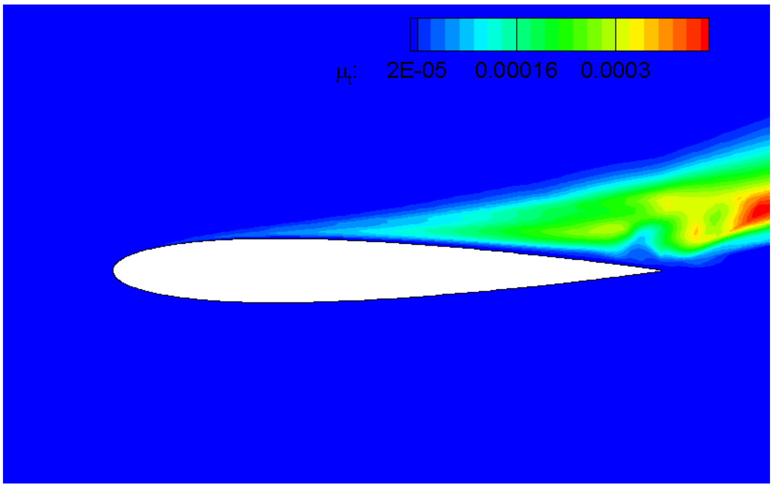

Figure 81 Turbulent Viscosity (μ_t) Distribution in SteadyAnalysis in SU2 at Mach number 0.2 and Angle of Attack of 14°

In Figure 81, the turbulent (eddy) viscosity distribution is plotted. The formation of boundary layer can be clearly seen through the eddy viscosity distribution.

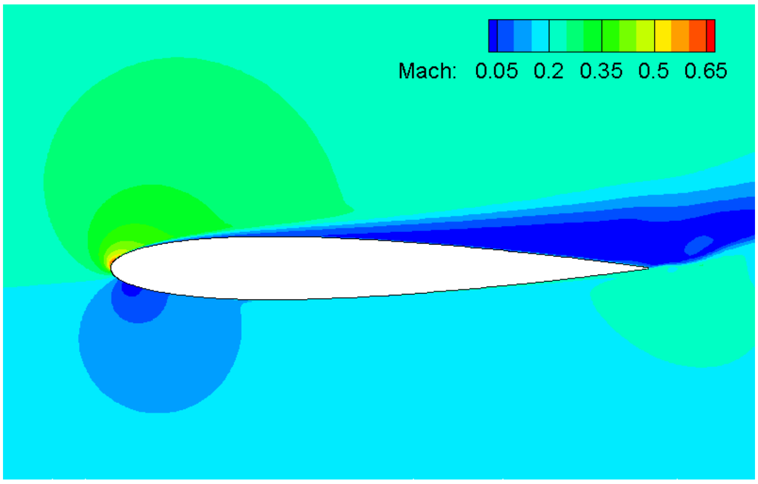

Figure 82 Mach Number Distribution at Mach number 0.2 and Angle of Attack of 14°

Figure 82 shows the Mach Distribution at the maximum angle of attack of section r/R=0.38 in Dymore-SU2 coupled analysis in hover. Since this section is close to the root, Mach number of the oncoming flow is 0.2 and Mach number around the airfoil is less than 1. The lift and the drag coefficients are presented for steady and transient analyses at the Mach number of 0.2 and the angle of attack of 14°.

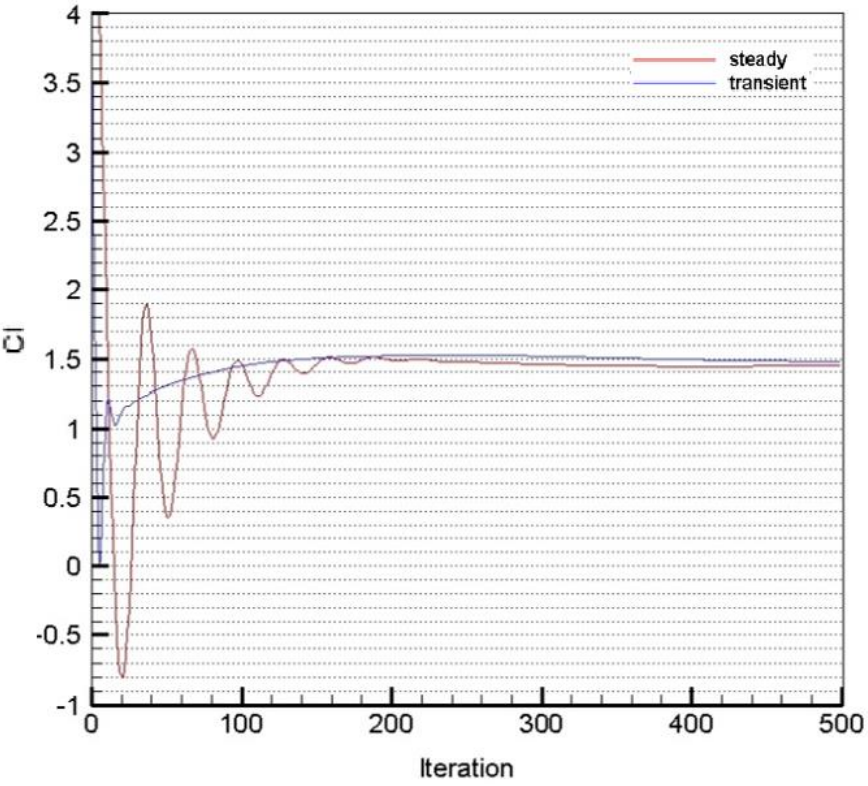

Figure 83 Cl in Steady and Transient Analyses in SU2 at Mach number 0.2 and Angle of Attack of 14°

The convergence of the lift coefficient through 500 iterations is shown in Figure 83.

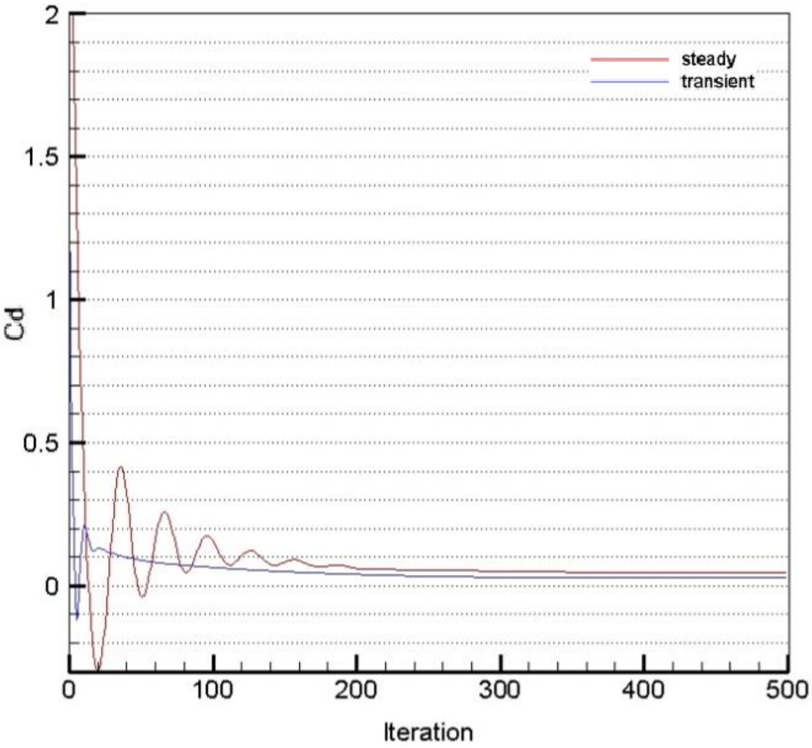

Figure 84 Cd in Steady and Transient Analyses in SU2 at Mach number 0.2 and Angle of Attack of 14º

The convergence of the drag coefficient through 500 iterations is shown in Figure 84. Drag coefficient converges after 200 iterations. Lift and the drag histories obtained by the steady analysis through Gauss-Seidel iterations show converged behaviour. The spatial discretization is the 2nd order Roe's scheme with the slope limiter. The temporal discretization is first order and implicit Euler formulation has been implemented. The turbulence model is the two equation Menter k-ω SST model which is considered as a good compromise between the k-ε models with wall functions and the standard k-ω models.

CHAPTER 4

CONCLUSION

In the comprehensive rotor dynamic analyses, the aerodynamic loads acting on the blade surface are generally calculated from the two dimensional aerodynamic performance tables which are prepared experimentally or prepared using the CFD. In this study, a multibody dynamics simulation tool, Dymore, is compiled with first an open source panel based solver, XFOIL, then with a Reynolds Averaged Navier-Stokes (RANS) solver, SU2, to perform the aerodynamic analyses for the purpose of the calculation of the aerodynamic coefficients. Dymore uses the aerodynamic performance tables in the comprehensive rotorcraft analyses as a built-in module. Thus in this study, calculation of aerodynamic coefficients is replaced with a panel method and a RANS solver. Validation studies are made for one blade for the UH-60 main rotor by selecting NACA 0012 as the airfoil profile.

4.1. Summary of the Thesis

Firstly, separate analyses are conducted in XFOIL for the angles of attack of 5^o, 10^o, 15^o and 20^o at Mach number of 0.4. It is inferred that below 15^o angle of attack, the boundary layer behavior is mainly laminar and boundary layer thickens as the angle of attack grows which is seen from aerodynamic analyses performed at angles of attack of 5^o and 10^o. Close to 15^o angle of attack, flow separation occurs at which the boundary layer exhibits transient and turbulent behavior at the same time with the laminar behavior. The air bubble formed at the leading edge causes the flow separation about 15^o angle of attack. Suction pressure at the upper surface of the airfoil drops when the angle of attack reaches to stall condition about 15^o angle of attack. As understood from the boundary layer velocity profiles, at stall, viscous effects overcome the inertial effects closer to the airfoil surface by causing viggles around the airfoil top surface. The benchmark studies which are performed independent from this thesis study show that neither the panel number or the node intensity do not have a significant role in the calculation of the aerodynamic coefficients. Similarly, separate analyses are performed for different turbulence critical amplification factors (1,4 and 9) in order to see the effects on the aerodynamic coefficients. As n decreases, the turbulence intensity increases and it is found out that as the critical amplification factor decreases, the maximum lift coefficient increases, the stall occurs earlier and the drag coefficient increases while the lift curve slope decreases. Forced transition or free transition has a slight effect on the stall angle of attack.

Secondly, steady RANS analyses are performed at the Mach numbers of 0.4 and 0.7 in SU2. The analysis for Mach number of 0.7 is performed only for 5^o angle of attack while for the Mach number of 0.4, the steady analyses are performed for 5^o and 10^o angles of attack. Laminar boundary layer behavior is observed in the analyses at Mach number of 0.4 and angles of attack of 5^o and 10^o. As the angle of attack increases, the boundary layer thickens. For the regions where the turbulent eddy viscosity is greater than 0, the Mach number is very small because of the reversed flow. The flow velocity is found out to be greater than the speed of sound which causes the shock formation at the top surface of the airfoil closer to the leading edge at Mach number of 0.7. An expansion wave occurs at the oncoming side of the flow of the supersonic region which causes a decrease in the static pressure. The expansion wave is followed by a normal shockwave when passing from the supersonic region to the subsonic region. The boundary layer with the flow separation is observed after the normal shock. In the steady computations, the lift and the drag coefficients are shown to be convergent except for one case which has the normal shockwave. For the cases with the shock, adaptive mesh refinement is mostly used in the literature. Although the solution seems not converged for the lift coefficient, it is computed for the region before the occurrence of divergence where converged behaviour is seen. In these computations double level multigrid acceleration of V scheme is used to speed up the convergence. However for the cases such as 15^o angle of attack at the Mach number of 0.4, the convergence cannot be achieved with the steady analyses by changing the CFL number or other parameters such as the slope limiter.

Transient RANS analyses are performed at the angle of attack of 15^o and at the Mach number 0.4 in SU2. As it is seen from the results that, first the separation bubble is formed at the leading edge, then it moved to the trailing edge and finally it is shed from the trailing edge. A convergent periodic solution is obtained which is understood from the residuals of the conservative variables and the residuals of the related turbulence model, which are the turbulent kinetic energy (k) and the dissipation rate (ω). The transition and flow separation location can be estimated from the boundary layer velocity profiles. In the lift, drag and moment coefficient calculations, the mean value is taken for the interval of the last five oscillations. Although the figures show the flow separation and the vortex shedding, the flow solution still lacks accuracy and fidelity. Higher resolution grids in extrusion direction can be used or RANS simulations can be switched to the LES or the DNS to increase the accuracy. Both of these methods are not appropriate for iterative and large computations regarding the computational efforts and costs when the CFD subroutines are called from the nested loops of the main program which requires too many CFD calculations.

In the next phase of the thesis study, the aerodynamic coefficients obtained from the coupled XFOIL-Dymore simulations using developed methodology is compared with the aerodynamic coefficients obtained from aerodynamic lookup tables and it is shown that coupled XFOIL-Dymore simulations produced consistent aerodynamic coefficient data with the data read from the aerodynamic lookup table. This analysis is performed when no control input is applied on the swashplate. In the sections which are exposed to high Reynolds number, drag coefficients calculated from XFOIL came out to be less than the drag coefficients interpolated from the aerodynamic performance tables. Lower drag coefficient prediction in XFOIL causes lower rotor torque compared to the rotor torque prediction obtained by using the aerodynamic lookup tables. It leads that the magnitude of the rotor torque calculated in XFOIL is predicted lower than the rotor torque calculated from the performance tables. Also, since the drag force is an in-plane force in the rotor hub plane, in-plane rotor hub forces and moments in lateral and longitudinal directions are predicted lower than the in-plane forces and moments calculated from the performance tables. Reynolds number increases with the radius towards to the tip; however, in XFOIL calculations Reynolds number is taken as 0.75 million along the blade span while the Mach-Reynolds proportionality constant and the linear variation of the Reynolds number are also tried in the XFOIL coupled calculations. However, the closest results to the aerodynamic performance tables are calculated from the constant Reynolds number analyses of 0.75 million in XFOIL. The airloads and the moments which are integrated at the rotor hub center and the aerodynamic coefficients which are obtained from the Dymore-XFOIL coupled solution came out to be similar to the values obtained from the Dymore solution performed using the aerodynamic lookup tables.

RANS coupled analyses are performed with the SST turbulence model. Zero control input case is compared with the lookup table results and XFOIL results. At the low angles of attack, the drag coefficient is predicted higher than the lookup table prediction which causes higher torque value and higher lead-lag angle amplitude. The pitch angle and the flap angle are found to be in good correlation with the Dymore analysis results obtained using the lookup table data. The thrust values are closer to the Dymore analysis results obtained by using lookup table values in the SU2 coupled analyses than the XFOIL coupled simulation which can be explained with better coefficient prediction at low angles of attack in SU2. Since an automatized healty simulation cannot be performed in XFOIL for higher angles of attack, the rotor case with the collective input is investiged in SU2 and compared with the Dymore simulation results obtained using lookup table. It is found out that the hub airloads and the angles are similar to each other.

To conclude, overall, the coupled simulation results are in good compliance with the Dymore simulation results obtained using lookup table. However, one drawback is that the coupled simulations with RANS are computationaly costly. A steady sectional analysis with 500 iterations SU2 approximately takes 5 minutes while a transient analysis takes half an hour for the given computational domain and the analysis parameters given in this study. In the present study, one blade with 8 airstations is used for the coupled simulations. One simulation is performed by adjusting the time step so that azimuthal increment is 5^o in one rotation interval. At each time step, maximum 5

Newton iterations is performed in the comprehensive simulation. Also, if the solution does not converge in a time step, first time step size is changed according to the time step size range which is prescribed by the user. In coupled SU2-Dymore simulation, the airloads are calculated from the CFD analysis and the coupled RANS simulations take approximately 110 hours in computation. However, by reducing the need for the computation for the cases with similar angle of attack and the Mach number reduces the computational time to 20 hours for hover case.

4.2. Future Work

As mentioned before, performing a coupled Dymore-CFD analysis allows shape optimization for the helicopter blades for different flight conditions such as the hover or the forward flight. The present study only aims to achieve a reliable, seamless integration of a CFD solver with Dymore. The follow-up study in the future will be the airfoil profile optimization utilizing the coupled Dymore-CFD solver suite. It should be noted that in the aerodynamic shape optimization of the governing profile of the blade, for each perturbed profile an aerodynamic analysis has to be performed and look-up table approach can not be used since the look-up tables are only valid for a specific airfoil.

Besides from the main purpose of this study, improvements in the load prediction are required for the cases in which the airfoil starts to stall and the transition or the flow separation occurs. This is needed to obtain the aerodynamic coefficients with higher fidelity. For this purpose, a transition model is required additional to the turbulence model. Recently, Bas and Cakmakcıoğlu [74] have implemented a correction based transition model by multiplying the productive terms of the SA equation with an intermittency function . A working Langtry-Menter (LM) transition model [75] which is also known as $\gamma - Re_\theta - SST$ model can be added to SU2. LM transition model is formed by adding extra two equations to the Menter-SST turbulence model. In the SST-transition model state variables are the intermittency (γ) and the momentum thickness Reynolds number (Re_θ) along with the turbulent kinetic energy (k) and the dissipation frequency (ω). However, in these models, the transition behavior is mainly governed by the turbulence intensity factor and the intermittency value entered by the user. Since these parameters alter from case to case, it is hard to have a common intermittency factor and a turbulence intensity factor for all cases in automatically coupled process. However, implementing a transition model may increase the accuracy of the coeffcients and the airloads.

In another point of view, recent studies for the helicopter rotors are stemming from the loose coupling of the comprehensive simulation tools with the CFD solvers. Three dimensional CFD calculation and data exchange between the time marching MBD simulation and the CFD at each time step are computationaly too expensive, which is known as the tight coupling. For this reason, the data exchange is achieved on a periodic basis for the CFD-CSD coupled simulations which is called as the loose coupling. This calculation is first started with the initial trim solution using the internal lookup tables. Then, the motions of the structural stations are transferred into the CFD program. In the CFD analysis, the motions are prescribed for the rotor blades. After the periodic computation is performed in CFD, the load distribution at the user defined azimuth intervals; e.g 5^o per each rotation is saved. Then, in the second step, the load difference which is called as delta airloads between the CFD load distribution and the lifting line load distribution is calculated. In the second run, the trim and the aeroelastic periodic analysis is performed with the internal lifting line airloads plus the delta airloads. The dynamic response is saved and transferred to the CFD. The lifting line airloads are calculated from the position and the orientation of the blades of the current iteration. By doing this, the trimmed analysis is corrected with the CFD by the step inputs in the comprehensive simulation tool. As another future work, loose coupling can be performed between Dymore and SU2 on an unstructured grid and the data exchange can be achieved between the MBD and the CFD since the methodology is simple and clear.

RANS simulations are preferred as the CFD methodology since other high fidelity computations related to turbulence; that is, LES or DNS are computationally costly. To include the boundary layer effect on the surface of the blade correctly, an overset grid is used with a cartesian background grid consisting of approximately 50 million cells in most of the studies in the literature [24]. Farfield boundaries for the background cartesian grid in the related studies are in dimensions of 20 radius in the radial direction, 5 radius in the axial direction and 30 radius in the downwash direction for isolated rotors.

Since CFD is expensive, most recent methods involve the combination of Navier-Stokes with filament based or sheet based free wake methods. Unsteady viscous computations are performed at the near farfield when Biot-Savart law based vortex sheet computation is performed at the farfield. In the literature, such utilization is called as the hybrid method. Using hybrid methods, high fidelity flow solution required for the regions closer to the blade can be calculated which cannot be obtained by solely using the lifting surface theory or the vortex lattice method. Also, this kind of implementation reduces the computational costs at the regions far away from the blade. This type of the application also can be performed between Dymore, SU2 and CHARM, the latter of which is a freewake calculation program. It uses fast vortex panel methods, related to the lifting surface theory or the vortex lattice method based on the Biot-Savart law.

According to the main purpose of this study besides from the future studies mentioned above, the initial aim will be performing a power optimization in future for the same thrust value. A gradient based optimization methodology will be used for the perturbation of the sections. Same airfoil profile will be used along blade span as this study assuming that the most governing section of the blade is being optimized. The airfoil surface will be discretized and the perturbations will be given to the surface nodes by using the Hicks-Henne polynomials. The change in the power to thrust ratio will be calculated for each perturbed section. Therefore, a gradient vector will be obtained between the variables and the target. In order to reach the target power to thrust ratio, the solution can be marched along the gradient vector. If the extrema point is exceeded, the solution has to go to the previous step and the gradient vector should be recalculated. Following this procedure, an optimized profile considered for the hover condition or the forward flight condition can be obtained for the main rotor or the tail rotor blades. The optimization will be performed using Dymore, XFOIL and SU2.

REFERENCES

[1] W. Johnson, “A History of Rotorcraft Comprehensive Analyses,” NASA Technical Note TP-2012-216012, 2012.

[2] D. A. Peters and C. J. He, “Finite State Induced Flow Models Part II: Three-Dimensional Rotor Disk David,” Journal of Aircraft, vol. 32, no. 2, pp. 323–333, 1995.

[3] J. G. Leishman and T. S. Beddoes, “A Semi-Empirical Model for Dynamic Stall,” Journal of the American Helicopter Society, vol. 34, no. 3, pp. 3–17, 1989.

[4] D. Petot, “Differential equation modeling of dynamic stall,” La Recherche Aerospatiale, vol. 5, pp. 59–72, 1989.

[5] K. W. Mcalister, O. Lambert, and D. Petot, “Application of the ONERA Model of Dynamic Stall,” NASA Technical Paper 2399, 1984.

[6] W. J. McCroskey, “A critical assessment of wind tunnel results for the NACA 0012 airfoil,” NASA Technical Memorandum 100019, October, 1987.

[7] I. H. Abbott and A. E. Von Doenhoff, Theory of Wing Sections: Including a Summary of Airfoil data. New York: Dover Publications, Inc., 1959.

[8] C. L. Ladson, “Effects of Independent Variation of Mach and Reynolds Numbers on the Low-Speed Aerodynamic Characteristics of the NACA 0012 Airfoil Section,” NASA Technical Memorandum 4074, October, 1988.

[9] N. Gregory and C. L. O’Reilly, “Low-Speed Aerodynamic Characteristics of NACA 0012 Aerofoil Section, including the Effects of Upper-Surface Roughness Simulating Hoar Frost,” U.S. Ministry of Defense Aeronautical Research Council Reports and Memoranda No. 3726, 1973.

[10] L. L. Green and P. A. Newman, “Transonic Wall Interference Assessment and Adaptive Wall Test Section,” in AIAA 19th Fluid Dynamics, Plasma Dynamics and Lasers Conference, 1987.

[11] C. C. Critzos, H. Heyson, and R. W. Boswinkle Jr., “Aerodynamic Characteristics of Naca 0012 Airfoil At Angles of Attack From 0 ° To 180 °,” NACA Technical Note 3361, 1955.

[12] C. D. Harris, “Two-dimensional aerodynamic characteristics of the NACA 0012 airfoil in the Langley 8 foot transonic pressure tunnel,” NASA Technical Memorandum 81927, 1981.

[13] J. Totah, “A Critical Assessment of UH-60 Main Rotor Blade Airfoil Data,” NASA Technical Memorandum 103985, September, 1993.

[14] W. G. Bousman, “Aerodynamic Characteristics of SC1095 and SC1094 R8 Airfoils,” NASA/TP–2003-212265, December, 2003.

[15] M. J. Smith, T. Wong, M. A. Potsdam, J. Baeder, and S. Phanse, “Evaluation of CFD to Determine Two-Dimensional Airfoil Characteristics for Rotorcraft Applications,” Journal of the American Helicopter Society, vol. 51, no. 1, pp. 70–79, 2006.

[16] P. G. Buning, D. C. Jespersen, T. H. Pulliam, W. M. Chan, J. P. Slotnick, S. E. Krist, K. J. Renze, “OVERFLOW User’s Manual, Version 1.8s.” NASA Langley Research Center, 1998.

[17] W. K. Anderson and D. L. Bonhaus, “An implicit upwind algorithm for computing turbulent flows on unstructured grids,” Journal of Computational Fluids, vol. 23, no. 1, pp. 1–21, 1994.

[18] L. Rumsey, T. Biedron, and L. Thomas, “CFL3D : Its History Applications,” Fluid Dynamics. NASA Technical Memorandum 112861, May, 1997.

[19] W. Z. Strang, R. F. Tomaro, and M. J. Grismer, “The Defining Methods of Cobalt60: a Parallel, Implicit, Unstructured Euler/Navierstokes Flow Solver,” 37th AIAA Aerospace Sciences Meeting and Exhibit, Reno, Nevada, January 11-14, 1999.

[20] J. D. Srinivasan, G. R., Baeder, “TURNS: A Free Wake Euler/Navier-Stokes Numerical Method for Helicopter Rotors,” AIAA Journal, vol. 31, no. 5, pp. 959–962, 1991.

[21] M. Drela, “A User’s Guide to MSES 3.05,” July, 2007.

[22] E. A. Mayda and C. P. van Dam, “Automated generation of airfoil performance tables using a two-dimensional Navier-Stokes solver,” Journal of the American Helicopter Society, vol. 50, no. 4, pp. 338–348, 2005.

[23] T. H. Pulliam, “Solution Methods In Computational Fluid Dynamics,” NASA Ames Research Center, 2005.

[24] M. Potsdam, H. Yeo, and W. Johnson, “Rotor Airloads Prediction Using Loose Aerodynamic/Structural Coupling,” Journal of Aircraft, vol. 43, no. 3, pp. 732–42, 2006.

[25] A. A. Zaki, “Using Tightly-Coupled CFD / CSD Simulation for Rotorcraft Stability Analysis,” Phd. Thesis. Georgia Institute of Technology, May, 2012.

[26] N. D. Reveles, “Advanced Methods For Dynamic Aeroelastic Analysis Of Rotors,” Phd. Thesis. Georgia Institute of Technology, May, 2014.

[27] S. J. Massey, A. R. Kreshock, and M. K. Sekula, “Coupled CFD / CSD Analysis of Rotor Blade Structural Loads with Experimental Validation,” in 31st AIAA Applied Aerodynamics Conference, San Diego, California, 24-27 June, 2013.

[28] M. J. Smith et al., “An Assessment of Comprehensive Code Prediction State-of-the-Art Using the HART II International Workshop Data,” in Proceedings of the 68th Annual Forum of the American Helicopter Society, Ft. Worth, Texas, May 1-3, 2012.

[29] D. Wachspress, T. R. Quackenbusch, and A. . Boschitsch, “First-principles free-vortex wake analysis for helicopters and tiltrotors,” in Proceedings of the 59th Annual Forum of the American Helicopter Society, Phoenix, Arizona, May 6-8, 2003

[30] M. P. Scully, “Computation of helicopter rotor wake geometry and its influence on rotor harmonic airloads,” Phd. Thesis. Massachusetts Institute of Technology, February, 1975.

[31] G. H. Vatistas, V. Kozel, and W. C. Mih, “A simpler model for concentrated vortices,” Experiments in Fluids, vol. 11, no. 1, pp. 73–76, 1991.

[32] “V-22 Osprey.”, Retrieved June 06, 2018 from https://en.wikipedia.org/wiki/Tiltrotor#/media/File:US_Navy_061206-N-0458E-076_A_U.S._Marine_Corps_V-22_Osprey_helicopter_practices_touch_and_go_landings_on_the_flight_deck_of_the_multipurpose_amphibious_assault_ship_USS_Wasp_(LHD_1).jpg.

[33] “CH-46 Sea Knight.”, Retrieved June 06, 2018 from https://en.wikipedia.org/wiki/Tandem_rotors#/media/File:USMC_CH-46.jpg.

[34] “KamowK32A.”, Retrieved June 06, 2018 from https://en.wikipedia.org/wiki/Coaxial_rotors#/media/File:KamowK32A.jpg.

[35] “AutoGyro MTOsport. ”, Retrieved June 06, 2018 from

https://en.wikipedia.org/wiki/AutoGyro_MT-03#/media/File:Autogyro_MT-03_(D-MTBI)_06.jpg.

[36] “MD Explorer. ”, Retrieved June 06, 2018 from https://www.aircraftcompare.com/aircraftimage/MD-Explorer-Photo-4/2073.

[37] “CH53G-Rotorhead. ”, Retrieved June 06, 2018 from http://www.b-domke.de/AviationImages/Rotorhead/15969.html.

[38] “R22-Rotorhead. ”, Retrieved June 06, 2018 from https://rc.runryder.com/helicopter/t490297p1/?p=4005063#RR.

[39] “BO105-Rotorhead. ”, Retrieved June 06, 2018 from http://www.b-domke.de/AviationImages/Rotorhead/0416.html.

[40] “Multibody simulation of the power boosted control section of a medium sized helicopter. ”, Retrieved June 06, 2018 from https://www.slideshare.net/AltairHTC/multibody-simulation-of-the-power-boosted-control-section-of-a-medium-sized-helicopter

[41] J. Johnston, “EC-155 Helicopter. ”, Retrieved August 17, 2014 from https://grabcad.com/library/ec-155-helicopter.

[42] W. Johnson, Helicopter theory. New York: Dover Publications, Inc., 1994.

[43] T. Theodorsen, “General theory of aerodynamic instability and the mechanism of flutter,” NACA Technical Report No. 496, January, 1949.

[44] A. R. S. Bramwell, G. Done, and D. Balmford, Bramwell’s Helicopter Dynamics, 2nd Edit. Oxford: Butterworth-Heinemann, 2001.

[45] O. Muvengei, J. Kihiu, and B. Ikua, “Dynamic analysis of multi-body mechanical systems with imperfect kinematic joints: a literature survey and review,” Sustainable Research and Innovation Proceedings, vol. 3, pp. 61–76, 2011.

[46] D. Negrut and A. Dyer, “ADAMS / Solver Primer,” Ann Arbor, Michigan, 2004.

[47] O. A. Bauchau, “DYMORE: a finite element based tool for the analysis of nonlinear flexible multibody systems,” Georgia Institute of Technology, 2001.

[48] D. H. Hodges, Nonlinear composite beam theory. Reston, Virginia: American Institute of Aeronautics and Astronautics, Inc., 2006.

[49] “UH-60 Black Hawk Main Rotor Head. ”, Retrieved August 17, 2014 from” https://grabcad.com/library/uh-60-black-hawk-main-rotor-head.

[50] Z. Gusztus, “UH-60 Blackhawk Main rotor Hardsurface model.”, Retrieved June 7, 2018 from https://www.artstation.com/artwork/uh-60-blackhawk-main-rotor-hardsurface-model.

[51] J. Seddon, Basic Helicopter Aerodynamics. Oxford: BSP Professional Books, 1990.

[52] R. P. Coleman, A. M. Feingold, C. W. Stempin, “Evaluation of the Induced-Velocity Field of an Idealized Helicoptor Rotor,” NACA Wartime Report, L5E10, 1945.

[53] W. Castles Jr and J. H. De Leeuw, “The Normal Component of the Induced Velocity in the Vicinity of a Lifting Rotor and Some Examples of its Application,” NACA Report 1184, 1954.

[54] H. H. Heyson and S. Katzoff, “Induced Velocities Near a Lifting Rotor with Nonuniform Disk Loading,” NACA Technical Report 1319, 1957.

[55] K. W. Mangler and H. B. Squire, “The Induced Velocity Field of a Rotor,” U.S. Ministry of Supply Aeronautical Research Council Reports and Memoranda No. 2642, 1953.

[56] J. G. Leishman, Principles of Helicopter Aerodynamics, Second Edition. New York: Cambridge University Press, 2006.

[57] T. A. Egolf and A. J. Landgrebe, “A Prescribed Wake Rotor Inflow and Flow Field Prediction Analysis - User’s Manual and Technical Approach,” NASA Contractor Report 165894, June, 1982.

[58] R. T. N. Chen, “A Survey of Nonuniform Inflow Models for Rotorcraft Flight Dynamics and Control Applications A Survey of Nonuniform Inflow Models for Rotorcraft Flight Dynamics and Control Applications,” NASA Technical Memorandum 102219, November, 1989.

[59] J. Anderson Jr, Fundamentals of Aerodynamics, Third Edition. New York: McGraw Hill, 1985.

[60] D. A. Peters, S. Karunamoorthy, and W. M. Cao, “Finite State Induced Flow Models, Part I: Two Dimensional Thin Airfoil,” Journal of Aircraft, vol. 32, no. 2, pp. 313–322, 1995.

[61] O. A. Bauchau, “Dymore User’s Manual - Unsteady Aerodynamics.”

[62] D. A. Peters, M. A. Hsieh, and A. Torrero, “A State-Space Airloads Theory for Flexible Airfoils,” Journal of the American Helicopter Society, vol. 52, no. 4, p. 329, 2007.

[63] M. Drela, “XFOIL: An Analysis and Design System for Low Reynolds Number Airfoils.”, 1989.

[64] M. Drela and M. B. Giles, “Viscous-inviscid analysis of transonic and low Reynolds number airfoils,” AIAA Journal, vol. 25, no. 10, pp. 1347–1355, 1987.

[65] D. L. Whitfield, “Integral solution of compressible turbulent boundary layers using improved velocity profiles,” Arnold Engineering Development Center AEDC-TR-78-42, December, 1978.

[66] T. W. Swafford, “Analytical approximation of two-dimensional separated turbulent boundary-layer velocity profiles,” AIAA Journal, vol. 21, no. 6, pp. 923–926, 1983.

[67] F. Palacios, T. D. Economon, A. C. Aranake, S. R. Copeland, A. K. Lonkar, T. W. Lukaczyk, D. E. Manosalvas, K. R. Naik, A. S. Padron, B. Tracey, A. Variyar, J. J. Alonso, “Stanford University Unstructured (SU2): Open-source Analysis and Design Technology for Turbulent Flows,” AIAA SciTech 52nd Aerospace Sciences Meeting, National Harbor, Maryland, 13-17 January, 2014.

[68] ANSYS, “Fluent Documentation - Lecture 7: Turbulence Modeling,”, 2014.

[69] P. R. Spalart and S. R. Allmaras, “A one-equation turbulence model for aerodynamic flows,” La Recherche Aerospatiale, vol. 1, no. 1, pp. 5–21, 1994.

[70] S. R. Allmaras, F. T. Johnson, and P. R. Spalart, “Modifications and clarifications for the implementation of the Spalart-Allmaras turbulence model,” in Seventh International Conference on Computational Fluid Dynamics (ICCFD7), Big Island, Havaii, 9-13 July, 2012.

[71] F. R. Menter, “Zonal Two Equation k-omega, Turbulence Models for Aerodynamic Flows,” in AIAA 24th Fluid Dynamics Conference, Orlando, Florido, 6-9 July, 1993.

[72] D. Kumar, “Design and Analysis of Composite Rotor Blades for Active / Passive Vibration Reduction,” Phd. Thesis. University of Michigan, 2013.

[73] J. Navarrete, “Construction of Airfoil Performance Tables by the Fusion of Experimental and Numerical Data,” MSc. Thesis. Rice University, August, 2004.

[74] S. C. Cakmakcioglu, O. Bas, and U. Kaynak, “A correlation-based algebraic transition model,” Journal of Mechanical Engineering Science, vol. 1, no. 15, 2017.

[75] R. B. Langtry and F. R. Menter, “Correlation-Based Transition Modeling for Unstructured Parallelized Computational Fluid Dynamics Codes,” AIAA Journal, vol. 47, no. 12, pp. 2894–2906, 2009.

APPENDIX A

Reference Aerodynamic Lookup Table for NACA 0012 Airfoil

Table A.1 NACA 0012 airfoil reference Cl table

	Mach Number										
α	**0**	**0.2**	**0.3**	**0.4**	**0.5**	**0.6**	**0.7**	**0.75**	**0.8**	**0.9**	**1**
-180	0	0	0	0	0	0	0	0	0	0	0
-172.5	0.78	0.78	0.78	0.78	0.78	0.78	0.78	0.78	0.78	0.78	0.78
-161	0.62	0.62	0.62	0.62	0.62	0.62	0.62	0.62	0.62	0.62	0.62
-147	1	1	1	1	1	1	1	1	1	1	1
-129	1	1	1	1	1	1	1	1	1	1	1
-49	-1.18	-1.18	-1.18	-1.18	-1.18	-1.18	-1.18	-1.18	-1.18	-1.18	-1.18
-39	-1.18	-1.18	-1.18	-1.18	-1.18	-1.18	-1.18	-1.18	-1.18	-1.18	-1.18
-21	-0.8	-0.8	-0.81	-0.83	-0.85	-0.85	-0.85	-0.71	-0.68	-0.64	-0.64
-16.5	-1.007	-1.007	-0.944	-0.96	-0.965	-0.965	-0.965	-0.795	-0.76	-0.7	-0.7
-15	-1.19	-1.19	-1.09	-1.055	-0.99	-0.98	-0.98	-0.83	-0.79	-0.72	-0.72
-14	-1.333	-1.333	-1.22	-1.096	-1	-0.97	-0.97	-0.84	-0.805	-0.73	-0.73
-13	-1.334	-1.334	-1.28	-1.12	-1	-0.96	-0.96	-0.85	-0.815	-0.735	-0.735
-12	-1.255	-1.255	-1.26	-1.13	-1	-0.947	-0.94	-0.85	-0.82	-0.74	-0.74
-11	-1.161	-1.161	-1.19	-1.12	-0.994	-0.93	-0.923	-0.85	-0.81	-0.74	-0.74
-10	-1.055	-1.055	-1.01	-1.082	-0.985	-0.91	-0.9	-0.845	-0.805	-0.73	-0.73
-8	-0.844	-0.844	-0.88	-0.907	-0.922	-0.87	-0.84	-0.82	-0.77	-0.695	-0.695
-6	-0.633	-0.633	-0.66	-0.684	-0.741	-0.77	-0.75	-0.77	-0.72	-0.593	-0.593
-4	-0.422	-0.422	-0.44	-0.456	-0.494	-0.544	-0.578	-0.627	-0.603	-0.396	-0.396
-2	-0.211	-0.211	-0.22	-0.228	-0.247	-0.272	-0.313	-0.35	-0.395	-0.2	-0.2
0	0	0	0	0	0	0	0	0	0	0	0
2	0.211	0.211	0.22	0.228	0.247	0.272	0.313	0.35	0.395	0.2	0.2
4	0.422	0.422	0.44	0.456	0.494	0.544	0.578	0.627	0.603	0.396	0.396
6	0.633	0.633	0.66	0.684	0.741	0.77	0.75	0.77	0.72	0.593	0.593
8	0.844	0.844	0.88	0.907	0.922	0.87	0.84	0.82	0.77	0.695	0.695
10	1.055	1.055	1.1	1.082	0.985	0.91	0.9	0.845	0.805	0.73	0.73
11	1.161	1.161	1.19	1.12	0.994	0.93	0.923	0.85	0.81	0.74	0.74
12	1.255	1.255	1.26	1.13	1	0.947	0.94	0.85	0.82	0.74	0.74
13	1.334	1.334	1.28	1.12	1	0.96	0.96	0.85	0.815	0.735	0.735
14	1.333	1.333	1.22	1.096	1	0.97	0.97	0.84	0.805	0.73	0.73
15	1.19	1.19	1.09	1.055	0.99	0.98	0.98	0.83	0.79	0.73	0.73

Table A.1 continued

16.5	1.007	1.007	0.944	0.96	0.965	0.965	0.965	0.795	0.76	0.7	0.7
21	0.8	0.8	0.81	0.83	0.85	0.85	0.85	0.71	0.68	0.64	0.64
39	1.18	1.18	1.18	1.18	1.18	1.18	1.18	1.18	1.18	1.18	1.18
49	1.18	1.18	1.18	1.18	1.18	1.18	1.18	1.18	1.18	1.18	1.18
129	-1	-1	-1	-1	-1	-1	-1	-1	-1	-1	-1
147	-1	-1	-1	-1	-1	-1	-1	-1	-1	-1	-1
161	-0.62	-0.62	-0.62	-0.62	-0.62	-0.62	-0.62	-0.62	-0.62	-0.62	-0.62
172.5	-0.78	-0.78	-0.78	-0.78	-0.78	-0.78	-0.78	-0.78	-0.78	-0.78	-0.78
180	0	0	0	0	0	0	0	0	0	0	0

Table A.2 NACA 0012 airfoil reference Cd table

					Mach Number						
α	**0**	**0.18**	**0.28**	**0.38**	**0.48**	**0.62**	**0.72**	**0.77**	**0.82**	**0.92**	**1**
-180	0.022	0.022	0.022	0.022	0.022	0.022	0.022	0.022	0.022	0.022	0.022
-175	0.062	0.062	0.062	0.062	0.062	0.062	0.062	0.062	0.062	0.062	0.062
-170	0.132	0.132	0.132	0.132	0.132	0.132	0.132	0.132	0.132	0.132	0.132
-165	0.242	0.242	0.242	0.242	0.242	0.242	0.242	0.242	0.242	0.242	0.242
-160	0.302	0.302	0.302	0.302	0.302	0.302	0.302	0.302	0.302	0.302	0.302
-140	1.042	1.042	1.042	1.042	1.042	1.042	1.042	1.042	1.042	1.042	1.042
-120	1.652	1.652	1.652	1.652	1.652	1.652	1.652	1.652	1.652	1.652	1.652
-110	1.852	1.852	1.852	1.852	1.852	1.852	1.852	1.852	1.852	1.852	1.852
-100	2.022	2.022	2.022	2.022	2.022	2.022	2.022	2.022	2.022	2.022	2.022
-90	2.022	2.022	2.022	2.022	2.022	2.022	2.022	2.022	2.022	2.022	2.022
-80	1.962	1.962	1.962	1.962	1.962	1.962	1.962	1.962	1.962	1.962	1.962
-70	1.842	1.842	1.842	1.842	1.842	1.842	1.842	1.842	1.842	1.842	1.842
-60	1.662	1.662	1.662	1.662	1.662	1.662	1.662	1.662	1.662	1.662	1.662
-50	1.392	1.392	1.392	1.392	1.392	1.399	1.392	1.392	1.392	1.392	1.392
-30	0.562	0.562	0.562	0.562	0.562	0.562	0.562	0.562	0.562	0.562	0.562
-21	0.332	0.332	0.332	0.332	0.332	0.332	0.332	0.332	0.332	0.342	0.342
-16	0.155	0.155	0.181	0.207	0.235	0.257	0.274	0.292	0.305	0.342	0.342
-15	0.102	0.102	0.148	0.181	0.209	0.233	0.252	0.271	0.282	0.298	0.298
-14	0.038	0.038	0.099	0.146	0.18	0.212	0.233	0.249	0.26	0.293	0.293
-13	0.0264	0.0264	0.0455	0.094	0.148	0.191	0.216	0.231	0.239	0.272	0.292
-12	0.022	0.022	0.03	0.06	0.111	0.164	0.198	0.211	0.22	0.252	0.291
-11	0.0196	0.0196	0.0232	0.038	0.078	0.135	0.17	0.192	0.202	0.232	0.275
-10	0.0174	0.0174	0.0189	0.0259	0.053	0.105	0.145	0.176	0.186	0.213	0.254
-9	0.0154	0.0154	0.0159	0.0187	0.0351	0.077	0.122	0.159	0.172	0.199	0.232
-8	0.0138	0.0138	0.0138	0.0147	0.022	0.053	0.101	0.14	0.155	0.183	0.214
-7	0.0122	0.0122	0.0122	0.0123	0.0141	0.035	0.082	0.111	0.139	0.169	0.192

Table A.2 continued

-6	**0.011**	**0.011**	**0.011**	**0.011**	**0.011**	**0.0212**	**0.0615**	**0.082**	**0.12**	**0.14**	**0.17**
-5	0.01	0.01	0.01	0.01	0.01	0.0132	0.038	0.054	0.088	0.111	0.14
-4	0.0093	0.0093	0.0093	0.0093	0.0093	0.01	0.0167	0.03	0.0575	0.095	0.112
-3	0.0088	0.0088	0.0088	0.0088	0.0088	0.009	0.0102	0.0175	0.0355	0.086	0.102
-2	0.0085	0.0085	0.0085	0.0085	0.0085	0.0085	0.0086	0.0117	0.024	0.081	0.098
-1	0.0083	0.0083	0.0083	0.0083	0.0083	0.0083	0.0083	0.0091	0.0175	0.078	0.096
0	0.008	0.008	0.008	0.008	0.008	0.008	0.008	0.008	0.0137	0.078	0.095
1	0.0083	0.0083	0.0083	0.0083	0.0083	0.0083	0.0083	0.0091	0.0175	0.078	0.096
2	0.0085	0.0085	0.0085	0.0085	0.0085	0.0085	0.0086	0.0117	0.024	0.081	0.098
3	0.0088	0.0088	0.0088	0.0088	0.0088	0.009	0.0102	0.0175	0.0355	0.086	0.102
4	0.0093	0.0093	0.0093	0.0093	0.0093	0.01	0.0167	0.03	0.0575	0.095	0.112
5	0.01	0.01	0.01	0.01	0.01	0.0132	0.038	0.054	0.088	0.111	0.14
6	0.011	0.011	0.011	0.011	0.011	0.0212	0.0615	0.082	0.12	0.14	0.17
7	0.0122	0.0122	0.0122	0.0123	0.0141	0.035	0.082	0.111	0.139	0.169	0.192
8	0.0138	0.0138	0.0138	0.0147	0.022	0.053	0.101	0.14	0.155	0.183	0.214
9	0.0154	0.0154	0.0159	0.0187	0.0351	0.077	0.122	0.159	0.172	0.199	0.232
10	0.0174	0.0174	0.0189	0.0259	0.053	0.105	0.145	0.176	0.186	0.213	0.254
11	0.0196	0.0196	0.0232	0.038	0.078	0.135	0.17	0.192	0.202	0.232	0.275
12	0.022	0.022	0.03	0.06	0.111	0.164	0.198	0.211	0.22	0.252	0.291
13	0.0264	0.0264	0.0455	0.094	0.148	0.191	0.216	0.231	0.239	0.272	0.292
14	0.038	0.038	0.099	0.146	0.18	0.212	0.233	0.249	0.26	0.293	0.293
15	0.102	0.102	0.148	0.181	0.209	0.233	0.252	0.271	0.282	0.298	0.298
16	0.155	0.155	0.181	0.207	0.235	0.257	0.274	0.292	0.305	0.342	0.342
21	0.332	0.332	0.332	0.332	0.332	0.332	0.332	0.332	0.332	0.342	0.342
30	0.562	0.562	0.562	0.562	0.562	0.562	0.562	0.562	0.562	0.562	0.562
50	1.392	1.392	1.392	1.392	1.392	1.392	1.392	1.392	1.392	1.392	1.392
60	1.662	1.662	1.662	1.662	1.662	1.662	1.662	1.662	1.662	1.662	1.662
70	1.842	1.842	1.842	1.842	1.842	1.842	1.842	1.842	1.842	1.842	1.842
80	1.962	1.962	1.962	1.962	1.962	1.962	1.962	1.962	1.962	1.962	1.962
90	2.022	2.022	2.022	2.022	2.022	2.022	2.022	2.022	2.022	2.022	2.022
100	2.022	2.022	2.022	2.022	2.022	2.022	2.022	2.022	2.022	2.022	2.022
110	1.852	1.852	1.852	1.852	1.852	1.852	1.852	1.852	1.852	1.852	1.852
120	1.652	1.652	1.652	1.652	1.652	1.652	1.652	1.652	1.652	1.652	1.652
140	1.042	1.042	1.042	1.042	1.042	1.042	1.042	1.042	1.042	1.042	1.042
160	0.302	0.302	0.302	0.302	0.302	0.302	0.302	0.302	0.302	0.302	0.302
165	0.242	0.242	0.242	0.242	0.242	0.242	0.242	0.242	0.242	0.242	0.242
170	0.132	0.132	0.132	0.132	0.132	0.132	0.132	0.132	0.132	0.132	0.132
175	0.062	0.062	0.062	0.062	0.062	0.062	0.062	0.062	0.062	0.062	0.062
180	0.022	0.022	0.022	0.022	0.022	0.022	0.022	0.022	0.022	0.022	0.022

Table A.3 NACA 0012 airfoil reference Cm table

	Mach Number									
α	**0**	**0.2**	**0.3**	**0.4**	**0.5**	**0.6**	**0.7**	**0.75**	**0.8**	**1**
-180	0	0	0	0	0	0	0	0	0	0
-170	0.4	0.4	0.4	0.4	0.4	0.4	0.4	0.4	0.4	0.4
-165	0.3	0.3	0.3	0.3	0.3	0.3	0.3	0.3	0.3	0.3
-160	0.3	0.3	0.3	0.3	0.3	0.3	0.3	0.3	0.3	0.3
-135	0.5	0.5	0.5	0.5	0.5	0.5	0.5	0.5	0.5	0.5
-90	0.5	0.5	0.5	0.5	0.5	0.5	0.5	0.5	0.5	0.5
-30	0.174	0.174	0.184	0.196	0.214	0.235	0.25	0.264	0.277	0.298
-23	0.112	0.112	0.118	0.128	0.144	0.157	0.171	0.183	0.206	0.232
-16	0.073	0.073	0.078	0.086	0.097	0.108	0.117	0.137	0.176	0.2
-15	0.054	0.054	0.065	0.073	0.084	0.097	0.111	0.133	0.173	0.195
-14	0	0	0.027	0.054	0.068	0.086	0.103	0.127	0.167	0.189
-13	0	0	0.0015	0.025	0.05	0.074	0.093	0.122	0.163	0.184
-12	0	0	0	0.002	0.03	0.06	0.083	0.116	0.157	0.176
-11	0	0	0	-0.003	0.014	0.046	0.074	0.108	0.149	0.17
-10	0	0	0	-0.0015	0.002	0.032	0.065	0.1	0.142	0.163
-9	0	0	0	0	-0.003	0.016	0.054	0.089	0.132	0.154
-8	0	0	0	0	-0.004	0.005	0.041	0.082	0.123	0.145
-7	0	0	0	0	0	-0.004	0.0275	0.072	0.1125	0.136
-6	0	0	0	0	0	-0.003	0.016	0.0625	0.1	0.125
-4	0	0	0	0	0	0	0.005	0.04	0.076	0.102
-3	0	0	0	0	0	0	-0.0025	0.026	0.0665	0.087
-2	0	0	0	0	0	0	0	0.013	0.053	0.07
-1	0	0	0	0	0	0	0	0.0035	0.033	0.045
0	0	0	0	0	0	0	0	0	0	0
1	0	0	0	0	0	0	0	-0.0035	-0.033	-0.045
2	0	0	0	0	0	0	0	-0.013	-0.053	-0.07
3	0	0	0	0	0	0	0.0025	-0.026	-0.0665	-0.087
4	0	0	0	0	0	0	-0.005	-0.04	-0.076	-0.102
6	0	0	0	0	0	0.003	-0.016	-0.0625	-0.1	-0.125
7	0	0	0	0	0	0.004	-0.0275	-0.072	-0.1125	-0.136
8	0	0	0	0	0.004	-0.005	-0.041	-0.082	-0.123	-0.145
9	0	0	0	0	0.003	-0.016	-0.054	-0.089	-0.132	-0.154
10	0	0	0	0.0015	-0.002	-0.032	-0.065	-0.1	-0.142	-0.163
11	0	0	0	0.003	-0.014	-0.046	-0.074	-0.108	-0.149	-0.17
12	0	0	0	-0.002	-0.03	-0.06	-0.083	-0.116	-0.157	-0.176
13	0	0	-0.0015	-0.025	-0.05	-0.074	-0.093	-0.122	-0.163	-0.184
14	0	0	-0.027	-0.054	-0.068	-0.086	-0.103	-0.127	-0.167	-0.189
15	-0.054	-0.054	-0.065	-0.073	-0.084	-0.097	-0.111	-0.133	-0.173	-0.195

Table A.3 continued

16	-0.073	-0.073	-0.078	-0.086	-0.097	-0.108	-0.117	-0.137	-0.176	-0.2
23	-0.112	-0.112	-0.118	-0.128	-0.144	-0.157	-0.171	-0.183	-0.206	-0.232
30	-0.174	-0.174	-0.184	-0.196	-0.214	-0.235	-0.25	-0.264	-0.277	-0.298
90	-0.5	-0.5	-0.5	-0.5	-0.5	-0.5	-0.5	-0.5	-0.5	-0.5
135	-0.5	-0.5	-0.5	-0.5	-0.5	-0.5	-0.5	-0.5	-0.5	-0.5
160	-0.3	-0.3	-0.3	-0.3	-0.3	-0.3	-0.3	-0.3	-0.3	-0.3
165	-0.3	-0.3	-0.3	-0.3	-0.3	-0.3	-0.3	-0.3	-0.3	-0.3
170	-0.4	-0.4	-0.4	-0.4	-0.4	-0.4	-0.4	-0.4	-0.4	-0.4
180	0	0	0	0	0	0	0	0	0	0

APPENDIX B

NACA 0012 Airfoil Coordinates

Table B.1 NACA 0012 airfoil coordinates

x	y	x	y	x	y	x	y
1	0.00126	0.4879181	0.0536866	0.0005839	-0.0042603	0.5362174	-0.0505161
0.9994161	0.0013419	0.4637826	0.0550769	0.0023342	-0.0084289	0.5602683	-0.0487619
0.9976658	0.001587	0.4397317	0.05632	0.0052468	-0.0125011	0.5841786	-0.0469124
0.9947532	0.0019938	0.4158215	0.0574033	0.0093149	-0.0164706	0.6078921	-0.0449802
0.990685	0.0025595	0.3921079	0.0583145	0.0145291	-0.02033	0.6313537	-0.0429778
0.9854709	0.0032804	0.3686463	0.0590419	0.0208771	-0.0240706	0.6545085	-0.0409174
0.9791229	0.0041519	0.3454915	0.0595747	0.0283441	-0.0276827	0.6773025	-0.0388109
0.9716559	0.0051685	0.3226976	0.0599028	0.0369127	-0.0311559	0.6996823	-0.03667
0.9630873	0.0063238	0.3003177	0.0600172	0.0465628	-0.0344792	0.7215958	-0.0345058
0.9534372	0.0076108	0.2784042	0.0599102	0.057272	-0.0376414	0.7429917	-0.0323294
0.942728	0.0090217	0.2570083	0.0595755	0.0690152	-0.040631	0.7638202	-0.0301515
0.9309849	0.0105485	0.2361799	0.0590081	0.0817649	-0.0434371	0.7840324	-0.0279828
0.9182351	0.0121823	0.2159676	0.0582048	0.0954915	-0.0460489	0.8035813	-0.0258337
0.9045085	0.0139143	0.1964187	0.057164	0.1101628	-0.0484567	0.8224211	-0.0237142
0.8898372	0.0157351	0.1775789	0.0558856	0.1257446	-0.0506513	0.8405079	-0.0216347
0.8742554	0.0176353	0.1594921	0.0543715	0.1422005	-0.0526251	0.8577995	-0.0196051
0.8577995	0.0196051	0.1422005	0.0526251	0.1594921	-0.0543715	0.8742554	-0.0176353
0.8405079	0.0216347	0.1257446	0.0506513	0.1775789	-0.0558856	0.8898372	-0.0157351
0.8224211	0.0237142	0.1101628	0.0484567	0.1964187	-0.057164	0.9045085	-0.0139143
0.8035813	0.0258337	0.0954915	0.0460489	0.2159676	-0.0582048	0.9182351	-0.0121823
0.7840324	0.0279828	0.0817649	0.0434371	0.2361799	-0.0590081	0.9309849	-0.0105485
0.7638202	0.0301515	0.0690152	0.040631	0.2570083	-0.0595755	0.942728	-0.0090217
0.7429917	0.0323294	0.057272	0.0376414	0.2784042	-0.0599102	0.9534372	-0.0076108
0.7215958	0.0345058	0.0465628	0.0344792	0.3003177	-0.0600172	0.9630873	-0.0063238
0.6996823	0.03667	0.0369127	0.0311559	0.3226976	-0.0599028	0.9716559	-0.0051685
0.6773025	0.0388109	0.0283441	0.0276827	0.3454915	-0.0595747	0.9791229	-0.0041519
0.6545085	0.0409174	0.0208771	0.0240706	0.3686463	-0.0590419	0.9854709	-0.0032804
0.6313537	0.0429778	0.0145291	0.02033	0.3921079	-0.0583145	0.990685	-0.0025595
0.6078921	0.0449802	0.0093149	0.0164706	0.4158215	-0.0574033	0.9947532	-0.0019938
0.5841786	0.0469124	0.0052468	0.0125011	0.4397317	-0.05632	0.9976658	-0.001587
0.5602683	0.0487619	0.0023342	0.0084289	0.4637826	-0.0550769	0.9994161	-0.0013419
0.5362174	0.0505161	0.0005839	0.0042603	0.4879181	-0.0536866	1	-0.00126
0.5120819	0.052162	0	0	0.5120819	-0.052162		

APPENDIX C

Parallellized Part of Main Code

Paralellized Dymore subroutine is given below. “MPI_initialize” and “MPI_finalize” functions are called in main program to start and finish parallelized section while a file which lift,drag and moment coefficients are written is defined in Iost structure and called from it via access functions.

```
/*====================================================================*/
void RotorComputeInternalAirloads
(Rotor rotor,     /* pointer to Rotor   */
 FemCtrl femctrl, /* pointer to FemCtrl */
 Iost iost,       /* pointer to Iost    */
 AeroInt aeroint  /* pointer to AeroInt */ ) {
/*====================================================================*/
/*  Compute the rotor airloads                                        */
/*====================================================================*/
    FldProp fldprop = AeroIntGetFluidProperties(aeroint); int ilfn, iast;
    UaModl uamodl = AeroIntGetUnsteadyAerodynamicModel(aeroint);
      TspCtrl tspctrl = FemCtrlGetTspCtrl(femctrl);
      double timei = TspCtrlGetStepInitialTime(tspctrl);
    FILE *debugFile;
    /*===============================*/
    /*  Loop over the lifting lines  */
    /*===============================*/
    for (ilfn=0; ilfn<RotorGetNumberOfLiftingLines(rotor); ilfn++) {
        LfnLine lfnline = RotorGetLiftingLine(rotor,ilfn);
        if (LfnLineGetAlsType(lfnline) == ALS_MATCHED) continue;

    // Calculation of airloads using SU2
        AldType aldtype = AeroIntGetAldType(aeroint);
        if (aldtype == ALD_SU2){
            MPI_Barrier(MPI_COMM_WORLD);

            double AoA,Mach,MachIP,Re,air_density,dynamic_visc;
            double gamma,gas_constant,freestream_temp,speed_of_sound;
            double CL_array[30], CD_array[30], CM_array[30], CD0_array[30];
            double AOA_array[30], M_array[30], RE_array[30];
            double coef[6],LinC[3];
            coef[0]=coef[1]=coef[2]=coef[3]=coef[4]=coef[5]=0;
            int iterstep=IostGetIteNum(iost);

    // Get the row_rank and size in the original communicator
            int world_rank, world_size;
            MPI_Comm_rank(MPI_COMM_WORLD, &world_rank);
            MPI_Comm_size(MPI_COMM_WORLD, &world_size);
            if (world_rank == 0) {
                debugFile = IostGetDebugFile(iost);
```

```
            }
    // Split the communicator based on the color and use the original row_rank
for ordering
            extern MPI_Comm MPI_COMM_LOCAL;
            extern int uflag,row_rank;
            int max_nb_color = 8;
            int group_procs = 16;
            MPI_Barrier(MPI_COMM_WORLD);
            int color = world_rank / group_procs;
            MPI_Comm_split(MPI_COMM_WORLD, color, world_rank,
&MPI_COMM_LOCAL);
            MPI_Comm_rank(MPI_COMM_LOCAL, &row_rank);
            double Cl, Cd, Cm, Cd0;
            /*double Cl0, Cm0, Cdp0;*/
            int cflag, rowsize, histfileflag;
            char histfname_dummy[1024];

            /*-----------------------------*/
            /*  Loop over the airstations  */
            /*-----------------------------*/
            for (iast=0; iast<LfnLineGetNumberOfAirstations(lfnline); iast++)
{
                if (color==iast){
                    AirSta ast = LfnLineGetAirStation(lfnline,iast);
                    AirStaSetId(ast,iast+1);
                    AstFlpComputeFlowParametersPeters(ast,fldprop);
                    AstFlp asf = AirStaGetAstFlp(ast);
                    AoA = AstFlpGetAngleOfAttack(asf);
                    Mach = AstFlpGetMachNumber(asf);
                    MachIP = AstFlpGetMachNumberInPlane(asf);
                    air_density = 1.2886;
                    dynamic_visc = 1.853e-5;
                    gamma = 1.4;
                    gas_constant = 287.87;
                    freestream_temp = 288.15;
                    speed_of_sound = sqrt(gamma * gas_constant *
freestream_temp);
                    Re = 1.8e6;

                    ThreeVal np=malloc(sizeof(OThreeVal));
                    np->value_1=np->value_2=np->value_3=0;
                    uflag=cflag=0;
                    if (row_rank==0){
                        histfileflag = exist_history(iost, AoA, Mach, 0);
                    }
                    MPI_Bcast(&histfileflag, 1, MPI_INT, 0, MPI_COMM_LOCAL);
                    MPI_Barrier(MPI_COMM_LOCAL);
                    if (histfileflag!=1){
                        su2pro(np, AoA, Mach, Re);
                        MPI_Barrier(MPI_COMM_LOCAL);
                    }else{
                        if (row_rank==0){
                            printf("steady history exists\n");}
                    }
                    if (row_rank==0){
                        History history=malloc(sizeof(OHistory));
                        if (histfileflag!=1){
```

```
                            Cl=np->value_1;
                            Cd=np->value_2;
                            Cm=np->value_3;

                            strcpy(histfname_dummy,np->hist_fname);
                            strcat(histfname_dummy,".dat");
                            history->histname=histfname_dummy;
                            history_read(history);
                            cflag=check_convergence(history);
                        }
                        else{
                            history->histname=iost->histfname;
                            history_read(history);
                            rowsize=history->datalength;
                            Cl=history->Cl[rowsize-1];
                            Cd=history->Cd[rowsize-1];
                            Cm=history->Cm[rowsize-1];
                            cflag=check_convergence(history);
                        }
                        history_free(history);
                        Cd0=0.008;
                        /*xfoil(&Cl0, &Cd0, &Cm0, &Cdp0, ZERO, MachIP, Re);*/
                    }
                    MPI_Bcast(&cflag, 1, MPI_INT, 0, MPI_COMM_LOCAL);
                    MPI_Barrier(MPI_COMM_LOCAL);
/*unsteady calculation*/
                    if (cflag==0){
                        uflag=1;
                        if (row_rank==0){
                            histfileflag = exist_history(iost, AoA, Mach, 1);
                        }
                        MPI_Bcast(&histfileflag, 1, MPI_INT, 0,
MPI_COMM_LOCAL);
                        MPI_Barrier(MPI_COMM_LOCAL);
                        if (histfileflag!=1){
                            su2pro(np, AoA, Mach, Re);
                            MPI_Barrier(MPI_COMM_LOCAL);
                        }else{
                            printf("transient history exists\n");
                        }
                        if (row_rank==0){
                            History history=malloc(sizeof(OHistory));
                            if (histfileflag!=1){
                                strcpy(histfname_dummy,np->hist_fname);
                                strcat(histfname_dummy,".dat");
                                history->histname=histfname_dummy;
                                history_read(history);

                                rowsize=history->datalength;
                                Cl = history_mean(history->Cl, rowsize);
                                Cd = history_mean(history->Cd, rowsize);
                                Cm = history_mean(history->Cm, rowsize);
                            }
                            else{
                                history->histname=iost->histfname;
                                history_read(history);
                                rowsize=history->datalength;
```

```
                                Cl = history_mean(history->Cl, rowsize);
                                Cd = history_mean(history->Cd, rowsize);
                                Cm = history_mean(history->Cm, rowsize);
                            }
                            history_free(history);
                        }
                    }

                    if(np){
                        free(np);
                        np=NULL;
                    }
                }
            }
        MPI_Barrier(MPI_COMM_WORLD);

// Gather coefficients in root process
        if (world_rank == 0) {
            int i, ij;
            ij=0;
            for (i = 0; i < world_size; i+=group_procs) {
                if (i != world_rank) {
                    MPI_Recv(&AOA_array[ij], 1, MPI_DOUBLE, i, i,
MPI_COMM_WORLD,MPI_STATUS_IGNORE);
                    MPI_Recv(&M_array[ij], 1, MPI_DOUBLE, i, 10*i,
MPI_COMM_WORLD,MPI_STATUS_IGNORE);
                    MPI_Recv(&RE_array[ij], 1, MPI_DOUBLE, i, 100*i,
MPI_COMM_WORLD,MPI_STATUS_IGNORE);
                    MPI_Recv(&CL_array[ij], 1, MPI_DOUBLE, i, 1000*i,
MPI_COMM_WORLD,MPI_STATUS_IGNORE);
                    MPI_Recv(&CD_array[ij], 1, MPI_DOUBLE, i, 10000*i,
MPI_COMM_WORLD,MPI_STATUS_IGNORE);
                    MPI_Recv(&CM_array[ij], 1, MPI_DOUBLE, i, 100000*i,
MPI_COMM_WORLD,MPI_STATUS_IGNORE);
                    MPI_Recv(&CD0_array[ij], 1, MPI_DOUBLE, i, 1000000*i,
MPI_COMM_WORLD,MPI_STATUS_IGNORE);
                    ij++;}
                else{
                    AOA_array[ij]=AoA;
                    M_array[ij]=Mach;
                    RE_array[ij]=Re;
                    CL_array[ij]=Cl;
                    CD_array[ij]=Cd;
                    CM_array[ij]=Cm;
                    CD0_array[ij]=Cd0;
                    ij++;}
            }
        }
        else {
            MPI_Send(&AoA, 1, MPI_DOUBLE, 0, world_rank,MPI_COMM_WORLD);
            MPI_Send(&Mach, 1, MPI_DOUBLE, 0, 10*world_rank, MPI_COMM_WORLD);
            MPI_Send(&Re, 1, MPI_DOUBLE, 0, 100*world_rank, MPI_COMM_WORLD);
            MPI_Send(&Cl, 1, MPI_DOUBLE, 0, 1000*world_rank, MPI_COMM_WORLD);
            MPI_Send(&Cd, 1, MPI_DOUBLE, 0, 10000*world_rank, MPI_COMM_WORLD);
            MPI_Send(&Cm, 1, MPI_DOUBLE, 0, 100000*world_rank,
MPI_COMM_WORLD);
```

```
            MPI_Send(&Cd0, 1, MPI_DOUBLE, 0, 1000000*world_rank,
MPI_COMM_WORLD);
        }
        MPI_Comm_free(&MPI_COMM_LOCAL);
        for (iast=0; iast<LfnLineGetNumberOfAirstations(lfnline); iast++) {
            MPI_Bcast(&CL_array[iast], 1, MPI_DOUBLE, 0, MPI_COMM_WORLD);
            MPI_Bcast(&CD_array[iast], 1, MPI_DOUBLE, 0, MPI_COMM_WORLD);
            MPI_Bcast(&CD0_array[iast], 1, MPI_DOUBLE, 0, MPI_COMM_WORLD);
            MPI_Bcast(&CM_array[iast], 1, MPI_DOUBLE, 0, MPI_COMM_WORLD);
        }
        MPI_Barrier(MPI_COMM_WORLD);

// Calculate airloads in root process
        for (iast=0; iast<LfnLineGetNumberOfAirstations(lfnline); iast++) {
            AirSta ast = LfnLineGetAirStation(lfnline,iast);
            AirStaSetId(ast,iast+1);
            AstFlp asf = AirStaGetAstFlp(ast);
            if (world_rank == 0) {
                fprintf(debugFile,"\n %f \t %i \t %i \t %f \t %f \t %f \t %f
\t %f \t %f \t %f", timei, iterstep, iast+1, AOA_array[iast], M_array[iast],
RE_array[iast], CL_array[iast], CD_array[iast], CM_array[iast],
CD0_array[iast]);
            }
            coef[0]=5.73; coef[1]=CL_array[iast]; coef[2]=CD_array[iast];
            coef[3]=CD0_array[iast]; coef[4]=-CM_array[iast]; coef[5]=0;
            LinC[0] = LinC[1] = LinC[2] = 0.1;

            /*---------------------*/
            /*  Save coefficients  */
            /*---------------------*/
            AstFlpSetA0 (asf,coef[0]); AstFlpSetCl (asf,coef[1]);
            AstFlpSetCd (asf,coef[2]); AstFlpSetCd0(asf,coef[3]);
            AstFlpSetCm (asf,coef[4]); AstFlpSetCh (asf,coef[5]);
            A3D_u0_v(AstFlpGetLinCs(asf),LinC);

            UaModlComputeAirloads(uamodl,femctrl,iost,aeroint,fldprop,ast);
        }
    }

// Calculation of airloads using XFOIL or tables
    else{
        /*-----------------------------*/
        /*  Loop over the airstations  */
        /*-----------------------------*/
        for (iast=0; iast<LfnLineGetNumberOfAirstations(lfnline); iast++) {
            AirSta ast = LfnLineGetAirStation(lfnline,iast);
            AirStaSetId(ast,iast+1);
            UaModlComputeAirloads(uamodl,femctrl,iost,aeroint,fldprop,ast);
        }
    }
}
}
```

Functions added to Dymore subroutine to process SU2 history data are given below. They are mainly formed of subroutines one of which reads lift,drag and moment coefficients from history file, other checks whether history file exist in current computation folder or not, another checks convergence of the history data, calculates of peak points in order to calculate mean values of lift, drag and moment coefficients and frees history data from the memory.

```
/*====================================================================*/
void history_read(History history) {
    char* string[2000];
    char line[2000];
    char *p, *array[22];
    int i, j, k;
    FILE *file;
    file = fopen(history->histname, "r");
    i=0; k=0;
    while(fgets(line, sizeof line, file)!=NULL){
        if (k>2){
            string[i]=line;
            p = strtok(string[i], ",");
            j=0;
            while (p != NULL){
                array[j++] = p;
                p = strtok(NULL, ",");
            }
            history->Cl[i]=strtod(array[1],NULL);
            history->Cd[i]=strtod(array[2],NULL);
            history->Cm[i]=strtod(array[6],NULL);
            i++;
        }
        k++;
    }
    fclose(file);
    history->datalength=i;
    return;
}
/*====================================================================*/
int exist_history(Iost iost, double Val_AOA, double Val_MACH, int tflag){
    char strhist[50]="history_M";
    char strmach[10], straoa[10];
    sprintf (strmach,"%4.2f",Val_MACH);
    strcat(strhist,strmach);
    sprintf (straoa,"%4.1f",Val_AOA);
    strcat(strhist,"_A");
    strcat(strhist,straoa);
    if (tflag==0){
        strcat(strhist,".dat");
    } else{
        strcat(strhist,"_u.dat");
    }
       if (access(strhist, F_OK ) != -1) {
        strcpy(iost->histfname,strhist);
        return 1;
    }
       else{
        return 0;
```

```
    }
}
/*====================================================================*/
int check_convergence(History history){
    int i,n,start_index;
    n=history->datalength;
    double lastdata=history->Cd[n-1];
    double convflag=1;

    if (n>200){start_index=n-50;}
    else{start_index=0;}
    if (lastdata>1){
      return 0;
    }
    else{
    for (i=start_index; i<n-1; i++ ){
        if (absolute(history->Cd[i]-lastdata)>0.01){
            convflag=0;
            break;
        }
    }
    return convflag;
    }
}
/*====================================================================*/
int calculate_peaks(double *data,int n){
    int i, j, start_index;
    double ddata1,ddata2;
    j=0;
    if (n>100){start_index=n-100;}
    else {start_index=0;}
    if (n<10){return 0;}
    else{
        for (i=start_index; i<n-2; i++ ) {
            ddata1=data[i+1]-data[i];
            ddata2=data[i+2]-data[i+1];
            if (ddata1*ddata2<=0){j++;}
        }
        if (j<2){return 0;}
        else{return j-1;}
    }
}
/*====================================================================*/
double history_mean(double *data, int n){
    double ddata1, ddata2;
    int stored_index[1500];
    double sum, mean;
    int i, k, tk, igg, start_index;

    if (n<50){
        sum=0.;
        for (i=0; i<n; i++){
            sum=sum+data[i];
        }
        mean=sum/n;
        return mean;
    }
```

```
    else {
        if (n>100){start_index=n-50;}
        else {start_index=50;}
        k=0;
        for (i=start_index; i<n-2; i++) {
            ddata1=data[i+1]-data[i];
            ddata2=data[i+2]-data[i+1];
            if (ddata1!=0&&ddata2!=0){
              if (ddata1*ddata2<=0){
                  stored_index[k]=i+1;
                  k++;
              }
            }
        }
        if (k%2==0){
          tk=k;
        }
        else{
          tk=k-1;
        }

        if (tk>6){
          sum=0.;
          igg=0;
          for (i=stored_index[tk-1]; i>(stored_index[tk-7]-1); i--){
              sum=sum+data[i];
              igg++;
          }
          mean=sum/igg;
          return mean;
        }
        else{
          sum=0.;
          igg=0;
          for (i=n; i>n-50; i--){
            sum=sum+data[i];
            igg++;
          }
          mean=sum/igg;
          return mean;
         }
    }
}
/*====================================================================*/
void history_free(History history){
    if(history){
        free(history);
        history=NULL;
    }
}
```

Common structures added for data sharing between codes are given here. Below header file is used to return multiple variables mainly lift, drag, moment coefficients as well as history file name from C++ code to C code.

```
#ifndef RETURNVALUES_H
#define RETURNVALUES_H

#ifdef __cplusplus
extern "C"
{
#endif
    typedef struct returnvalues{
    double value_1, value_2, value_3;
    char hist_fname[1024];
}*ThreeVal,OThreeVal;
#ifdef __cplusplus
}
#endif
#endif
```

Below header file is used to define global variables which are global through all program. “MPI_Comm_World” variable is a global communication world definement in default in MPI routines. SU2 initially uses “MPI_Comm_World”. All “MPI_Comm_World” are changed to something dummy “MPI_Comm_Local” in SU2. The reason is that main purpose is to use “MPI_Comm_World” in main program and split this main communication World into smaller communication worlds called as “MPI_Comm_Local”. By doing this, double level parallelization is obtained. Those are used to make sure that MPI communication variable “MPI_Comm_Local” gets the same value throughout SU2 subroutines. This header file is called at the main header file of SU2. “uflag” is used to flag whether analysis type is unsteady or not.

```
#ifndef GLOBAL_H
#define GLOBAL_H

#ifdef __cplusplus
    extern "C" MPI_Comm MPI_COMM_LOCAL;
    extern "C" int uflag;
    extern "C" int row_rank;
#else
    extern MPI_Comm MPI_COMM_LOCAL;
    extern int uflag;
    extern int row_rank;
#endif
#endif
```

Below header file is used to share history file data of SU2 data between history subroutines and define subroutines.

```
#ifndef INTERFACE_H
#define INTERFACE_H

#include <stdio.h>
#include <stdlib.h>
#include <string.h>
#include <errno.h>
#include <math.h>
#include <fcntl.h>
#include <assert.h>
#include <unistd.h>

typedef struct history{
    double Cl[2000];
    double Cd[2000];
    double Cm[2000];
    int datalength;
    char* histname;
}*History,OHistory;

void history_read(History);
void history_free(History);
int check_convergence(History);
int exist_history(Iost, double, double,int);
double history_mean(double *,int);
double absolute(double);
int su2pro(ThreeVal,double,double,double);
extern double xfoil(double*, double*, double*, double*, double, double,
double);

#endif
```

Main XFOIL subroutine is given. C-FORTRAN binding are used with intrinsic functions.

```
      SUBROUTINE XFOIL(CLx,CDx,CMx,CDPx,ADEGin,MAINF1in,REINF1in)
     & BIND(C,name="xfoil")
      use omp_lib
      use, intrinsic :: ISO_C_BINDING
      real(C_DOUBLE), intent(OUT) :: CLx
      real(C_DOUBLE), intent(OUT) :: CDx
      real(C_DOUBLE), intent(OUT) :: CMx
      real(C_DOUBLE), intent(OUT) :: CDPx
      real(C_DOUBLE), intent(IN),VALUE :: ADEGin
      real(C_DOUBLE), intent(IN),VALUE :: MAINF1in
      real(C_DOUBLE), intent(IN),VALUE :: REINF1in
      CHARACTER*32 FOSTER
        INCLUDE 'XFOIL.INC'

        DIMENSION IINPUT(20), RINPUT(20)
        DATA ANGTOL / 40.0 /  !- max panel angle threshold for warning
        data verse/.false./
        CALL INIT

        LU = 8
        ADEG      = ADEGin
```

```
        MINF1     = MAINF1in
        REINF1    = REINF1in
        IINPUT(1) = 0012

        CALL NACA(IINPUT(1))
        CALL OPER

        CLx=CL
        CDx=CD
        CMx=CM
        CDPx=CDP
        WRITE(*,*) IINPUT(1), ADEGin, MAINF1in, CLx, CDx, CMx
        RETURN
      END ! XFOIL
```

Main SU2 subroutine is given. MPI initialization and finalization are deactivated in order to start MPI in main program Dymore. Angle of attack, Mach numbers and Reynolds numbers are passed to internal solver drivers by directly passing variables since changing private class values using access functions is more complicated. Returned values are written to “returnvalues” structure at head processor for each splitted group of processors. According to analysis type, steady or unsteady configuration file is read by considering parameter of “uflag”. History file name is changed with case angle of attack and Mach number so that in main program compution necessity is checked whether history file exist or not.

```
#include "../include/SU2_CFD.hpp"
#include "../../returnvalues.h"

using namespace std;
extern "C" int su2pro(ThreeVal, double, double, double);
extern "C" {MPI_Comm MPI_COMM_LOCAL;
    int uflag;
    int row_rank;
}

/*int main(int argc, char *argv) {*/
int su2pro(ThreeVal threevalptr, su2double value_AOA, su2double value_MACH,
su2double value_REYNOLDS) {

  unsigned short nZone, nDim;
  char config_file_name[MAX_STRING_SIZE];
  bool fsi;

  /*--- MPI initialization, and buffer setting ---*/
/*#ifdef HAVE_MPI
  int  buffsize;
  char *buffptr;
  SU2_MPI::Init(&argc, &argv);
  MPI_Buffer_attach( malloc(BUFSIZE), BUFSIZE );
```

```
#endif*/

  /*--- Create a pointer to the main SU2 Driver ---*/
  CDriver *driver = NULL;

  /*--- Load in the number of zones and spatial dimensions in the mesh file
(If no config
   file is specified, default.cfg is used) ---*/

/*  if (argc == 2) { strcpy(config_file_name, argv[1]); }
  else { strcpy(config_file_name, "default.cfg"); }*/
    if (uflag==0){
        strcpy(config_file_name, "inv_NACA0012.cfg");
    }
    else{
        strcpy(config_file_name, "inv_NACA0012_ust.cfg");
    }

  /*--- Read the name and format of the input mesh file to get from the mesh
   file the number of zones and dimensions from the numerical grid (required
   for variables allocation)  ---*/

  CConfig *config = NULL;
  config = new CConfig(config_file_name, SU2_CFD);

  nZone = GetnZone(config->GetMesh_FileName(), config->GetMesh_FileFormat(),
config);
  nDim  = GetnDim(config->GetMesh_FileName(), config->GetMesh_FileFormat());
  fsi = config->GetFSI_Simulation();

  /*--- First, given the basic information about the number of zones and the
   solver types from the config, instantiate the appropriate driver for the
problem
   and perform all the preprocessing. ---*/

  if (nZone == SINGLE_ZONE) {

    /*--- Single zone problem: instantiate the single zone driver class. ---*/

    driver = new CSingleZoneDriver(config_file_name, nZone, nDim, value_AOA,
value_MACH, value_REYNOLDS);
      config->SetConv_FileName(value_AOA, value_MACH);

  } else if (config->GetUnsteady_Simulation() == TIME_SPECTRAL) {

    /*--- Use the spectral method driver. ---*/

    driver = new CSpectralDriver(config_file_name, nZone, nDim, value_AOA,
value_MACH, value_REYNOLDS);

  } else if ((nZone == 2) && fsi) {

    /*--- FSI problem: instantiate the FSI driver class. ---*/

    driver = new CFSIDriver(config_file_name, nZone, nDim, value_AOA,
value_MACH, value_REYNOLDS);
```

```
  } else {

    /*--- Multi-zone problem: instantiate the multi-zone driver class by 
default
     or a specialized driver class for a particular multi-physics problem. ---
*/

    driver = new CMultiZoneDriver(config_file_name, nZone, nDim, value_AOA, 
value_MACH, value_REYNOLDS);

    /*--- Future multi-zone drivers instatiated here. ---*/

  }

  /*--- Launch the main external loop of the solver ---*/
  driver->StartSolver();
    if (row_rank==0){
        double value_CL=driver->Get_Lift();
        double value_CD=driver->Get_Drag();
        double value_CM=driver->Get_Mz();

        threevalptr->value_1=value_CL;
        threevalptr->value_2=value_CD;
        threevalptr->value_3=value_CM;

        string strdummy=config->GetConv_FileName();
        char chardummy[1024];
        strncpy(chardummy, strdummy.c_str(), sizeof(chardummy));
        chardummy[sizeof(chardummy) - 1] = 0;
        strcpy(threevalptr->hist_fname,chardummy);
    }

  /*--- Postprocess all the containers, close history file, exit SU2 ---*/
  driver->Postprocessing();

  if (driver != NULL) delete driver;
  driver = NULL;

 /*--- Finalize MPI parallelization ---*/
/* #ifdef HAVE_MPI
  MPI_Buffer_detach(&buffptr, &buffsize);
  free(buffptr);
  MPI_Finalize();
#endif*/
    return 0;
}
```

APPENDIX D

Grid Generation Macro

By using record macro option in Pointwise, a structured c grid is generated. Then macro script is regenerated in a FORTRAN program and run from it automatically. Parameters like growth rate or first Wall height is modified with an input file given in section 0.

```
! POINTWISE C-GRID SCRIPT
        program main
        real firstlayer,tespacing,lespacing
        integer ipoint,itepoint
        character*10 rAF
        character*150 path_Pwise, path_work

        pi = atan(1.)*4

!.. read case file
        open(1,file='cases.txt')
        read(1,*)
        read(1,*) path_work
        read(1,*)
        read(1,*) path_Pwise
        read(1,*)
        read(1,*) rAF(i)
        read(1,*)
        read(1,*) ipoint
        read(1,*)
        read(1,*) itepoint
        read(1,*)
        read(1,*) firstlayer
        read(1,*)
        read(1,*) growthrate
        read(1,*)
        read(1,*) lespacing
        read(1,*)
        read(1,*) tespacing
        read(1,*)
        read(1,*) stopheight
        close(1)

!.. create structured c grid
        open(1,file='pw_mesh_cgrid.glf')
        write(1,*)'# Pointwise V17.0 Journal file - Tue Oct 14 16:20:35 2014'
        write(1,*)
        write(1,*)'package require PWI_Glyph 2.17.0'
        write(1,*)
        write(1,*)'pw::Application setUndoMaximumLevels 5     '
```

```
        write(1,*)
        write(1,*)'set _TMP(mode_10) [pw::Application begin DatabaseImport]
'
        write(1,*)'  $_TMP(mode_10) initialize -type Automatic
{',trim(path_work),rAF(i),'.dat}'
        write(1,*)'  $_TMP(mode_10) read
'
        write(1,*)'  $_TMP(mode_10) convert                                  '
        write(1,*)'$_TMP(mode_10) end                                        '
        write(1,*)'unset _TMP(mode_10)                                       '
        write(1,*)'pw::Application markUndoLevel {Import Database}        '
        write(1,*)
        write(1,*)'set _DB(1) [pw::DatabaseEntity getByName "curve-1"]   '
        write(1,*)'set _TMP(split_params) [list] '
        write(1,*)'lappend _TMP(split_params) [$_DB(1) getParameter -closest
[pw::Application getXYZ [$_DB(1) getPosition&
     &        -arc [expr 50 / 100.0]]]]'
        write(1,*)'set _TMP(PW_40) [$_DB(1) split $_TMP(split_params)]  '
        write(1,*)'unset _TMP(split_params) '
        write(1,*)'unset _TMP(PW_40)'
        write(1,*)'pw::Application markUndoLevel {Split}                   '
        write(1,*)
        write(1,*)'set _DB(2) [pw::DatabaseEntity getByName "curve-1-split-2"]
'
        write(1,*)'set _DB(3) [pw::DatabaseEntity getByName "curve-2"]
'
        write(1,*)'set _DB(4) [pw::DatabaseEntity getByName "curve-1-split-1"]
'
        write(1,*)'set _TMP(PW_41) [pw::Connector createOnDatabase -merge 0 -
reject _TMP(unused) [list $_DB(2) $_DB(3) $_DB(4)]] '
        write(1,*)'unset _TMP(unused)   '
        write(1,*)'unset _TMP(PW_41)    '
        write(1,*)'pw::Application markUndoLevel {Connectors On DB Entities} '
        write(1,*)
        write(1,*)'set _CN(1) [pw::GridEntity getByName "con-2"] '
        write(1,*)'set _CN(2) [pw::GridEntity getByName "con-3"] '
        write(1,*)'set _TMP(PW_42) [pw::Collection create] '
        write(1,*)'$_TMP(PW_42) set [list $_CN(1) $_CN(2)] '
        write(1,*)'$_TMP(PW_42) do setDimension ',ipoint
        write(1,*)'$_TMP(PW_42) delete  '
        write(1,*)'unset _TMP(PW_42)'
        write(1,*)'pw::Application markUndoLevel {Dimension}'
        write(1,*)
        write(1,*)'set _CN(3) [pw::GridEntity getByName "con-1"]'
        write(1,*)'set _TMP(PW_43) [pw::Collection create]'
        write(1,*)'$_TMP(PW_43) set [list $_CN(3)] '
        write(1,*)'$_TMP(PW_43) do setDimension ',itepoint
        write(1,*)'$_TMP(PW_43) delete'
        write(1,*)'unset _TMP(PW_43)'
        write(1,*)'pw::Application markUndoLevel {Dimension}'
        write(1,*)
        write(1,*)'set _TMP(mode_10) [pw::Application begin Modify [list
$_CN(2) $_CN(1)]]'
        write(1,*)'  set _TMP(PW_44) [$_CN(1) getDistribution 1]'
        write(1,*)'  $_TMP(PW_44) setEndSpacing ',lespacing
        write(1,*)'  unset _TMP(PW_44)'
        write(1,*)'  set _TMP(PW_45) [$_CN(2) getDistribution 1]'
```

```
        write(1,*)'  $_TMP(PW_45) setBeginSpacing ',lespacing
        write(1,*)'  unset _TMP(PW_45)'
        write(1,*)'$_TMP(mode_10) end '
        write(1,*)'unset _TMP(mode_10)'
        write(1,*)'pw::Application markUndoLevel {Change Spacing(s)}'
        write(1,*)
        write(1,*)'set _TMP(mode_10) [pw::Application begin Modify [list
$_CN(2) $_CN(1)]]'
        write(1,*)'  set _TMP(PW_46) [$_CN(1) getDistribution 1]'
        write(1,*)'  $_TMP(PW_46) setBeginSpacing ',tespacing
        write(1,*)'  unset _TMP(PW_46)'
        write(1,*)'  set _TMP(PW_47) [$_CN(2) getDistribution 1]'
        write(1,*)'  $_TMP(PW_47) setEndSpacing ',tespacing
        write(1,*)'  unset _TMP(PW_47)'
        write(1,*)'$_TMP(mode_10) end '
        write(1,*)'unset _TMP(mode_10)'
        write(1,*)'pw::Application markUndoLevel {Change Spacing(s)}'
        write(1,*)
        write(1,*)'set _TMP(mode_10) [pw::Application begin Create]'
        write(1,*)'  set _TMP(PW_48) [pw::Edge createFromConnectors [list
$_CN(1) $_CN(2)]] '
        write(1,*)'  set _TMP(edge_2) [lindex $_TMP(PW_48) 0]'
        write(1,*)'  unset _TMP(PW_48)'
        write(1,*)'  set _TMP(dom_2) [pw::DomainStructured create]'
        write(1,*)'  $_TMP(dom_2) addEdge $_TMP(edge_2) '
        write(1,*)'$_TMP(mode_10) end '
        write(1,*)'unset _TMP(mode_10)'
        write(1,*)'set _TMP(mode_10) [pw::Application begin ExtrusionSolver
[list $_TMP(dom_2)]]'
        write(1,*)'  $_TMP(mode_10) setKeepFailingStep true '
        write(1,*)'  set _DM(1) [pw::GridEntity getByName "dom-1"] '
        write(1,*)'  $_DM(1) setExtrusionSolverAttribute NormalInitialStepSize
',firstlayer
        write(1,*)'  $_DM(1) setExtrusionSolverAttribute SpacingGrowthFactor
',growthrate
        write(1,*)'  $_DM(1) setExtrusionSolverAttribute
NormalKinseyBarthSmoothing 0.0 '
        write(1,*)'  $_DM(1) setExtrusionSolverAttribute NormalMarchingVector
{-0 -0 -1} '
        write(1,*)'  $_DM(1) setExtrusionSolverAttribute StopAtHeight
',stopheight
        write(1,*)'  $_DM(1) setExtrusionBoundaryCondition Begin SymmetryX  '
        write(1,*)'  $_DM(1) setExtrusionBoundaryConditionStepSuppression
Begin 0'
        write(1,*)'  $_DM(1) setExtrusionBoundaryCondition End SymmetryX '
        write(1,*)'  $_DM(1) setExtrusionBoundaryConditionStepSuppression End
0'
        write(1,*)'  $_TMP(mode_10) run 2000'
        write(1,*)'$_TMP(mode_10) end '
        write(1,*)'unset _TMP(mode_10)'
        write(1,*)'unset _TMP(dom_2)'
        write(1,*)'unset _TMP(edge_2)'
        write(1,*)'pw::Application markUndoLevel {Extrude, Normal}'
        write(1,*)
        write(1,*)'pw::Application exit'
        system('"D:\Program
Files\Pointwise\PointwiseV17.0R2\win32\bin\Pointwise.exe" pw_mesh_cgrid.glf')
```

```
      close(1)

      stop
      end
```

APPENDIX E

Grid Generation Input file

```
#Working Folder
C:\WORKDIR\
#Folder Path for Pointwise
C:\POINTWISE_DIR\
#Name of the Airfoil
NACA0012_M
#Number of Points on Upper Edge and Lower Edge
200
#Number of Points on Blunt Trailing Edge
38
#First Wall Height
0.000001
#Growth Ratio
1.1
#Leading Edge Spacing
0.001
#Trailing Edge Spacing
0.001
#Stop Height
15
```